

# THERMAL PROCESSING OF POWDER ALUMINUM ALLOYS FOR ADDITIVE MANUFACTURING APPLICATIONS

by

Caitlin Elizabeth Walde

A Dissertation

Submitted to the Faculty

of the

WORCESTER POLYTECHNIC INSTITUTE

in partial fulfillment of the requirements for the

Degree of Doctor of Philosophy

in

Materials Science and Engineering

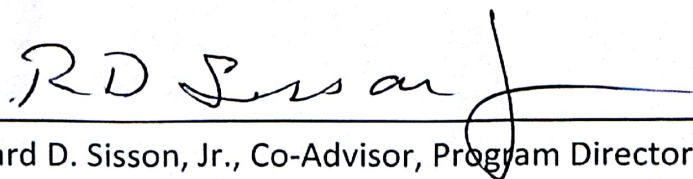
December 2018

APPROVED:



---

Dr. Danielle L. Cote, Major Advisor



---

Dr. Richard D. Sisson, Jr., Co-Advisor, Program Director

## 1 Abstract

For additive manufacturing, research has shown that the chemistry and microstructural properties of the feedstock powder can significantly affect the properties of the consolidated material. Thermal treatment and recycling parameters for powders used in both solid and liquid state processes can further affect the microstructure and properties of the consolidated parts. Understanding the powder microstructure and effects of powder pre-treatment can aid in optimizing the properties of the final consolidated part. This research proposes a method for the characterization and optimization of powder pre-processing thermal parameters using aluminum alloy powder as examples. Light microscopy, electron microscopy, and hardness were used to evaluate each condition.

## 2 Acknowledgements

First and foremost, I would like to express my sincere gratitude to my advisors, Richard Sisson and Danielle Cote, for their guidance, support, and encouragement throughout the completion of my thesis. Not only have I grown as a researcher and scientist, but they have given me opportunities to grow as a teacher and a leader as well.

I also wish to thank my committee members, Prof. Liang, Prof. Makhoulouf, Prof. Shivkumar, and Dr. Anderson, for their feedback and insight throughout the completion of my thesis.

I would like to thank my friends and colleagues in the ARL Cold Spray research group at WPI, specifically Victor Champagne, Baillie (McNally) Haddad, Kyle Fitzpatrick-Schmidt, Derek Tsaknopoulos, Matt Gleason, Bryer Sousa, and Chris Massar, for their help in the lab, their stimulating conversation, and their constant companionship.

I have had much help throughout the completion of my thesis by students and faculty that have worked with me outside of my research group, and I would like to extend a thanks to Dr. Soderhjelm, Alino Te, and Farrah Farhadi for their help. I would also like to thank Rita Shilansky and GlorieAnn Minnich for their logistical help and unwavering support.

I would also like to thank my many friends that have helped keep me sane through this. Among others, thank you; Jess, Julie, Theresa, Haley, and Kyle!

It should also be mentioned that I would not be here if it were not for the unconditional support of my parents; their hard work in making me who I am gave me the opportunity to work with something I love.

Lastly, but most importantly, I would like to thank my fiancé, Keith, for his love, patience, and encouragement in this endeavor. Without his support, help, and confidence in me, this would not have been possible.

### 3 Table of Contents

1	Abstract.....	1
2	Acknowledgements.....	1
3	Table of Contents.....	2
3.1	Table of Figures.....	4
3.2	Table of Tables.....	7
4	Introduction.....	8
4.1	Project Needs.....	8
4.2	Project Goal.....	8
4.3	Background.....	8
5	Literature Review.....	10
5.1	Thermal Treatment of Aluminum Alloys.....	10
5.2	Powder Properties and Treatments.....	11
5.3	Cast versus Powder.....	12
5.4	Phase Identification.....	13
5.4.1	Techniques.....	13
5.4.2	Phase Identification of Al 2024, 6061, and 7075 Powders.....	14
5.5	3D Characterization.....	15
6	Experimental Work.....	17
6.1	Cast versus Powder.....	17
6.1.1	Materials and Methods.....	17
6.1.2	Results and Discussion.....	22
6.1.3	Summary and Conclusion.....	33
6.2	Solution Treatment.....	34
6.2.1	Materials.....	34
6.2.2	Method.....	34
6.2.3	Results and Discussion.....	39
6.2.4	Conclusions.....	59
6.3	Phase Identification.....	61
6.3.1	Materials.....	61
6.3.2	Method.....	61
6.3.3	Results and Discussion.....	63
6.3.4	Conclusions.....	83

6.4	3D Characterization .....	86
6.4.1	Materials .....	86
6.4.2	Method.....	87
6.4.3	Results.....	87
6.4.4	3D vs. 2D .....	90
7	Future Work.....	91
7.1	Cast versus Powder.....	91
7.2	Thermal Treatment.....	91
7.2.1	Solution Treatment.....	91
7.2.2	Aging Treatment .....	91
7.3	3D Characterization .....	91
7.4	Phase Identification .....	91
8	Potential Impact.....	92
8.1	Powder Metallurgy .....	92
8.2	Additive Manufacturing .....	92
8.3	Thermodynamic and Kinetic Modeling.....	92
9	Relevant Presentations & Publications.....	93
9.1	Publications.....	93
9.2	Technical Conference Presentations .....	93
9.3	Technical Conference Posters.....	94
10	References .....	95

### 3.1 Table of Figures

Figure 1: Cooling rate as a function of particle size for each of the gas atomized alloys.....	22
Figure 2 a) Temperature as a function of time for each alloy during casting, and b) calculated cooling rate as a function of time for each alloy during casting.....	23
Figure 3: Feature size as a function of particle size, both predicted and theoretical, for a) 2024, b) 6061, and c) 7075.....	24
Figure 4: DSC thermograms of cast and powder samples in both the control and thermally treated conditions, for a) 2024, b) 6061, and c) 7075. Example: C7075 = as-cast; HC7075 = thermally treated cast; P7075 = as-atomized 7075; HP7075 = thermally treated powder. ....	25
Figure 5: Optical micrograph of Al 7075 after etching, a) as-atomized powder and b) as-cast. ....	26
Figure 6: SEM micrographs of Al 7075 a) as-atomized powder, b) thermally treated powder, c) as-cast, and d) thermally treated cast. ....	27
Figure 7: Phase area percentages for the as-cast, as-atomized, and thermally treated cast and powders for a) 2024, b) 6061, and c) 7075.....	28
Figure 8: Microstructural feature size for the as-cast, as-atomized, and thermally treated cast and powders for a) Al 2024, b) Al 6061, and c) Al 7075. ....	29
Figure 9: Vickers Hardness numbers for the as-cast, as-atomized, and thermally treated cast and powders for a) Al 2024, b) Al 6061, and c) Al 7075. ....	30
Figure 10: a) Equilibrium secondary phases in Al 2024 as a function of temperature and b) secondary phases predicted based on non-equilibrium conditions (Scheil solidification), as predicted by Thermo-Calc.....	35
Figure 11: Equilibrium secondary phases in Al 6061 as a function of temperature as predicted by Thermo-Calc.....	36
Figure 12: Equilibrium secondary phases in Al 7075 as a function of temperature as predicted by Thermo-Calc.....	37
Figure 13: Typical images used for secondary phase fraction and precipitate size analysis; (a) SEM of an As-Atomized 6061 particle, (b) processed image from (a), (c) SEM of a heat treated particle, (d) processed image from (c). ....	38
Figure 14: Low magnification SEM micrographs for 2024 powder a) as-atomized, b) 0 min treated, c) 20 min treated, and d) 120 min treated. High magnification SEM micrograph of powder e) as-atomized, f) 0 min treated, g) 20 min treated, and h) 120 min treated. ....	41
Figure 15: Normalized heat flow vs. temperature (DSC) thermograms for each condition.....	42
Figure 16: 2024 as-atomized powder particle a) SEM and b) EBSD. 60 minute thermally treated powder particle c) SEM and d) EBSD.....	44
Figure 17: Nanohardness measurements of 2024 powder as a function of their treatment time .....	45
Figure 18: Relative frequency as a function of particle size, for select treatment times .....	45
Figure 19: Nanohardness and Secondary phase area fraction as a function of treatment time .....	46
Figure 20: Relative frequency of precipitate sizes for (a) Mg <sub>2</sub> Si, 0 min, (b) Mg <sub>2</sub> Si, 20 min, (c) Mg <sub>2</sub> Si, 40 min, (d) Mg <sub>2</sub> Si, 60 min, (e) Mg <sub>2</sub> Si, 120 min, (f) Mg <sub>2</sub> Si, 240 min, (g) Fe-containing phases, 0 min, (h) Fe-containing phases, 20 min, (i) Fe-containing phases, (k) Fe-containing phases, 120 min, (l) Fe-containing phases, 240 min. ....	48
Figure 21: Secondary phase area fraction (SPAF) as a function of solution treatment time. ....	49
Figure 22: EBSD results for various solution treatment times. (a) As-Atomized, (b) 20 min, (c) 60 min, (d) 240 min. ....	50

Figure 23: DSC scans of select treatment times of 6061 .....	51
Figure 24: Hardness as a function of solution treatment time for 6061 .....	52
Figure 25: Overview SEM micrograph and EBSD micrograph of the as-atomized condition for 7075.....	54
Figure 26: Overview SEM micrographs of the thermally treated conditions of 7075; a) 465 °C for 0min, b) 465 °C for 60min, c) 465 °C for 120min, d) 480 °C for 0min, e) 480 °C for 60min, f) 480 °C for 120min....	55
Figure 27: Area percent of secondary phases present in 7075 as a function of treatment time for both treatment temperatures.....	55
Figure 28: DSC scans of select treatment times of 7075 .....	57
Figure 29: Hardness as a function of solution treatment time for 7075 .....	58
Figure 30: Low magnification HAADF micrographs of powder Al 2024 a) in the as-atomized condition and b) after a 60 minute thermal treatment. ....	63
Figure 31: High magnification HAADF's and elemental EDS maps for the as-atomized condition of 2024 at a triple point a) HAADF, b) Al, c) Cu, d) Fe, e) Mg, f) Mn, and g) Si, and at a boundary h) HAADF, i) Al, j) Cu, k) Fe, l) Mg, m) Mn, and n) Si.....	64
Figure 32: High magnification HAADF's and elemental EDS maps for the 60 minute thermally treated condition of 2024 at a multiple boundaries region 1 a) HAADF, b) Al, c) Cu, d) Fe, e) Mg, f) Mn, and g) Si, at region 2 h) HAADF, i) Al, j) Cu, k) Fe, l) Mg, m) Mn, a .....	66
Figure 33: Phase diagrams predicted using Thermo-Calc a) with Al <sub>15</sub> Si <sub>2</sub> Mn <sub>4</sub> suppressed, b) increased magnification of (a), and c) increased magnification of Figure 1a. ....	67
Figure 34: Typical images used for secondary phase fraction analysis: (a) TEM-HAADF of as-manufactured Al 6061 particle lamella, (b) TEM HAADF of thermally treated Al 6061 particle lamella. ..	68
Figure 35: (a) Equilibrium diagram from Thermo-Calc software, (b) Scheil diagram from Thermo-Calc software, (c) amount of each possible phase as predicted by Thermo-Calc software at varying conditions. ....	69
Figure 36: Overview images of as-manufactured Al 6061: (a) SEM, (b) TEM-HAADF, (c) increased magnification HAADF from (b). Outlined regions show where further analysis will be highlighted.....	70
Figure 37: (a) HAADF image of a triple point in as-manufactured Al 6061. Elemental EDS maps for: (b) Al, (c) Cu, (d) Fe, (e) Mg, (f) Si. (g) High-magnification HAADF of highlighted region in (a).....	71
Figure 38: Elemental EDS maps and HAADF images of Mg-rich phases at a boundary in as-manufactured Al 6061: (a) alternating Mg <sub>2</sub> Si and Fe-rich phases (left to right: HAADF image, Al, Cu, Fe, Mg, Si), (b) alternating Mg <sub>2</sub> Si and Fe-rich phases in a different orientation (left to right: HAADF image, Al, Cu, Mg, Si), (c) unique Mg <sub>2</sub> Si morphology at a boundary (left to right: HAADF image, Al, Cu, Fe, Mg, Si).....	72
Figure 39: Additional morphologies of Mg <sub>2</sub> Si in as-manufactured Al 6061: (a) Fe-rich phase on Mg <sub>2</sub> Si, (b) alternating Fe-rich and Mg <sub>2</sub> Si on a boundary, (c) Mg <sub>2</sub> Si on a boundary, (d) atypical Mg <sub>2</sub> Si morphology. ....	73
Figure 40: Higher magnification a) HAADF, and EDS maps of b) Al, c) Cu, d) Fe, e) Mg, and f) Si showing Mg <sub>2</sub> Si and Al <sub>13</sub> –Fe <sub>4</sub> at a triple point in the as-atomized powder. ....	74
Figure 41: Overview images of thermally treated Al 6061: (a) SEM, (b) TEM HAADF, (c) increased magnification HAADF of similar sample, (d) Mg <sub>2</sub> Si of plate-like morphology, (e) Mg <sub>2</sub> Si dissolving. ....	75
Figure 42: a) HAADF, and EDS maps b) Al, c) Cr, d) Cu, e) Fe, f) Mn, g) Mg, and h) Si showing Al <sub>9</sub> Fe <sub>2</sub> Si–2 and residual Mg <sub>2</sub> Si in the thermally treated powder.....	77
Figure 43: a) HAADF, and EDS maps of b) Al, c) Cr, d) Cu, e) Fe, f) Mn, g) Mg, and h) Si showing another morphology of Al <sub>9</sub> Fe <sub>2</sub> Si–2 in the thermally treated powder.....	78

Figure 44: Overview TEM micrographs for 7075 of a) the as-atomized condition, b) 60min at 465 °C and c) 60min at 480 °C. ....	80
Figure 45: TEM micrograph and EDS maps for 7075 for the as-atomized condition; a) HAADF, b) Al, c) Cu, d) Fe, e) Mg, f) Si, and g) Zn .....	81
Figure 46: TEM micrograph and EDS maps for 7075 for the 60min at 465 °C condition; a) HAADF, b) Al, c) Cu, d) Fe, e) Mg, f) Si, and g) Zn. ....	81
Figure 47: TEM micrograph and EDS maps for 7075 for the 60min at 480 °C condition; a) HAADF, b) Al, c) Cu, d) Fe, e) Mg, f) Si, and g) Zn. ....	82
Figure 48: Volume renderings of (a) secondary phases in a sub-volume of the sectioned As-Atomized particle, (b) secondary phases in the full volume of the sectioned As-Atomized particle, (c) matrix, secondary phases, and pores in the full volume of the sectioned treated particle. ....	88
Figure 49: Slices from sectioning of (a) As-Atomized particle, SEM, (b) As-Atomized particle, EBSD, (c) treated particle, SEM, (d) treated particle, EBSD. ....	89

### 3.2 Table of Tables

Table 1: Droplet density ( $\rho$ ), molten metal droplet temperature ( $T_d$ ) and specific heat of the metal droplets ( $C_p$ ) for each of the Al alloys. ....	18
Table 2: Compositions of the powders and cast samples, compared to the ASM standard, for Al 2024. .	19
Table 3: Compositions of the powders and cast samples, compared to the ASM standard, for Al 6061. .	19
Table 4: Compositions of the powders and cast samples, compared to the ASM standard, for Al 7075. .	20
Table 5: Size distribution characteristics for each of the alloy powders. ....	20
Table 6: Etching procedure for each alloy, for both powder and cast. ....	21
Table 7: Enthalpy of peak at 300 °C for each condition.....	43
Table 8: Secondary phase area (%) for 2024, as measured via TEM. ....	63
Table 9: SPVF for rendered volumes.....	88

## 4 Introduction

### 4.1 Project Needs

Every year, the Department of Defense spends millions of dollars replacing corroded helicopter parts. Not only is replacement costly, but it is time consuming as well – the part needs to be ordered, made, and shipped to the field. While waiting, the helicopters are grounded, halting productivity and inhibiting safety measures on the front.

The cold spray process is being used as a way to repair – rather than replace – the parts. It is fast, portable, and repeatable. Parts can be repaired in a matter of hours, in the field, rather than months, saving up to 12 million dollars annually in time saved, as well as replacement parts. Currently, cold spray is only certified to be used on non-structural parts, which make up 45% of the corroded parts.<sup>1</sup> If the process could be qualified for use on structural parts, additional time and money could be saved. What the process lacks, though, is the necessary high strength and fatigue life to meet the qualifications consistently.

There is one particularly unique aspect about the cold spray process that makes it intriguing to Material Scientists that we can take advantage of, and that is that it's done at “cold” temperatures, so there is no melting. In the process, feedstock powders are combined with a heated carrier gas and accelerated through a converging-diverging nozzle towards a substrate, where the particles adhere and build up layers. Because there is no melting, the properties and microstructural features of the feedstock powder are retained or improved upon once processed.

### 4.2 Project Goal

It is possible to take advantage of the retention of powder properties and features in the consolidated part. The goal of this project is to optimize the properties of the feedstock powder such that the properties of the consolidated part are optimized for a given application. This will be accomplished through evaluating homogenization and solution thermal treatments of the powder. The treatments will be evaluated via scanning electron microscopy (SEM), transmission electron microscopy (TEM), energy-dispersive x-ray spectroscopy (EDS/EDX), electron backscatter diffraction (EBSD), light microscopy, differential scanning calorimetry (DSC), and nanoindentation (NI) in three common aerospace aluminum alloys – 2024, 6061, and 7075.

### 4.3 Background

Cold spray is a process in which metallic powder particles are accelerated at supersonic velocities in a carrier gas through a converging-diverging nozzle towards a substrate, where they plastically deform, form bonds, and adhere, building up layers. Smaller layers for a coating, more layers for a full part.<sup>2</sup> The deposition is highly uniform and has little porosity. Some of the main applications for this process are in coatings, dimensional restoration, and additive manufacturing. Aluminum, copper, and titanium are the most commonly used alloy systems, though other metals, such as molybdenum and tantalum, have been used as well.

The feedstock powder used in cold spray is typically manufactured via gas atomization, where molten metal is separated into droplets by high pressure gas streams, usually nitrogen, argon, or helium. During

the cold spray process, the velocity, temperature, size, and shape of the feedstock powder affect the velocity of the particles, which determines the quality of the coating. Particle size may be easily controlled through the powder manufacturing process or subsequent sieving processes, however shape is not as easily controlled. Helium, nitrogen, and compressed air are typically used as carrier gases in the cold spray process. The gas density, temperature, and pressure also affect the particle velocity.

Work has been done on a through-process model of the cold spray process. This model combines the various stages of the cold spray process – feedstock powder and powder pre-processing; spray parameters such as carrier gas settings, nozzle design, and stand-off distance; and post-consolidation treatments – to simulate and predict how changes in these parameters affect the properties of the consolidated part.

Some concerns of the process moving forward are the ability to recycle the feedstock powder, the cost associated with helium carrier gas though it provides superior coatings, and optimization of all parameters to demonstrate repeatable high strength so the process can be used in structural applications.

## 5 Literature Review

### 5.1 Thermal Treatment of Aluminum Alloys

Thermal treatments may be applied to materials to control their microstructure, and the microstructure directly influences the properties of the material.<sup>3</sup> This is particularly useful in metals where precipitation hardening and annealing are often designed for during alloy development; the three alloys considered here are prime examples. 2024 (Al-Cu alloy), 6061 (Al-Mg-Si alloy), and 7075 (Al-Zn alloy) are all considered heat-treatable alloys. Heat treatment is achieved through a series of steps: homogenization, annealing, solution heat treatment, quenching, natural aging, and artificial aging.

The purpose of the homogenization step is to allow the alloying elements to form a homogenous solid solution within the Al matrix.<sup>4</sup> This may remove any microsegregation and allow for evenly dispersed precipitates to form during subsequent steps. Homogenization is performed in the 350-450°C temperature range for Al alloys, and may often take 15-20 hours, depending on the size of the part.

The annealing step is used to relieve residual stresses induced during forming by softening the material; the goal of this is to make it easier to work with for subsequent forming processes. Annealing is performed at temperatures above the recrystallization temperature, in the 350-450°C range, and may take three to four hours depending on the size of the part and the amount of strain present in the material.

The solution heat treatment step has a goal similar to that of homogenization – form a uniform solid solution – though the solution heat treatment step brings the alloy closer to completion of this goal than the homogenization step. Solution heat treatments are carried out at higher temperatures than homogenization treatments, in the 450-550°C range, which is closer to the eutectic melting temperature of the alloy. Local variations in solute concentration may exist in the part during any of the heat treatment steps, but it is most important in the solution heat treatment step. These local variations may cause a change in the eutectic temperature, which may cause some localized, incipient melting. Incipient melting causes a decrease in properties, but can be avoided through careful selection of treatment temperature and control of the heating rate.

The time held at temperature is highly important, but also extremely variable depending on part dimensions. For example, thin sheets may require a matter of minutes while thicker castings may take over 20 hours. If the time at temperature is too short, a full solid solution will not be achieved, but if it is too long, high temperature oxidation becomes a risk.

After the solution heat treatment, the part is quenched to retain the supersaturated solid solution; this retention is useful to achieve optimal precipitation hardening in subsequent aging steps. The quench rate is of high importance; it must be fast enough to avoid precipitation but slow enough to avoid distortion of the part.

The purpose of the aging steps are to nucleate and grow small coherent or semi-coherent precipitates and their precursors (GP zones). First, solute atoms cluster around quenched in vacancies; their lattice mismatch causes strain fields to form, increasing the strength of the material. Once sufficient solute atoms have diffused to the cluster, coherent precipitates can form, increasing the strain in the lattice. As more atoms diffuse to the precipitate, the precipitate continues to grow and increase the lattice strain, until the matrix can no longer accommodate the amount of strain. At this point, the precipitate loses

some coherency and becomes semi-coherent. As more atoms still continue to diffuse, the precipitate continues to grow, increase strain, and lose coherency, until it becomes incoherent in its equilibrium form. The precursor phases provide the most increases in strength, due to the large amounts of strain in the matrix.

The natural aging step is used to strengthen alloys at room temperature, though not all alloys are capable of this. For example, the 2xxx alloys harden substantially at room temperature over a few days and their properties become stable after 1 week. On the other hand, 6xxx and 7xxx alloys may harden at room temperature, but their properties may still change even after a few years at room temperature. Artificial aging may be used in situations like these to accelerate the process of achieving stable precipitates. Artificial aging uses elevated temperatures, in the 100-200°C, to accelerate the processes that would occur naturally at room temperature.

The predominant precipitate in 2xxx alloys is  $\text{Al}_2\text{Cu}$  ( $\theta$ ), with its precursors  $\theta''$  and  $\theta'$ . In 6xxx alloys,  $\text{Mg}_2\text{Si}$  ( $\beta$ ) is the equilibrium phase, with precursors  $\beta'$  and  $\beta''$ . In 7xxx alloys, there are several precipitation sequences that may occur, depending on the exact alloy composition and local concentrations.  $\text{Al}_2\text{CuMg}$  ( $S$ ),  $\text{Mg}_{32}(\text{Al}, \text{Zn})_{49}$  ( $T$ ), and  $\text{MgZn}_2$  ( $\eta$ ) may be the predominant equilibrium phases with precursors  $T'$  and  $\eta'$ . These phases will be further explored in Section 5.4 Phase Identification.

## 5.2 Powder Properties and Treatments

Powder metallurgy has been explored for many years now, but has gained a renewed interest for the use of metallic powders in additive manufacturing processes. Powder bed ink jet printing, selective laser sintering, selective laser melting, electron beam additive manufacturing, thermal spray, cold spray, and additive friction stir are all additive manufacturing techniques that utilize metallic powders as feedstock.<sup>5-9</sup> In most of these techniques, the powder is melted during processing. Cold spray and additive friction stir are unlike the other processes in that the powder remains solid during consolidation; because of this, some of the microstructural features of the powder are retained during processing.<sup>10-15</sup> This means that it is important to understand the microstructural features of the feedstock powder prior to consolidation.

Little research has been published studying the microstructure and processing of metallic powders. Most of the research published on metallic powders regards the effect of processing conditions on the size distribution, shape, and flowability of the particles, as well as the effect of those properties on the consolidated parts.<sup>11,16</sup> While these properties are important to understand, the microstructural and chemical characteristics of the particles are important as well. This section reviews what is present in the literature regarding the microstructure of rapidly solidified powders.

Metallic powders can be produced through a variety of techniques; atomization, milling, and chemical reduction are among the most common ways.<sup>17</sup> Of these, gas atomized powders are the ones most commonly used in solid state additive manufacturing for their highly spherical particles of high purity, rapid solidification, and homogenous structure.<sup>18</sup>

Levi and Mehrabian show that sub-micron sized aluminum particles exhibit a range of microstructures, from single-crystals with homogeneous structure to multiple grains with microsegregation, with smaller

particles showing less segregation.<sup>19</sup> Adkins and Tsakirooulos, as well as Zheng et al, also show a correlation between particle size and degree of solute segregation.<sup>20,21</sup>

Rokni et al have perhaps performed the most in-depth analysis of gas-atomized aluminum powders to date. They analyze not just the size distribution and shape, but also the internal microstructure utilizing SEM, TEM, and EBSD. They report that gas atomized aluminum particles show surface grain features in the 1-4  $\mu\text{m}$  range, with a similar structure internally which is accompanied by some solute segregation.<sup>12,15,22,23</sup> Additionally, they show that grains are typically equiaxed with some residual stresses.<sup>12</sup>

As Rokni et al show numerous times, the structure present in the powders is also present in the consolidated part. With this in mind, Sabard et al apply a heat treatment to the as-atomized powders prior to use in cold spray consolidation.<sup>24</sup> They found that with a heat treatment of 4 hours at 450°C, particle deformation was enhanced, leading to improved particle-substrate bonding and thicker coatings. Additionally, they found that the heat treated powders had a reduction in solute segregation and a higher porosity than the as-atomized condition. They also observed the formation of some needle-like precipitates in the heat treated condition that were not present in the as-atomized condition. The chosen treatment temperature is based on commercially used treatments for wrought components, and no work has been done to identify treatments specifically designed for powders.

Though Rokni et al have performed extensive microstructural analysis of the as-atomized microstructure in relation to its presence in the consolidated structure, they, and others, and have done little to no work in identifying the specific phases present in the as-atomized structure. Adkins and Tsakirooulos identified the major intermetallic present in their Al-Cr-Zr-Mn powders ( $\text{Al}_{13}\text{Cr}_2$ ) but did not evaluate other phases that may be present.<sup>21</sup> Sabard et al note that analysis in an SEM is not sufficient to identify phases present in gas atomized powder due to the low resolution.<sup>10</sup> Phases present in 2xxx, 6xxx, and 7xxx series aluminum alloys will be further explored in Section 5.4 Literature Review - Phase Identification.<sup>24</sup>

### 5.3 Cast versus Powder

Additive manufacturing is being used in the aerospace industry for repair applications; this can save both time and money over the conventional method of part replacement.<sup>25</sup> Solid-state additive manufacturing techniques are of particular interest because the lack of melting in the feedstock powder results in retainment or improvement of feedstock material properties during processing.<sup>2</sup> The feedstock material for these processes is frequently gas-atomized powder.<sup>26</sup> During the gas-atomization process, molten metal is atomized in a gas stream, where it is rapidly cooled and collected. This rapid solidification results in a dendritic microstructure that often inherently contains segregation of alloying elements. The size and shape of the powder particles is influenced not only by the alloy composition, but also by the processing parameters. For aluminum alloys, the particles tend to be primarily spherical in shape and have a wide size distribution. The size distribution can be more tightly controlled with the addition of a sieving step.

In the application of solid state additive manufacturing used for repair of an existing material, in order to get the best interface between the original part material and the repair material, it is important to understand the properties of both materials. There is ample research and data on the properties of the

original part material – such as tests and data needed to qualify it for use – but research on the newly additively manufactured areas are relatively new and are limited to a case-by-case basis.<sup>27–30</sup> Simulation tools can greatly decrease the time required to fully understand these consolidated materials and decrease the number of experiments needed to find the optimum parameters. These models have been developed to utilize commercially available thermodynamic and kinetic software to take the properties of the feedstock material, couple it with the consolidation process parameters, and then output material properties of the consolidated part.<sup>31</sup> If properties such as consolidated material hardness and tensile strength are desired outputs of the model, then similar properties of the powder must be input into the model. These properties come from one or both of two sources: data generated experimentally or data gathered from published literature.

It is already common practice to gather data on wrought materials through both of the aforementioned techniques; handbooks and decades of experiments give great comparison between literature values and those generated experimentally.<sup>32</sup> It is necessary to apply the same to models for additive manufacturing methods that utilize powders as feedstock. However, when literature is consulted, there is a discrepancy between the types of properties reported for powder alloys and those reported for wrought alloys. Properties such as hardness, tensile strength, melting temperature, and microstructure are reported for wrought alloys,<sup>33–35</sup> while properties such as flowability, particle size distribution, melting temperature, and combustion temperature are reported for powders.<sup>36–38</sup>

While these shape characteristics of the powders are useful for predicting certain aspects of the additive manufacturing process, data on the chemistry and those properties that correlate with mechanical properties are still needed. It is possible to use the data that is already available for wrought alloys as input properties for the feedstock powder, but this may not be accurate. Powder particles are much smaller than wrought samples, so it is hypothesized that there is different behavior at such different scales and cooling rates.

## 5.4 Phase Identification

In order to completely understand the microstructure of a material, it is important to know which phases are present in the microstructure. These phases can be identified through various techniques, and thermodynamic and kinetic modeling has made major advancements in recent years to aid in prediction of which phases are present at certain conditions.

### 5.4.1 Techniques

Various analytical techniques can be used to identify phases in alloys, and the technique that is most useful is largely dependent upon the size of the phase considered. Light microscopy and x-ray diffraction (XRD) can be used if the phase is sufficiently large.<sup>8,39</sup> Typically, scanning electron microscopy (SEM) and energy-dispersive x-ray spectroscopy (EDS/EDX) are sufficient for most phase identification, though transmission electron microscopy (TEM) and atom probe tomography (APT) may need to be used for phases in the tens of nanometer size range.<sup>39–41</sup>

Samples for analysis using light microscopy and SEM can be prepared using conventional grinding and polishing techniques, whereas those analyzed using TEM or APT may need to be polished using twin-jet polishing, electro-polishing or extracted using a focused ion beam (FIB).<sup>39</sup> Regardless of the scale, it is important to prepare the samples so as not to induce any defects, damage, or phase changes. For

example, insufficient lubricant during grinding may heat the sample sufficiently to change the microstructure, and the gallium ion beam used in most FIB's may cause damage to the structure and even penetrate the lattice, distorting measurements.

TEM and APT are more advantageous for identifying smaller phases than SEM due to the smaller interaction volume of the beam, which increases resolution. Both TEM and APT can achieve atomic-level resolution, though very careful and time-consuming sample preparation is required. Sample thickness plays a significant role in the resolution capabilities, though Barbosa et al was able to identify a Q-phase precipitate 50nm in length using EDS.<sup>42</sup>

#### 5.4.2 Phase Identification of Al 2024, 6061, and 7075 Powders

Formation of intermetallic phases is inevitable in aluminum alloys; they can form during solidification from the liquid, during cooling after solidification or during heat treatments.<sup>43</sup>

Due to the highly metastable conditions present in rapidly solidified powders and the potential for large variations in local compositions, it is important to consider all intermetallic phases containing the elements present in the alloys considered, not just those conventionally present in those alloys. The alloys considered are 2024, 6061, and 7075, all containing varying amounts of Al, Cr, Cu, Fe, Mg, Mn, Si, and Ti.  $\text{Al}_2\text{Cu}$  ( $\theta$ ), with its precursors  $\theta''$  and  $\theta'$  are the primary strengthening phases in 2xxx alloys. As mentioned in the Handbook of Aluminum, in 6xxx alloys,  $\text{Mg}_2\text{Si}$  ( $\beta$ ) is the equilibrium phase, with precursor  $\beta'$  and  $\beta''$ .<sup>4</sup> In 7xxx alloys, there are several precipitation sequences that may occur, depending on the exact alloy composition and local concentrations.  $\text{Al}_2\text{CuMg}$  ( $S$ ),  $\text{Mg}_{32}(\text{Al}, \text{Zn})_{49}$  ( $T$ ), and  $\text{MgZn}_2$  ( $\eta$ ) may be the predominant equilibrium phases with precursors  $T'$  and  $\eta'$ . In addition to elemental concentrations, cooling rate has been shown to have an effect on the size, morphology, and distribution of the intermetallics.<sup>41</sup>

$\text{Al}_2\text{Cu}$  ( $\theta$ ) can be present as block-shaped, eutectic structure, or a mixture of both; which shapes are present is largely dependent upon the amount of Mg present.<sup>39,44</sup>  $\theta'$  is a plate-like, tetragonal phase, while  $\theta''$  is much finer and no conclusive structure has been identified yet.<sup>44,45</sup> Additionally, the structure of  $\text{Al}_2\text{Cu}$  is inconclusive, having been identified as monoclinic, orthorhombic, hexagonal, and tetragonal.<sup>44</sup>

$\text{Mg}_2\text{Si}$  ( $\beta$ ) is the equilibrium phase, with precursors  $\beta'$  and  $\beta''$ .  $\beta''$  is monoclinic in structure and is needle-like in shape,  $\beta'$  is has a hexagonal crystal structure and rod-like morphology, and  $\beta$  ( $\text{Mg}_2\text{Si}$ ) has a cubic crystal structure with a coarse morphology.<sup>46,47</sup> Depending upon the exact Cu:Mg:Si ratios,  $\text{Al}_2\text{Cu}$  and Q-phase ( $\text{AlCuMgSi}$  precipitate) may form more readily than the beta phases.

$\text{Al}_2\text{CuMg}$  ( $S$ ) and  $S'$  are orthorhombic, with  $S$  found primarily at the grain boundaries and  $S'$  primarily in the grain interiors.<sup>39</sup> There is little difference in the lattice strain between the two phases, though  $S'$  tends to be a finer needle-like precipitate with  $S$  being coarser. The shape of  $S$  phase has been shown to be dependent upon the Cu:Mg ratio, where higher ratios results in more lath-like structures.<sup>48,49</sup>

$\text{MgZn}_2$  ( $\eta$ ) is hexagonal and needle-shaped, while its precursor  $\eta'$  has a plate-like structure and is also hexagonal.<sup>39,50</sup>  $\eta'$  is believed to have lattice parameters similar to aluminum, which often makes it full coherent with the aluminum matrix. Diffraction spots from  $\eta'$  are typically very weak compared to the aluminum matrix, making it difficult to identify.<sup>51</sup> Additionally, if the Zn:Mg ratio is high, then  $\text{Mg}_2\text{Zn}_{11}$

will form instead and is cubic in structure.<sup>48</sup>  $Mg_{32}(Al, Zn)_{49}$  (T phase) is also reported in literature, but is seen as an idealized stoichiometric composition of  $MgZn_2$ .<sup>39,52</sup>

$\alpha$ -AlFeMnSi typically forms in the interdendritic channels via eutectic decomposition ( $L \rightarrow \alpha$ -Al +  $\alpha$ -AlFeMnSi) and has a bcc crystal structure. Coarse  $\alpha$ -AlFeMnSi form during solidification, medium sized  $\alpha$ -AlFeMnSi form during heating. Barbosa et al found  $\alpha$ -AlFeMnSi in 6061, though it is not typically seen in this alloy.<sup>42</sup> Variations in the local concentration of Fe can dictate which phase forms. If the local concentration of Fe is low compared to the concentration of Mn, then the  $Al_{12}Mn_3Si$  phase forms, whereas if the concentration of Fe is higher,  $\alpha$ -AlFeMnSi forms.<sup>53</sup>  $Al_{12}Mn_3Si$  has a simple cubic structure, stable phase, granular shape.<sup>41</sup> If there is a low Si concentration, then  $Al_6Mn$ , or  $Al_6FeMn$ , will form instead.<sup>54</sup> This has a plate-like shape, is orthorhombic in structure, and is the metastable precursor to  $Al_{12}Mn_3Si$ .<sup>41</sup>

Q-phase, an AlCuMgSi precipitate, is common in aluminum alloys containing Al, Cu, Mg, and Si, though there is little conclusive information of the phase in literature. If the Cu content is close to 1wt% is when it will form.<sup>53</sup> If the Cu content is higher, more  $Al_2Cu$  will form instead.<sup>46</sup> Its stoichiometric composition is widely discussed, and ranges from  $Al_4Cu_2Mg_8Si_7$  to  $Al_4Cu_1Mg_5Si_4$ .<sup>48</sup> It is generally thought that Q-phase has a hexagonal crystal structure and its precursor, Q', has been seen to be lathe shaped.<sup>42</sup>

The structures, shapes and presence of these phases can be used in Section 7.4 - Phase Identification via experimentation and modelling.

## 5.5 3D Characterization

Serial sectioning and 3D analysis are not new concepts but have been increasing in recent years due to advancements in more powerful equipment, software, and automation of these processes.<sup>55-57</sup> In many instances, 2D sections are sufficient for microstructural analysis, but there are an increasing number of applications in which it is important to understand the 3D microstructure. Such applications include the interconnectedness of networks (pores, segregation, secondary phases), shapes and anisotropy of features (particles, grains, precipitates), and the spacing and distribution of those features.<sup>58,59</sup> Additionally, modeling processes typically utilize volume fraction (rather than area fraction), and 3D tomography can provide that information accurately.<sup>26,60</sup>

Commercial methods have been developed, perhaps most widely known is RoboMet3D developed by the US Air Force Research Laboratory. This utilizes a robotic arm to automate the polishing, etching, and imaging with light microscopy of mounted samples. The process can perform slices of thicknesses between 0.1-10 $\mu$ m.<sup>61,62</sup> On a smaller scale, FEI has developed automatic software to mill and image in a dual-beam FIB.<sup>63</sup> This method has the ability to perform slice thicknesses of 10nm-1 $\mu$ m, and can incorporate a variety of types of electron imaging (back scatter, secondary, EDS, and EBSD).

Focused Ion Beam (FIB) tomography in dual beam FIB-SEM microscopes is the most popular method for obtaining 3D microstructures as it has high site-specific precision and can obtain high magnifications as well. However, the common Ga ion beam can only provide depths on the order of tens of microns in dimension. Plasma Xe ion beams have increased in popularity due to their ability to offer the same benefits as a Ga ion beam but with the added benefit of providing depths on the order of hundreds of microns in dimension and increased milling efficiencies.<sup>58</sup> Additionally there is little to no beam damage, so the surfaces are of high quality for electron backscatter diffraction (EBSD) analysis.<sup>58,64</sup>

In direct relation to this study, Uchic et al provide a process for utilizing a dual-beam FIB for automated serial sectioning with EBSD to study nickel superalloys, Lin et al have used mechanical polishing and SEM to study the granular structure commercially pure aluminum, and Soppela et al utilized white light illumination to study the particle shape and surface roughness of organic powder samples.<sup>63,65,66</sup> Zaefferer et al have used the 3D EBSD FIB technique to analyze the effect of various features on the grain orientation and structure of copper and iron based materials.<sup>67,68</sup> Specifically, they have evaluated the change in texture below a nanoindent and the change in orientation around a precipitate. However, no work has been published regarding aluminum powder.<sup>66</sup>

## 6 Experimental Work

This work has been submitted in part for publication as:

**C. Walde**, B. Sousa, V. Champagne, & D. Cote. An Evaluation of Gas Atomized Aluminum Alloy Powders as Compared to Cast Counterparts. *Metallurgical and Materials Transactions A*. Under Review.

### 6.1 Cast versus Powder

Metal additive manufacturing has emerged as a disruptive force within the advanced manufacturing sector. The technology's development is largely attributable to research concerned with the optimization of existing additive methods or the design of novel approaches for an application. Research has shown that, for certain metal additive manufacturing techniques, the properties of the feedstock powder affect the properties of the consolidated material. Understanding the powder characteristics before use in additive manufacturing could lead to fine-tuning the properties of additively manufactured materials. Recent consideration has been given to the prospect of advancing additive manufacturing further by 1) designing alloys specific to an additive process and 2) better understanding commercially available feedstock compositions. In support of the latter effort, three commercially available Al aerospace alloy systems were studied to showcase the differences in the properties of a bulk alloy as compared with a powder feedstock material with the same designation.

Optical microscopy, scanning electron microscopy, nanoindentation, microhardness testing, differential scanning calorimetry, elemental analysis, and cooling rate calculations were utilized during this effort. The properties of the gas atomized Al 2024, Al 6061, and Al 7075 powders, in comparison to their cast counterparts, were found to be different from one another. Differences were observed in terms of their microstructure, mechanical response, and kinetic behavior during thermal treatments. This work confirms initial findings that powder alloys may not be treated the same way as their cast counterparts, providing a comprehensive understanding of feedstock powder properties to improve effectivity of additive manufacturing processes.

#### 6.1.1 Materials and Methods

##### 6.1.1.1 Cooling Rate Calculations for Powder

Gas atomization is known to achieve cooling rates as high as  $10^7$  °C/sec.<sup>69</sup> Since the rate of cooling during gas atomization is orders of magnitude greater than those reported for castings, the classical models relating microstructure to cooling rates cannot be directly applied to rapidly solidified powders. As such, a relatively simple heat transfer model, which was reported by He et al.<sup>70</sup>, was found to be adequate in capturing the mechanisms behind single particle solidification during atomization. The simplified heat transfer model for rapidly solidified powders is given in Equation 1.

$$\frac{dT_d}{dt} = \frac{12}{\rho C_p} (T_d - T_g) \frac{k_g}{d^2} \quad \text{Equation 1}$$

Where  $T_d$  is the molten metal droplet temperature in °K;  $t$  is the time in seconds;  $T_g$  is the gas atomizing temperature in °K;  $\rho$  is the droplet density in kg/m<sup>3</sup>;  $C_p$  is the specific heat of the metal

droplet in J/(kg°K);  $k_g$  is the thermal conductivity of the gas species utilized during atomization in W/(m°K); and  $d$  is the droplet diameter in m. It follows that the cooling rate is inversely proportional to the droplet diameter as shown in Equation 2.

$$\frac{dT_d}{dt} \propto d^{-2} \quad \text{Equation 2}$$

Table 1 tabulates the droplet density ( $\rho$ ), molten metal droplet temperature ( $T_d$ ) and specific heat of the metal droplets ( $C_p$ ) for each of the Al alloys.

Table 1: Droplet density ( $\rho$ ), molten metal droplet temperature ( $T_d$ ) and specific heat of the metal droplets ( $C_p$ ) for each of the Al alloys.

Alloy	Droplet Density (kg/m <sup>3</sup> )	Molten Metal Droplet Temp. (°K)	Specific Heat (J/kg°K)
2024	2270	1473	1140
6061	2700	1473	896
7075	2810	1473	960

In casting metallurgy, there is a proven relationship between secondary dendrite arm spacing and solidification (Equation 3),

$$\lambda_x = \lambda_{o_x} \left( \frac{dT}{dt} \right)^{-n} \quad \text{Equation 3}$$

Where  $\lambda_{o_x}$  and  $-n$  are alloy-dependent constants. The materials property simulation software JMatPro® (Sente Software, Guildford, UK; Version 9.1.1) was used to determine  $\lambda_o$  and  $-n$  for Al 2024, Al 6061 and Al 7075:  $\lambda_{o_{2024}} = 86.741$ ,  $\lambda_{o_{6061}} = 99.853$ , and  $\lambda_{o_{7075}} = 90.049$ . A value of 0.33 was used for  $n$  for all of the alloys.

In an effort to relate the powder particle cooling rates with their microstructural feature sizes, Equations 1 and 3 were combined, resulting in the relationship in Equation 4.<sup>31</sup>

$$\lambda = \lambda_o \left( \frac{12}{\rho C_p} (T_d - T_f) \frac{k_g}{d^2} \right)^{-n} \quad \text{Equation 4}$$

#### 6.1.1.2 Cooling Rate Relations for Castings

With respect to the alloys in their cast conditions, thermocouples were used to experimentally determine the cooling rates experienced during solidification upon casting. According to Ghoncheh et al.<sup>71</sup>, the relationship between dendrite arm spacing and cooling rate for cast Al 2024 is given in Equation 5.

$$DAS = 46.51 \left( \frac{dT}{dt} \right)^{-0.59} \quad \text{Equation 5}$$

Where DAS is the dendrite arm spacing in  $\mu\text{m}$  and  $dT/dt$  is the cooling rate. In the case of Al 6061 and Al 7075, the DAS relation given in Equation 6 is a reasonable approximation.<sup>71</sup>

$$DAS = 45.00 \left( \frac{dT}{dt} \right)^{-0.39} \quad \text{Equation 6}$$

### 6.1.1.3 The Casting Process

Al 2024, Al 6061, and Al 7075, were purchased as sheets, subsequently melted and cast in-house into cylinders with 28 mm diameters. The cooling rates were measured in the center of the cylinder. Optical emission spectrometry (OES) was used to measure the compositions of the three as-cast alloys (Table 2, Table 3, and Table 4). The OES was made by SPECTRO Analytical Instruments (Germany).

Table 2: Compositions of the powders and cast samples, compared to the ASM standard, for Al 2024.

Element	2024		
	Cast	ASM	Powder
Cr	0.197	< 0.10	0.0051
Cu	0.012	3.80 – 4.90	3.83
Fe	0.291	< 0.50	0.065
Mg	2.25	1.20 – 1.80	1.51
Mn	0.06	0.30 – 0.90	0.54
Si	0.142	< 0.50	0.13
Ti	0.011	< 0.15	0.0029
Zn	< 0.001	< 0.25	0.013
Al	97.00	Bal.	93.904

Table 3: Compositions of the powders and cast samples, compared to the ASM standard, for Al 6061.

Element	6061		
	Cast	ASM	Powder
Cr	0.19	0.04 – 0.35	0.087
Cu	0.164	0.15 – 0.4	0.25
Fe	0.373	< 0.7	0.27
Mg	0.66	0.8 – 1.2	0.95
Mn	0.06	< 0.15	0.34
Si	0.52	0.4 – 0.8	0.49
Ti	0.019	< 0.15	0.024
Zn	0.024	< 0.25	0.035
Al	98.00	Bal.	97.554

Table 4: Compositions of the powders and cast samples, compared to the ASM standard, for Al 7075.

Element	7075		
	Cast	ASM	Powder
Cr	0.201	0.18 – 0.28	0.20
Cu	1.36	1.2 – 2.0	1.59
Fe	0.151	< 0.5	0.17
Mg	2.21	2.1 – 2.9	2.50
Mn	0.027	< 0.3	0.26
Si	0.059	< 0.4	0.15
Ti	0.03	< 0.2	0.029
Zn	4.94	5.1 – 6.1	5.71
Al	91.022	Bal.	89.391

#### 6.1.1.4 Gas Atomized Aluminum Powders

Each of the alloyed powders were gas atomized in nitrogen by Valimet, Inc. (Stockton, CA). The cooling rate during this process was on the order of  $10^4 - 10^5$  °C/s. The received powders were mechanically sieved from the initial distribution to the studied ranges, with  $d_{10}$ ,  $d_{50}$ , and  $d_{90}$  as shown in Table 5. The compositions of the powders were evaluated using direct current plasma emission spectroscopy as performed by Luvak Inc. (Boylston, MA) and presented in Table 2, Table 3, and Table 4.

Table 5: Size distribution characteristics for each of the alloy powders.

Alloy	$d_{10}$ (μm)	$d_{50}$ (μm)	$d_{90}$ (μm)
2024	18.5	34.2	57.8
6061	33.8	41.2	54.3
7075	26.1	37.1	52.9

#### 6.1.1.5 Thermal Processing

Heat treatment was performed on one set of samples at a time in a differential scanning calorimeter (DSC) for its highly accurate temperature control. One set of samples was left untreated as a control. Cast samples were cut to fit into DSC crucibles, with two parallel flat sides. Heat treatments were performed using a heating rate of 50 °C/min and a cooling rate of 120 °C/min. Samples were brought to the treatment temperature determined for each alloy (Al 2024 = 490 °C; Al 6061 = 530 °C; Al 7075 = 480 °C) and held for one hour before being quenched. Nitrogen was used as the purge gas. Specifically, a TA Instruments Discovery DSC with LN2P cooler was used. Since the powders provided by Valimet were atomized in nitrogen gas, the  $k_g$  is 0.024 W/m<sup>2</sup>K while the  $T_f$  is 300 °K for cooling rate calculations.

6.1.1.6 *Experimental Characterization*

The grain size of the samples was characterized via etching and subsequent light microscopy. For etching, samples were compression mounted in a phenolic resin and polished with a 0.05 um colloidal silica suspension. Once polished, the samples were etched using the reagents and times described in Table 6. Grain size was then measured using light microscopy micrographs and Olympus Stream’s software package for grains and intercepts. To reduce the distortion due to the curvature of the powder particles, only features near the center of the front face of the powders were included in the measurements. Also, due to the contribution of the secondary dendrite arm spacing measurement, grains were measured in a comparable method: from the center of the grain boundaries to the center of the grain.

Table 6: Etching procedure for each alloy, for both powder and cast.

Alloy	Reagent	Etching Time	
		Powder	Cast
2024	Keller’s Reagent (1.0% hydrofluoric acid, 1.5% hydrochloric acid, 2.5% nitric acid, 95.0% distilled water)	5 seconds	35 seconds
6061	0.5% hydrofluoric acid; 99.5% distilled water	1 minute	2 minutes
7075	Keller’s Reagent (1.0% hydrofluoric acid, 1.5% hydrochloric acid, 2.5% nitric acid, 95.0% distilled water)	5 seconds	17 seconds

Samples were prepared for SEM the same way they were prepared for etching. SEM micrographs were taken using a tungsten-source SEM (EVO MA-10, Carl Zeiss Microscopy, Thornwood, NY). Both secondary electron (SE) and backscattered electron (BSE) images were taken. The BSE images were used to evaluate the amount of secondary phases present in each condition. This was accomplished by contrast thresholding using image analysis software.

Nanoindentation testing was performed using an iMicro Pro system from Nanomechanics, Inc. (Oakridge, TN) on the powder samples. The InForce 50 actuator (<http://www.nanomechanicsinc.com>) was employed with a diamond Berkovich tip from Micro Star Technologies Inc. (Huntsville, TX). 25 particles were selected for indentation testing per sample. To accommodate for the known indentation size effect, hardness measurements were reported at indentation depths of 200 nm using the dynamic advanced hardness and modulus method provided by Nanomechanics, Inc.<sup>72</sup> Using standard methods, the tip was cleaned, and the contact area function was analytically calibrated via load vs. depth data from a fused Si sample.

Microhardness testing was performed with a DiaMet Hardness Tester from Buehler (Lake Bluff, Illinois) on the cast samples. The microhardness data was collected using a Vickers indenter tip with applied force of 0.1 kgf / mm<sup>2</sup>. Inspired by and modeled from the Vickers tip geometry, Berkovich shaped nanoindentation tips have become commonplace for testing materials with elastic moduli greater than 500 MPa. Since each tip geometry has essentially the same contact area also result in 8% strains during indentation, the nanoindentation hardness is readily converted to a Vickers Hardness Number via the following relation.

$$HVN = 0.0945 * H_{NI}$$

Where HVN is the Vickers Hardness Number and  $H_{NI}$  is the nanoindentation hardness with units in MPa. Therefore, the nanoindentation hardness's are directly converted to an HVN value for direct comparison with the microhardness responses for the cast conditions.

DSC analysis was performed on the samples at a heating rate of 5 °C/min in a nitrogen environment.

## 6.1.2 Results and Discussion

### 6.1.2.1 Cooling Rate Comparisons

The cooling rates as a function of particle size for each of the gas atomized alloy compositions considered is presented in Figure 1.

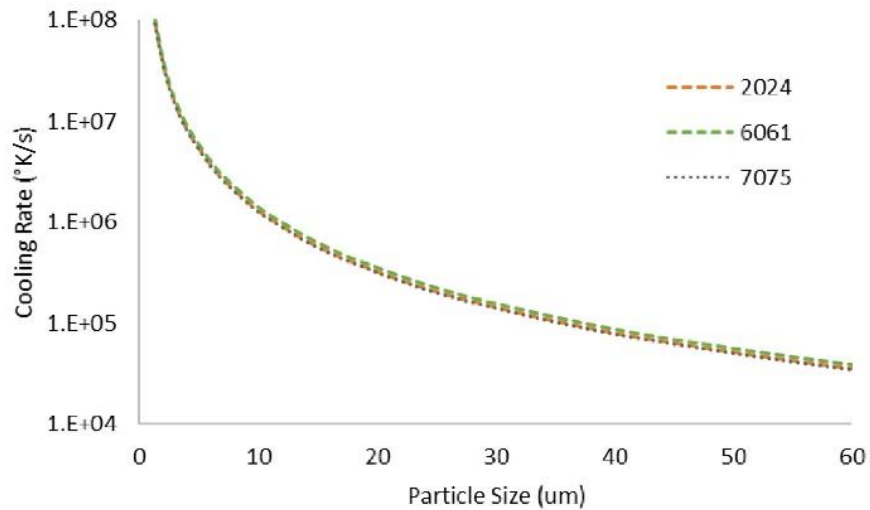


Figure 1: Cooling rate as a function of particle size for each of the gas atomized alloys.

Part A of Figure 2 shows the temperature of the three casts as a function of time, which speaks to the cooling rates experienced by the cast materials in contrast to the rapidly solidified powders. Finally, Part B of Figure 2 contrasts the cast cooling rates with time. The cooling rates expected in both cases are consistent with those presented in earlier works.<sup>73</sup>

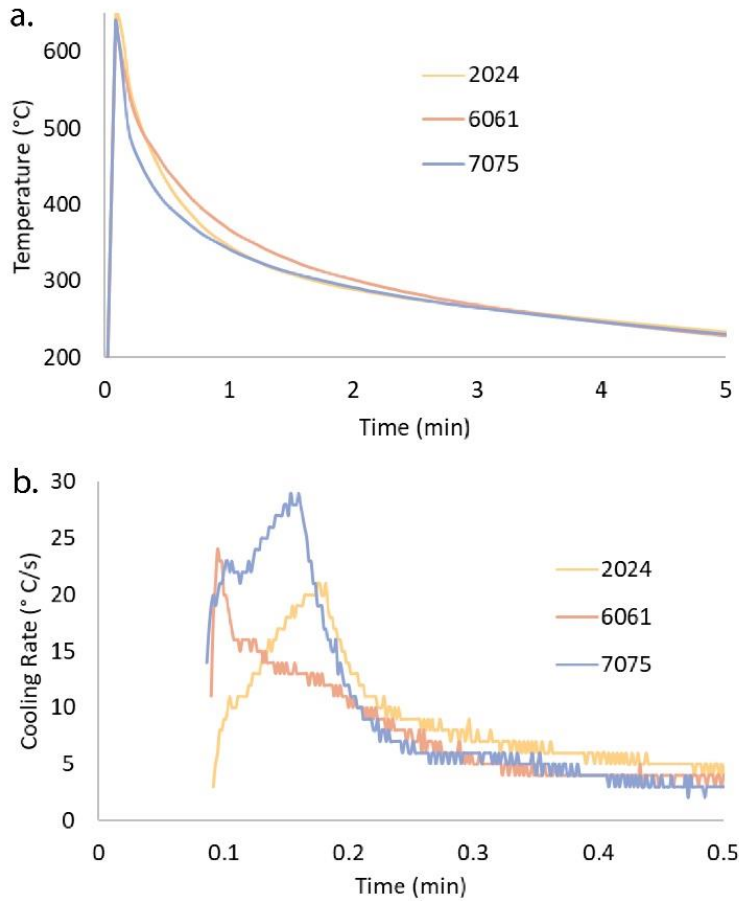


Figure 2 a) Temperature as a function of time for each alloy during casting, and b) calculated cooling rate as a function of time for each alloy during casting.

Parts A through C of Figure 3 presents the experimentally measured as well as predicted feature sizes as a function of particle size for Al 2024, Al 6061, and Al 7075 respectively.

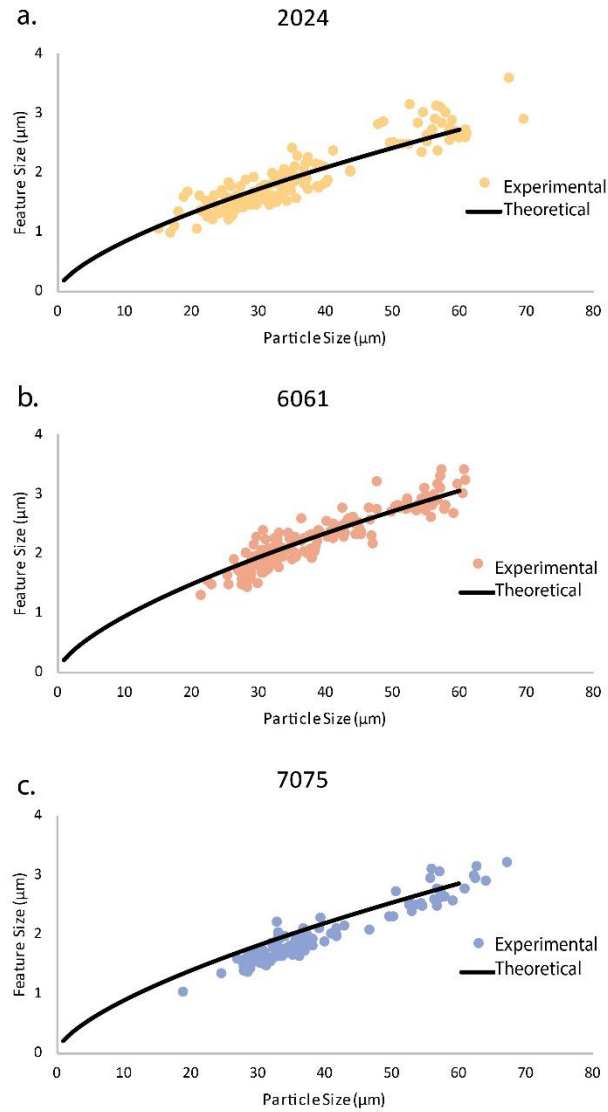


Figure 3: Feature size as a function of particle size, both predicted and theoretical, for a) 2024, b) 6061, and c) 7075.

#### 6.1.2.2 Compositions and Kinetics

The experimentally derived chemistries of the gas atomized powders as well as the as-cast samples are compared to the standard compositional ranges defined by ASM International.<sup>32</sup> Table 2, Table 3, and Table 4 present the chemical compositions of each alloy.

Parts A through C of Figure 4 serve to highlight the differences in kinetics, via DSC data, between the alloys in their powder and cast forms.

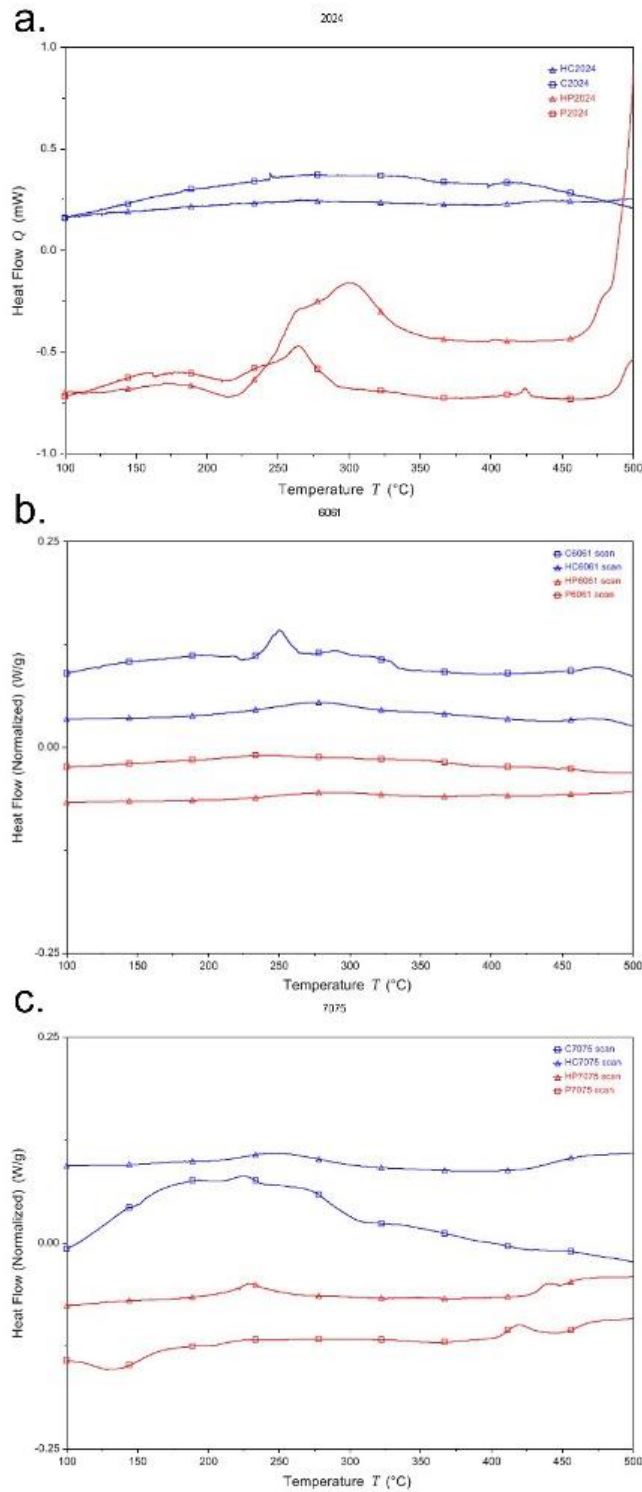


Figure 4: DSC thermograms of cast and powder samples in both the control and thermally treated conditions, for a) 2024, b) 6061, and c) 7075. Example: C7075 = as-cast; HC7075 = thermally treated cast; P7075 = as-atomized 7075; HP7075 = thermally treated powder.

### 6.1.2.3 Microstructural Analysis

Figure 5 shows example optical micrographs for Al 7075 after etching; part A shows the as-atomized powder condition and part B shows the as-cast condition.

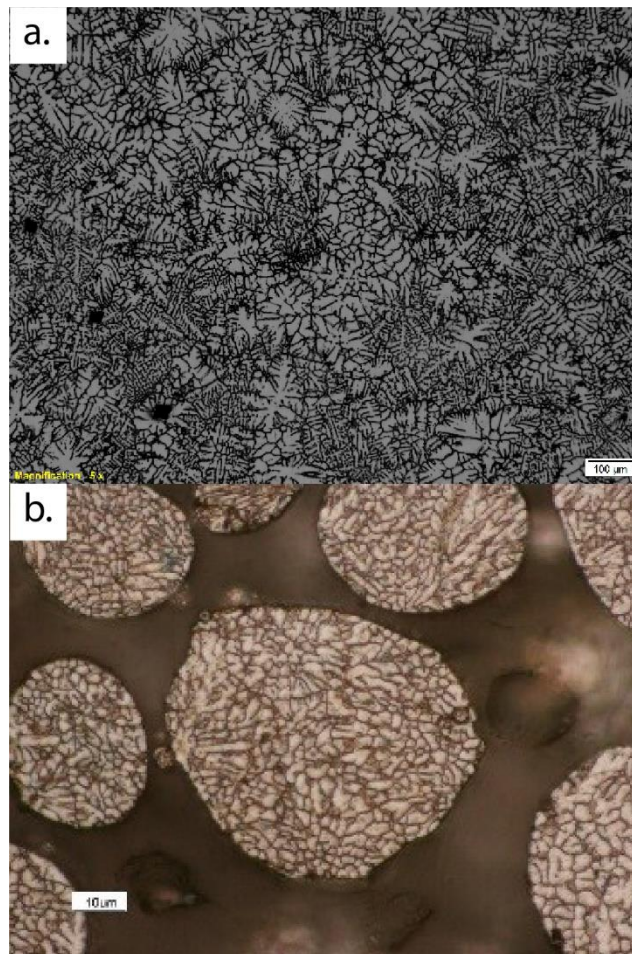


Figure 5: Optical micrograph of Al 7075 after etching, a) as-atomized powder and b) as-cast.

Figure 6 compares the microstructures of the as-cast, as-atomized, thermally treated cast, and thermally treated powder via SEM for Al 7075.

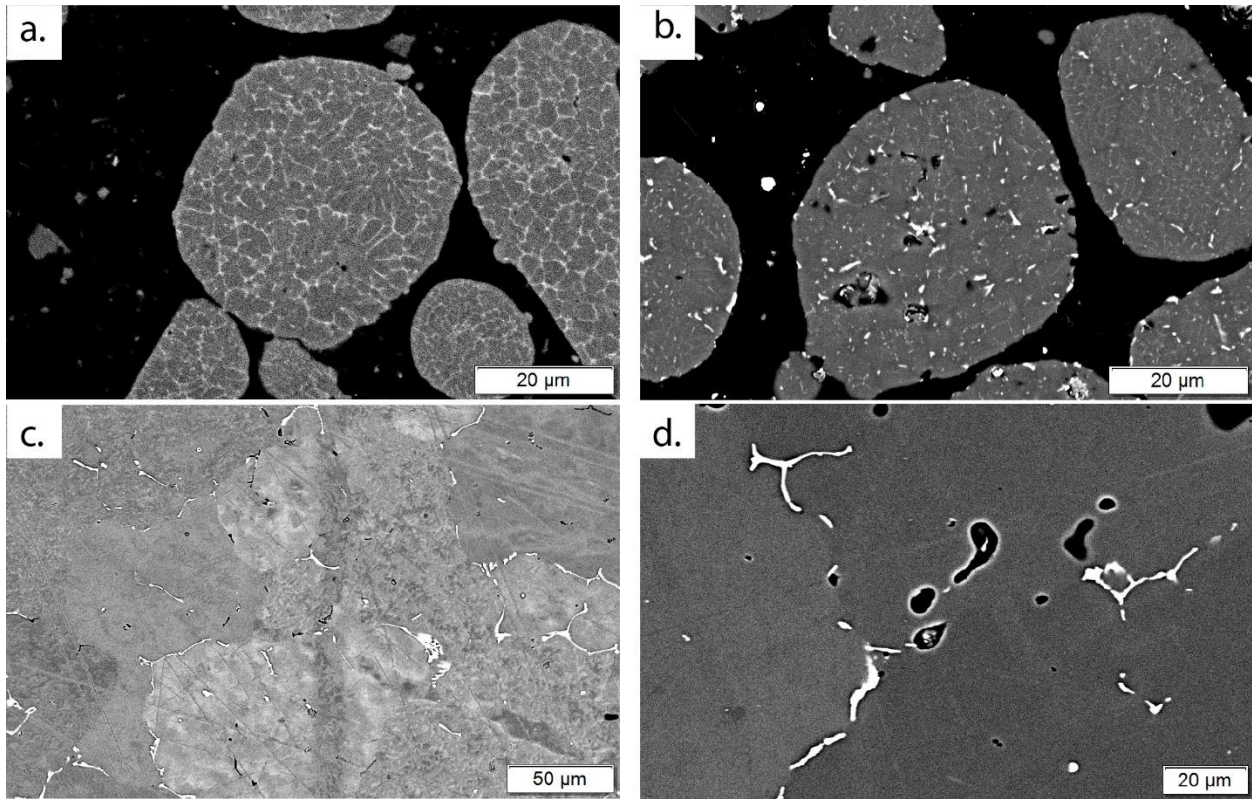


Figure 6: SEM micrographs of Al 7075 a) as-atomized powder, b) thermally treated powder, c) as-cast, and d) thermally treated cast.

The secondary phase area percent of each alloy is presented in relation to each of the conditions studied herein. More specifically, the phase area percentages for the as-cast, as-atomized, thermally treated casts, and thermally treated powders are shown in Figure 7. The figure is further refined in terms of the Mg or Fe richness of each of the phases analyzed.

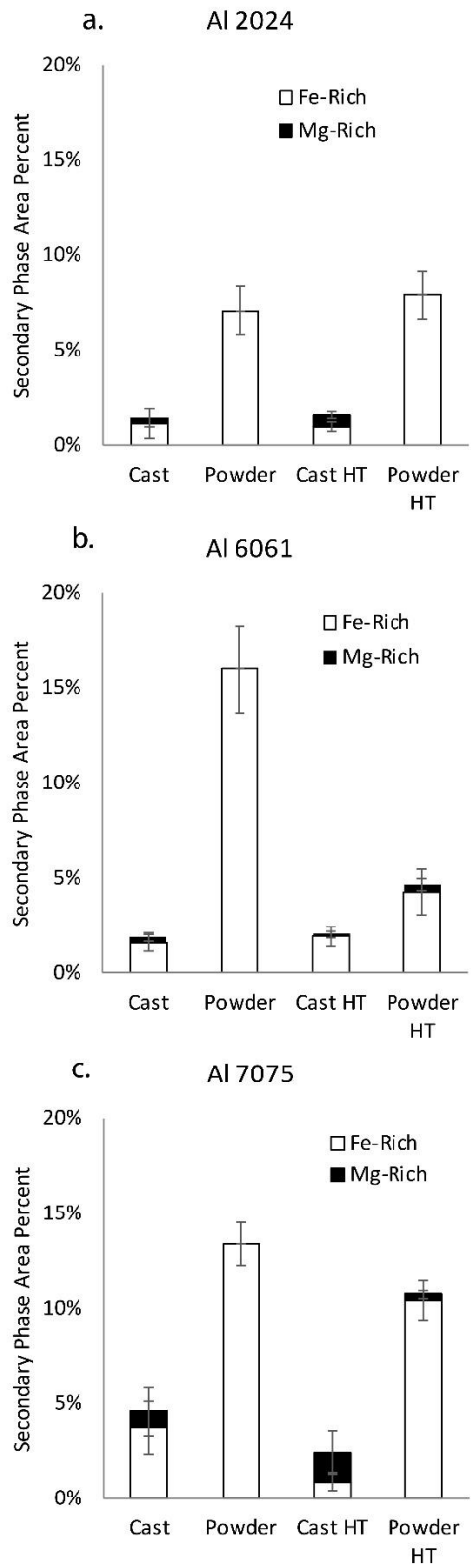


Figure 7: Phase area percentages for the as-cast, as-atomized, and thermally treated cast and powders for a) 2024, b) 6061, and c) 7075.

The microstructural feature sizes for the three alloys are given in Figure 8. Like Figure 7, Figure 8 presents the features sizes for each of the conditions, which includes the as-cast, as-atomized, thermally treated casts, and thermally treated powders.

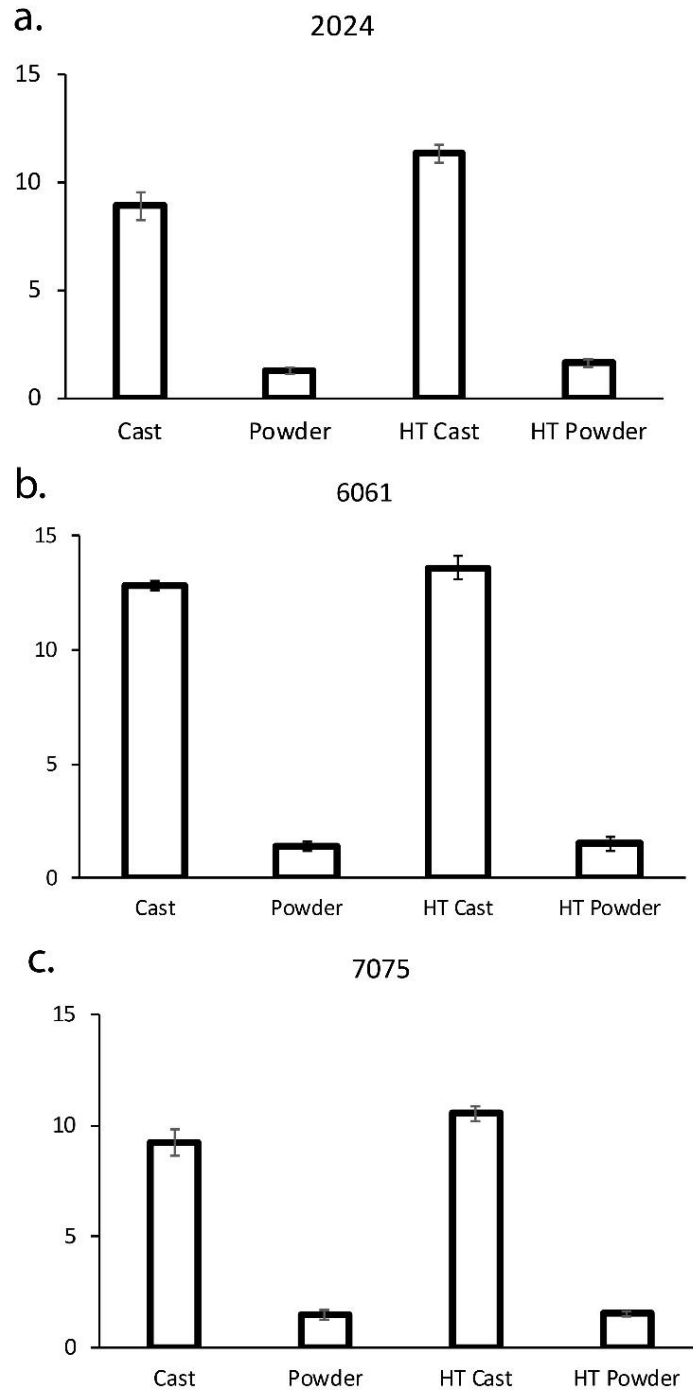


Figure 8: Microstructural feature size for the as-cast, as-atomized, and thermally treated cast and powders for a) Al 2024, b) Al 6061, and c) Al 7075.

#### 6.1.2.4 Mechanical Behavior

Lastly, the Vickers Hardness numbers for each of the alloys in all four conditions are given in Figure 9.

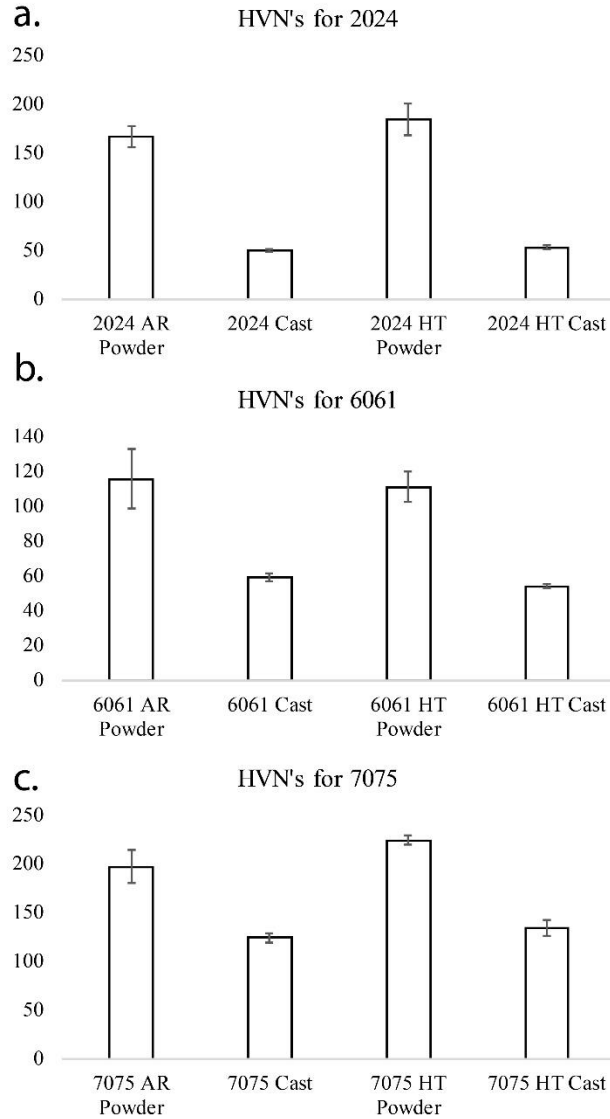


Figure 9: Vickers Hardness numbers for the as-cast, as-atomized, and thermally treated cast and powders for a) Al 2024, b) Al 6061, and c) Al 7075.

#### 6.1.2.5 Al 2024 Powder vs. Cast

With respect to the compositional specification limits (Table 2) for Al 2024, the OES recorded data for the as-cast condition is out of specification with respect to the measured Cr, Cu, and Mn contents. However, the chemical makeup of the Al 2024 as-atomized powder agrees with the standard alloying chemistry defined by ASM. Though the compositions measured for the as-cast Al 2024 is outside of specifications, the variation is attributed to contamination of the OES, and the study between the cast and powder is still an interesting one.

The DSC data (Figure 4) as well as the secondary phase area fraction results (Figure 7) speak to the difference in kinetics between the cast and powder forms of the alloy. For atomized Al 2024, in both the heat treated and as-received conditions, there exists multiple points along the DSC scan that suggest precipitation and dissolution of additional secondary phases. On the other hand, the DSC data for the as-cast and thermally processed conditions demonstrate little to no secondary phase activity.

From Figure 7, the secondary phase area fraction of the powder in both conditions is shown to be approximately four times greater than their cast counterparts. The difference in secondary phase area fraction highlights the critical role cooling rates play in determining the microstructure of the material as well as its' compatibility with thermal processing. Additionally, the heat-treated cast sample experienced an increase in Mg rich precipitate formation. Though Mg-based precipitation and dissolution is certainly at play in the atomized powder earlier work has shown that the phases are too small compared to the interaction volume of the electron beam.<sup>74,75</sup>

In much the same way the secondary phase formation speaks to the influence of cooling rate upon the as-atomized and as-cast microstructures, the polycrystalline feature sizes also attest to the dominating role of cooling rate. Shown in Figure 8, the feature size of Al 2024 in each condition is presented. In comparison to the as-cast data, the feature size measured via optical microscopy of chemically etched cross-sections appears to be about four times smaller. Post thermal processing, a small annealing effect is seen between the as-cast and thermally treated cast sample. As for the two powder conditions, a negligible difference in feature size can be discerned from the data.

The experimental and computational feature sizes plotted as a function of powder cooling rate and in relation to particle diameter reinforces the current rapid solidification theory. That said, the measured grain size of the as-cast Al 2024 sample also agrees well with the calculated feature size from the cooling rates collected using a thermocouple (Figure 2). More specifically, the measured feature size was 8.92  $\mu\text{m}$  while the calculated feature size was 7.94  $\mu\text{m}$ .

As presented in Figure 9, the hardness of Al 2024 powder is approximately three times that of its cast counterpart. For both the powder and cast samples, thermal processing resulted in acute increases in the recorded Vickers Hardness Numbers.

#### *6.1.2.6 Al 6061 Powder vs. Cast*

Unlike the case of Al 2024, the as-cast composition of the 6061 sample was within specification thresholds except for the alloying element Mg according to Table 3. As for the as-atomized powder, the Mn content was found to be almost double that of the upper limit permitted according to ASM International. Contamination of the OES device could account for the recorded Mg value. However, contamination in the atomizer used to produce the rapidly solidified 6061 powder particles or an out-of-spec master alloy could be responsible for the overabundance of Mn as an alloying element.

In further contrast to 2024, the DSC (Figure 4) only revealed one precipitation occurrence out of all four conditions. In turn, little was gleaned from the DSC in terms of the difference in kinetics between the atomized and cast forms.

A significant change in the secondary phase area percent (Figure 7) of the 6061-powder occurred upon thermal processing. As shown, the Fe-rich precipitates dissolved upon processing to about twenty-five percent of the as-atomized phase area percent. At the same time, a noteworthy precipitation of Mg rich phases also occurred upon treating the powder. Regarding the cast samples, little to no change was observed.

As presented in Figure 8, the microstructural feature sizes of the cast 6061 samples, in comparison to the atomized samples, was found to be approximately seven times greater in diameter. As with 2024, a small annealing effect in the cast 6061 condition was observed after thermal processing. Yet negligible changes were found for the atomized powder in the as-received as well as heat treated conditions.

With a calculated feature size of 13.03  $\mu\text{m}$  and an experimental size of 12.84  $\mu\text{m}$  for the as-cast 6061 sample, this data echoes and compliments the observed agreement observed in the case of 2024.

In contrast to 2024, the cast and atomized 6061 VHN's decrease after thermal processing according to Figure 9. Recalling the significant decrease in secondary phase area percent for 6061 powders after thermal treatment, as presented in Figure 7, the observed decrease in hardness appears to correlate with the dissolution of a majority of the Fe rich intermetallic phases into the matrix solution.

#### *6.1.2.7 Al 7075 Powder vs. Cast*

The weight percent of each of the alloying elements in the as-atomized Al 7075 powders was found to be well within the specified compositional range as shown in Table 4. As for the as-cast Al 7075 sample, the weight percent of Zn fell short of the lower limit defined by the ASM compositional specification by 0.16 %. Like Al 6061 and Al 2024, contamination could have hindered the OES. Alternatively, the accuracy inherent to OES may account for this deviation within the data.

Unique in comparison to Al 6061 and Al 2024, the DSC scans revealed in Figure 4 highlight the difference in kinetics between the cast and powder conditions where there is only one broad precipitation peak in the cast data versus three precipitation peaks and one dissolution drop in the powder curves. Even more unique still is the trend found in Figure 7 as related to Al 7075. While the overall secondary phase area percent nearly decreases by fifty percent upon thermal processing of the cast samples, the heat-treated cast sample yields two times as much Mg rich phase area percent versus its' as-cast condition. That said, a small decrease in the phase area fraction is observed for the processed powder as well as an increase in the Mg rich secondary phase area percentage.

With respect to Figure 8 the same trend observed in Al 2024 was identified for Al 7075 in both the atomized and cast conditions; the thermally processed powder resulted in a greater VHN when compared to the as-atomized condition. To a lesser extent, the thermally treated cast sample also

experienced a slight increase in hardness. However, unlike Al 2024, the hardness values of the atomized powder is less than two times greater than its cast counterpart. The increase in hardness for both conditions is likely due to the precipitation of Mg rich phases upon thermal processing.

### 6.1.3 Summary and Conclusion

Three commonly used Al alloys in the aerospace industry were manufactured in two different processes. Each of the alloys were gas atomized as well as cast as a method of yielding a set of rapidly solidified morphologies in conjunction with classically solidified casts for Al 2024, Al 6061 and Al 7075. The as-atomized and as-cast samples were thermally processed according to the Materials and Methods section of the paper such that each of the alloys considered had four conditions for consideration: as-cast; as-atomized; heat treated cast; and thermally processed powder. The cooling rates experienced during atomization were modeled to predict the microstructural feature size as a function of particle diameter; said findings were plotted with experimentally obtained feature sizes and good agreement was seen. DSC scans as well as SEM-based secondary phase area fractions were determined for each condition studied per alloy to better understand the kinetics of powders in comparison to castings. Elemental analysis was performed and compared to widely accepted compositional ranges. The cross-sectional feature sizes were obtained from optical micrographs of the chemically etched samples. Lastly, the mechanical properties were obtained through indentation testing at the nano and micro scale for each of the three alloys.

In conclusion, each of the alloys showed vastly different properties as a function of cooling rate as well as processing approach, i.e. atomization vs. casting. Said otherwise, though the powder and cast morphologies of an alloy may have the same compositional chemistry or microstructural denotations, this study finds the properties of the two morphologies to be uniquely different from one another. The uniqueness was largely observed via secondary phase analysis, microstructural feature size measurements and calculations, variation in cooling rates, and the differences in mechanical behaviors. With this in mind, it is important to evaluate powders as their own material and develop thermal treatments specific for this condition, prior to use in any additive manufacturing technique.

## 6.2 Solution Treatment

Gas-atomized metallic powders are commonly used in additive manufacturing processes. Research has shown that, for certain AM techniques, the chemistry and microstructural properties of the feedstock powder significantly affect the properties of the consolidated material. Understanding the properties of the feedstock powder prior to use in additive manufacturing processes can lead to optimizing the properties of the consolidated materials as well as determining the recyclability of the feedstock powders. This research studies the effect of various solution treatment processes on the characteristics and microstructural evolution of powder aluminum alloys 2024, 6061, and 7075. Treatment times and temperatures were guided by thermodynamic and kinetic modeling. Light microscopy, scanning electron microscopy, and hardness were used to evaluate each condition.

### 6.2.1 Materials

The powder used for this study was the Al 2024, 6061, and 7075 that was used in Section 6.1 Cast versus Powder; see Section 6.1 Cast versus Powder for material details.

### 6.2.2 Method

#### 6.2.2.1 *Treatment Parameters*

Solution treatment temperatures were determined using Thermo-Calc software simulations (Stockholm, Sweden). The TCAL4 database was used to create an isopleth of the exact composition of the alloy under investigation. Figure 10, Figure 11, and Figure 12 show the equilibrium secondary phases in each of the alloys as a function of temperature. Although gas atomized powders are rapidly solidified and are thus not considered to be in an equilibrium state, this data was useful in determining the solution treatment temperature by predicting the melting temperatures of secondary phases. Additional experimental work, described in Section 0

Phase Identification, was performed to confirm which of these phases are present in the gas atomized powders.

Using Figure 10, a treatment temperature of 490°C was chosen for Al 2024. This temperature is high enough to dissolve unwanted phases (S phase,  $Al_9Fe_2Si_2$ ) while low enough to avoid melting. Six different solution treatment times were chosen (0 min, 20 min, 40 min, 60 min, 120 min, and 240 min) and one sample was left untreated (As-Atomized) as a control.

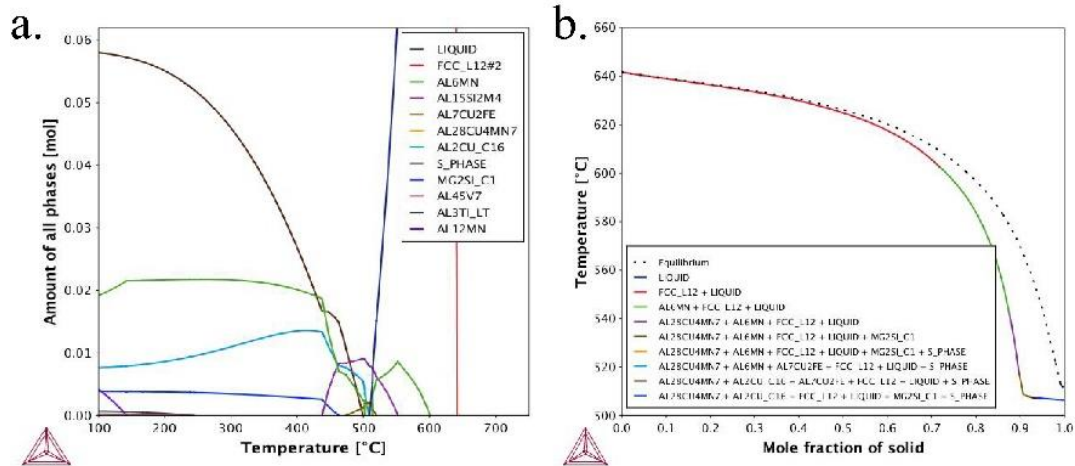


Figure 10: a) Equilibrium secondary phases in Al 2024 as a function of temperature and b) secondary phases predicted based on non-equilibrium conditions (Scheil solidification), as predicted by Thermo-Calc.

Using Figure 11, a treatment temperature of 530 °C was chosen for Al 6061. This temperature is high enough to dissolve unwanted phases ( $Mg_2Si$ ) while low enough to avoid melting. Six different solution treatment times were chosen (0 min, 20 min, 40 min, 60 min, 120 min, and 240 min) and one sample was left untreated (As-Atomized) as a control.

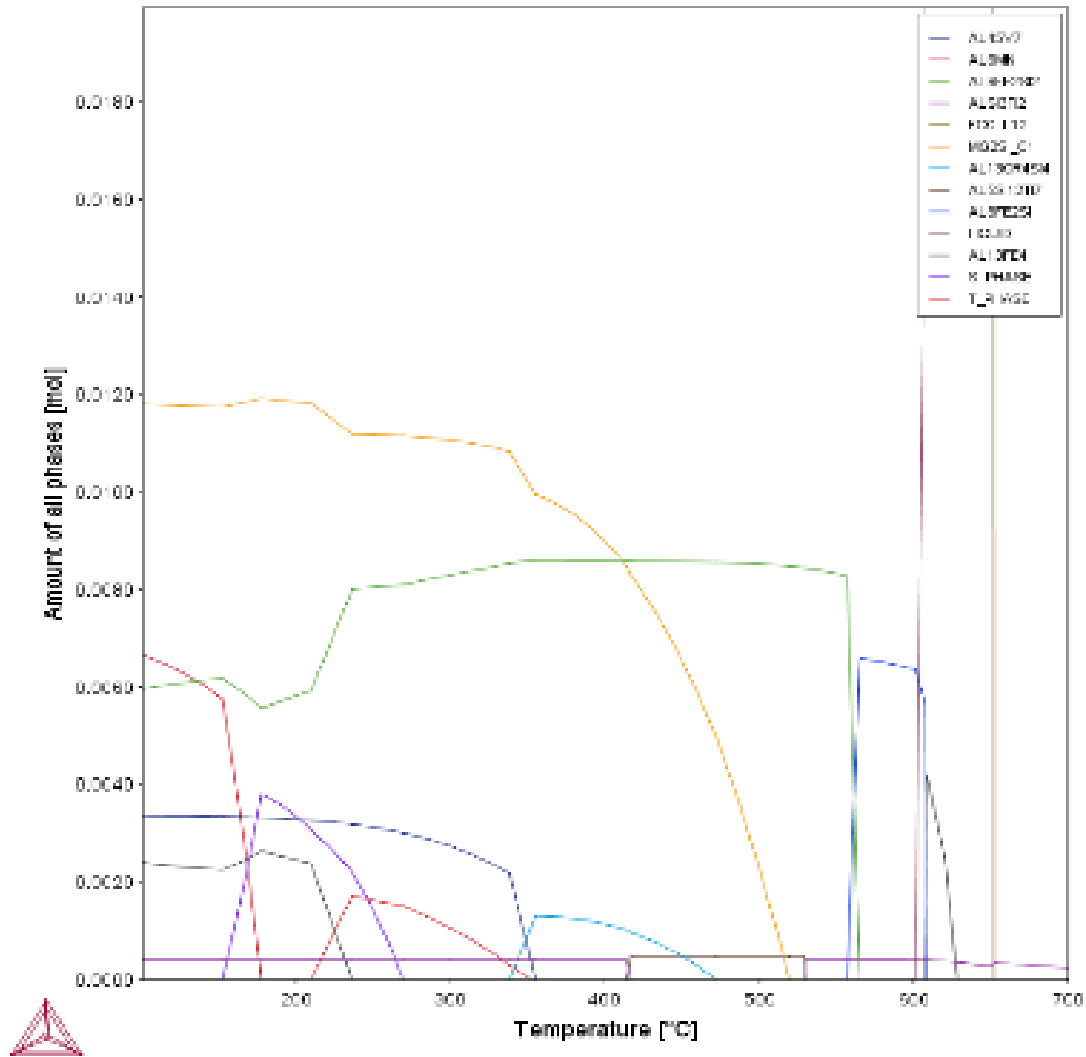


Figure 11: Equilibrium secondary phases in Al 6061 as a function of temperature as predicted by Thermo-Calc.

Using Figure 12, the temperatures of 465°C and 480°C were chosen for a case study comparison of two treatment temperatures. These temperatures were chosen with the goal of homogenizing the microstructure – dissolving T-phase while avoiding S-phase growth, avoiding  $\text{Al}_7\text{Cu}_2\text{Fe}$  coarsening, and avoiding melting. Six different solution treatment times were chosen (0 min, 20 min, 40 min, 60 min, 120 min, and 240 min) and one sample was left untreated (As-Atomized) as a control.

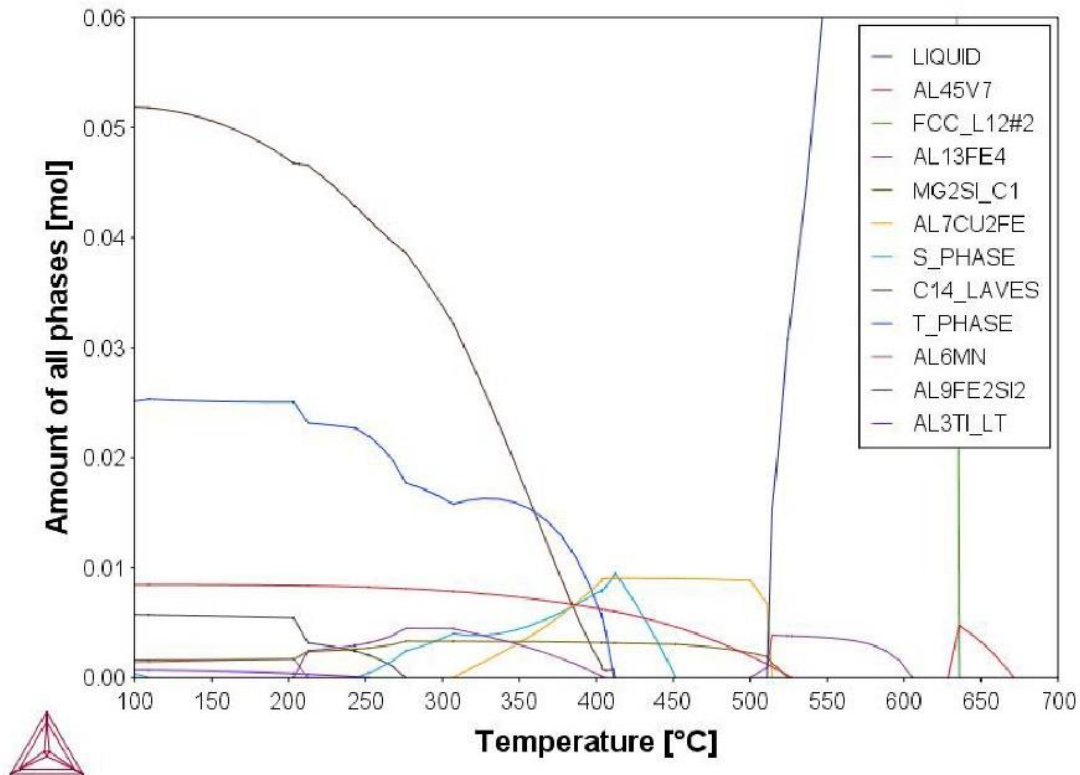


Figure 12: Equilibrium secondary phases in Al 7075 as a function of temperature as predicted by Thermo-Calc.

Samples were heated at 50°C/min to the determined temperature in a differential scanning calorimeter (DSC) for its' rigorous temperature control furnace, held for the given treatment time, then quenched at approximately 120°C/min, all in nitrogen environments.

#### 6.2.2.2 Light Microscopy

Grain size measurements were made using a grain analysis software (Stream, Olympus Corporation, Shinjuku, Japan) on images taken on a stereoscope (GX71, Olympus Corporation, Shinjuku, Japan). For imaging, the samples were mounted in 32 mm metallurgical mounts with a 2-part epoxy system, then mechanically polished with a final suspension of 0.25  $\mu\text{m}$  colloidal silica. The polished samples were then etched according to Section 6.1 Cast versus Powder **Error! Reference source not found.** .

#### 6.2.2.3 SEM

For SEM imaging, samples were mounted in 32 mm metallurgical mounts with a 2-part epoxy system, then mechanically polished with final suspension of 0.25  $\mu\text{m}$  colloidal silica. Samples were sputter-coated with a Au-Pd coating to increase conductivity.

SEM micrographs were taken in a tungsten source SEM (Zeiss EVO-MA10) at an accelerating voltage of 10 kV. Both secondary electron (SE) images and backscattered electron (BSE) images were taken, though the BSE images were used for image analysis and secondary phase quantification due to better elemental z-contrast.

### 6.2.2.3.1 Image Analysis

Image analysis software (Stream, Olympus Corporation, Shinjuku, Japan) was used to threshold the image contrast and identify the secondary phases from the matrix. Figure 13 shows images typical of this analysis; the top row shows an As-Atomized particle, the bottom row shows a thermally treated particle. The left column is the original SEM image, and the right column shows that image with applied threshold constraints, where yellow represents the  $Mg_2Si$  (dark-contrasting phase) and the blue represents the Fe-containing phases (bright-contrasting phases).

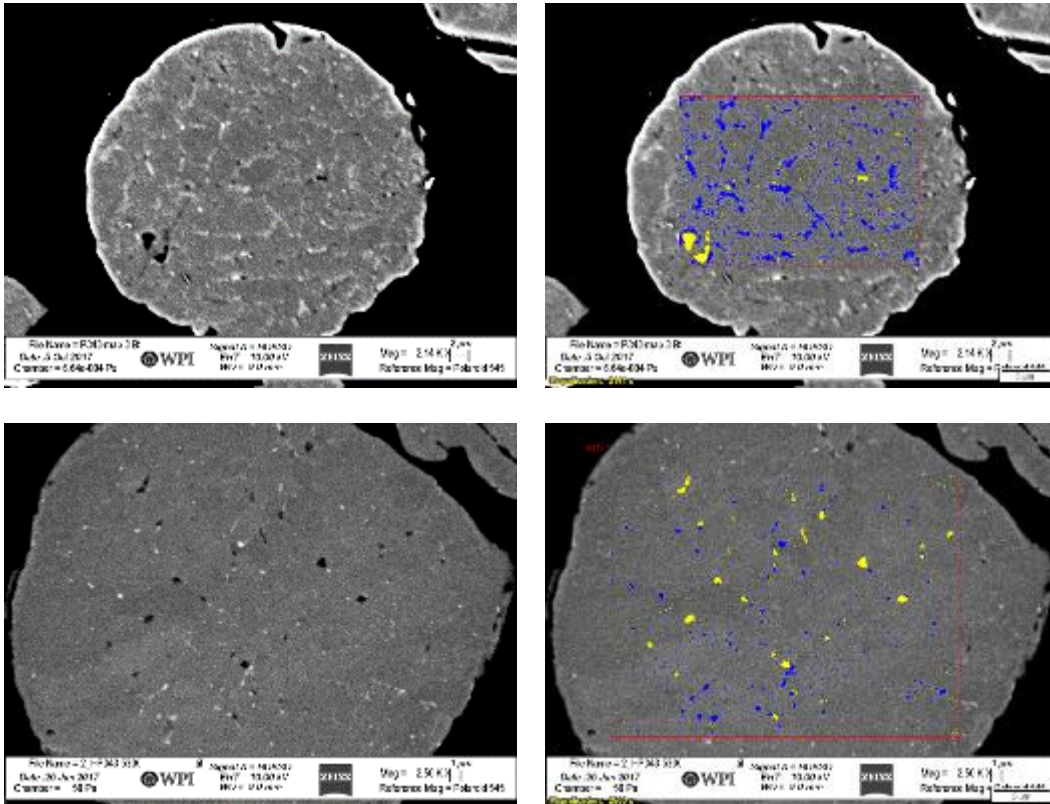


Figure 13: Typical images used for secondary phase fraction and precipitate size analysis; (a) SEM of an As-Atomized 6061 particle, (b) processed image from (a), (c) SEM of a heat treated particle, (d) processed image from (c).

Due to the limitations of interaction volume in an SEM, it is not possible to identify exactly which phases are the bright-contrasting phases using energy-dispersive x-ray spectroscopy (EDS). Additionally, these phases are so few in comparison to the matrix Al that they are not measurable using x-ray diffraction (XRD). Additional work was performed to accurately identify these secondary phases, but is discussed in Section 0

Phase Identification.

#### 6.2.2.4 EBSD

For EBSD analysis, samples were mounted in conductive carbon paint (SPI Supplies Division of Structure Probe, Inc.) on a silicon wafer, and polished in an Ar-ion cross section polisher (JEOL IB-19530CP) for 2 hours at 6 kV. The silicon wafers were then mounted on the 70° side of a pre-tilted holder for analysis.

2D EBSD was performed in a field-emission SEM (FEG-SEM, JEOL JSM-7000F) with an Oxford NordlysMax<sup>2</sup> detector. An accelerating voltage of 20 kV and step size of 0.5 μm were used.

#### 6.2.2.5 Hardness

Hardness was measured via nanoindentation (Keysight G200). For hardness analysis, the samples for SEM analysis were used and repolished with 0.25 μm silica to remove the sputtercoating. Samples were indented at room temperature using a Berkovich sharp-pyramidal diamond tip (Micro Star Tech, Inc.) and the “Express Test for Thin Films Large Table – Batch” method. This method allows for a correction factor to account for the influence of the substrate on the measured hardness value.

### 6.2.3 Results and Discussion

#### 6.2.3.1 2024

This work has been submitted in part for publication as:

**C. Walde**, K. Tsaknopoulos, V. Champagne, & D. Cote. The Microstructural Evolution of Rapidly Solidified Powder Aluminum 2024 during Thermal Processing. *Metallography, Microstructure, and Analysis*. Under Review.

##### 6.2.3.1.1 Light Microscopy

Both granular and sub-granular boundaries were revealed during etching. With etching, it is not possible to discern between the granular and sub-granular boundaries; as such, the size of the sub-granular structure – cells – were measured using light microscopy. The cell size of the As-Atomized sample ranged from 1.3-1.5 μm, and the grain size of the treated samples ranged from 1.4-2.1 μm. There was no appreciable growth as a function of solution treatment time.

##### 6.2.3.1.2 SEM

SEM micrographs were taken to evaluate the evolution of the secondary phases as a function of treatment time. Samples of micrographs used are shown in Figure 14a-h, with Figure 14e-f having a higher magnification than Figure 14a-d. Area fraction of the secondary phases were measured using image thresholding. Some precipitates were too small to be seen in the SEM; these were investigated through the use of TEM. Multiple micrographs were taken for each condition and then results were averaged. This is one advantage of SEM over TEM – the ability to quickly gather data from many powder particles, resulting in a broader understanding of the microstructure of each treatment condition. TEM results are presented and analyzed in Section 0

Phase Identification.

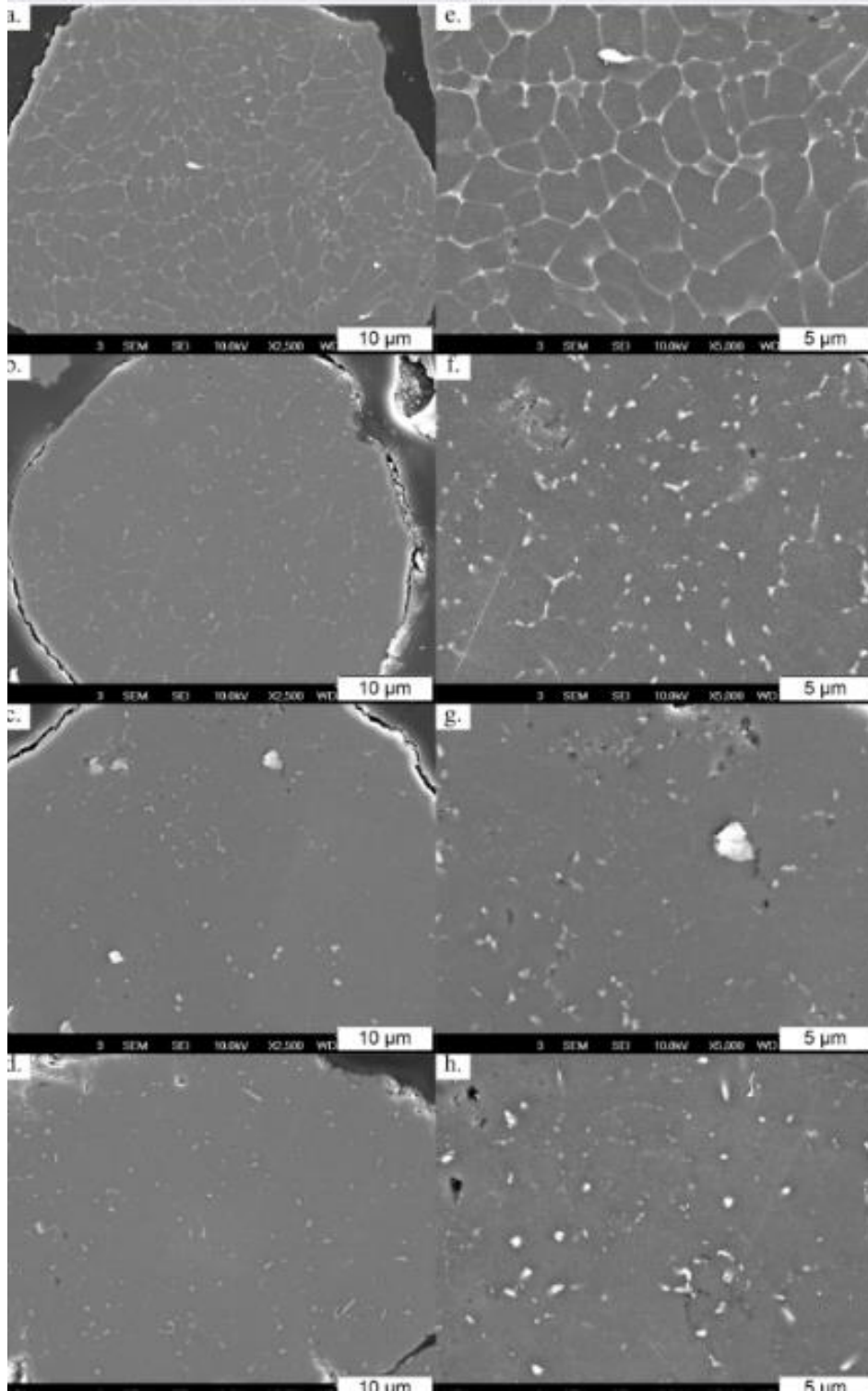


Figure 14: Low magnification SEM micrographs for 2024 powder a) as-atomized, b) 0 min treated, c) 20 min treated, and d) 120 min treated. High magnification SEM micrograph of powder e) as-atomized, f) 0 min treated, g) 20 min treated, and h) 120 min treated.

### 6.2.3.1.3 DSC

DSC was used to evaluate the relative amount of secondary phases formed upon reheating specimens that were previously solutionized for various times at 490°C (Figure 15). Note the difference between the As-Atomized (untreated) sample and the various treatments.

TEM sample preparation can be time consuming and only yields insight into a small sample of the powder, thus it is important to utilize other, faster and more representative, analysis techniques to provide insight into a larger population of powder particles.

DSC was employed to evaluate the relative amount of secondary phases formed upon reheating solutionized specimens for various times at 490 °C. Figure 15 shows these scans while Table I shows the enthalpy of the peak located around 300 °C. Note the difference in peak shape between the as-received condition and the various treatments but lack of difference in peak area as seen in the calculated enthalpies in Table 7.

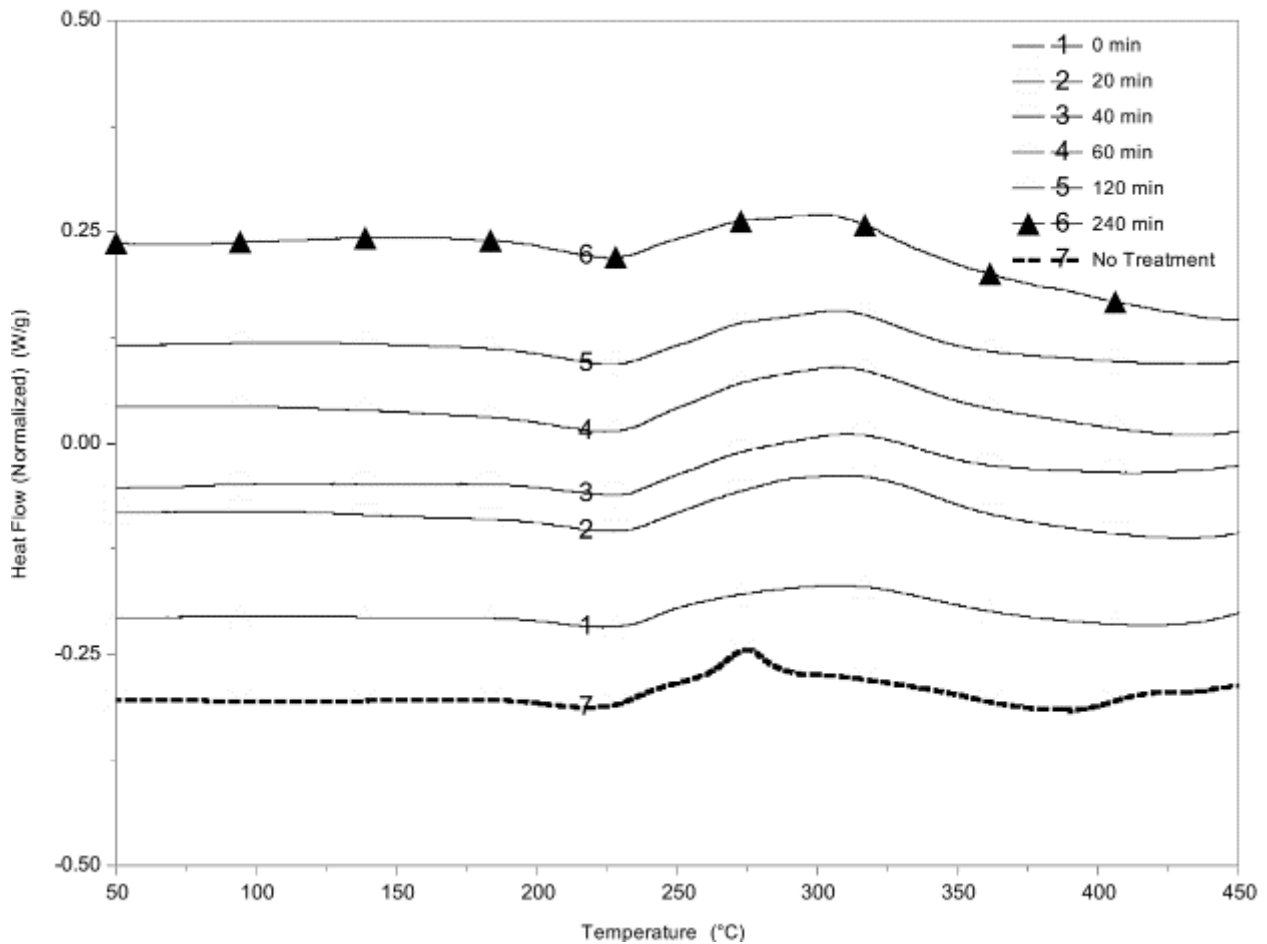


Figure 15: Normalized heat flow vs. temperature (DSC) thermograms for each condition.

Table 7: Enthalpy of peak at 300 °C for each condition.

Treatment	Enthalpy (J/g)
No Treatment	28
0 min	28
20 min	39
40 min	30
60 min	43
120 min	30
240 min	31

The difference in thermogram shape indicates a difference in precipitation kinetics; the as-received condition has distinct peaks for what have been identified as the  $\theta'$  and  $\theta$  peaks whereas the solution treated conditions have a single peak in the same temperature range.<sup>76</sup> Despite the difference in peak shape, the enthalpy associated with the reaction in each thermally treated condition is similar, implying a similar degree of solid solution in each condition. However, this contradicts what was shown in the SEM micrographs and in Figure 3, both of which indicated differences in the secondary phases, and subsequently the degree of solid solution, of each condition.

The discrepancies between the two analysis techniques – DSC and electron microscopy – limits the convenience of DSC as a faster method for evaluating various treatment conditions. While the DSC thermograms show the changes in the  $\text{Al}_2\text{Cu}$  precipitate, consistent with TEM, they do not show the other intermetallics that are also present. Other research has shown that knowing exactly which intermetallics have formed is important for predicting the mechanical behavior of the final consolidated part.<sup>71</sup>

#### 6.2.3.1.4 EBSD

EBSD was used secondarily to evaluate the granular structure of the rapidly solidified powders. A preliminary evaluation was only performed on the as-received and 60 minute thermally treated conditions. Figure 16 shows EBSD micrographs and corresponding electron backscatter micrographs of both conditions. The grain size measured via this method was found to be 3-4  $\mu\text{m}$  in both the as-received and thermally treated conditions. When the grain size from both of these EBSD micrographs are compared to the cell sizes seen in the corresponding SEM micrographs, there is a discrepancy. The sizes of the granular features measured from SEM are of comparable size to the feature size measured via light microscopy after etching, while the size of the features from EBSD are considerably larger than both of those. This implies that there are both granular and sub-granular structures in these rapidly solidified powders. This is consistent with results seen for as-received 6061 powder, showing a granular and sub-granular structure.<sup>74</sup> However, in the 6061, the authors saw a reorientation of the grains after thermal treatment for 60 minutes, which is not the case in the 2024 powder seen here. The alloying content of the studied 6061 was much lower than that of the 2024 studied here; 2 wt% in the 6061, compared to the 6 wt% in the 2024 here. Given the difference in the composition, there is a greater driving force for the precipitation of secondary phases in the 2024, leading to more phases per area. Increased amounts of phases are more effective at pinning the grain boundaries, thus delaying the reorientation in these 2024 powders.

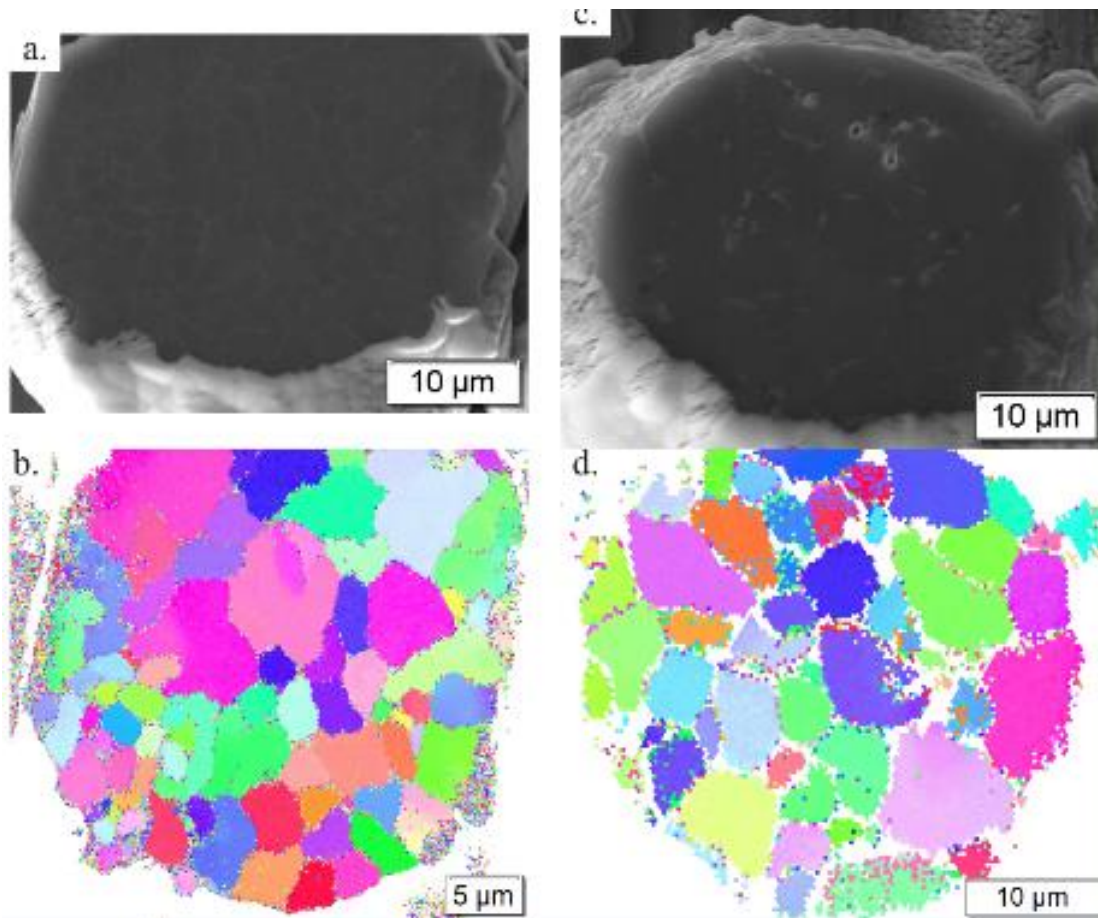


Figure 16: 2024 as-atomized powder particle a) SEM and b) EBSD. 60 minute thermally treated powder particle c) SEM and d) EBSD.

#### 6.2.3.1.5 Hardness

Figure 17 shows the results from nanohardness measurements as a function of solution treatment time at 490°C; the dashed line indicates the value of the untreated powder, for reference. To eliminate the potential effects of the mounting epoxy, results were filtered to include only data between 0.7 GPa and 3 GPa; the approximate nanohardness of the epoxy and a reasonable value for Al alloys, respectively.

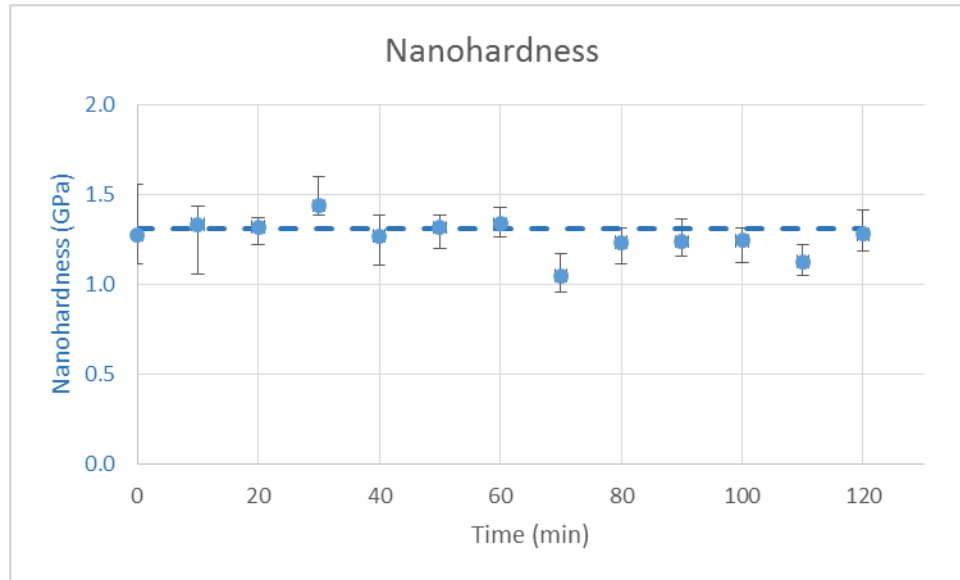


Figure 17: Nanohardness measurements of 2024 powder as a function of their treatment time

#### 6.2.3.1.6 Precipitate Size

The relative frequency of particle sizes for select solution treatments can be seen in Figure 18. The trend shows that after initial heating, the amount of the smaller particles increases, while the amount of larger particles remains relatively constant once partially dissolved. This suggests that after initial heating the larger particles either shrink or dissolve completely.

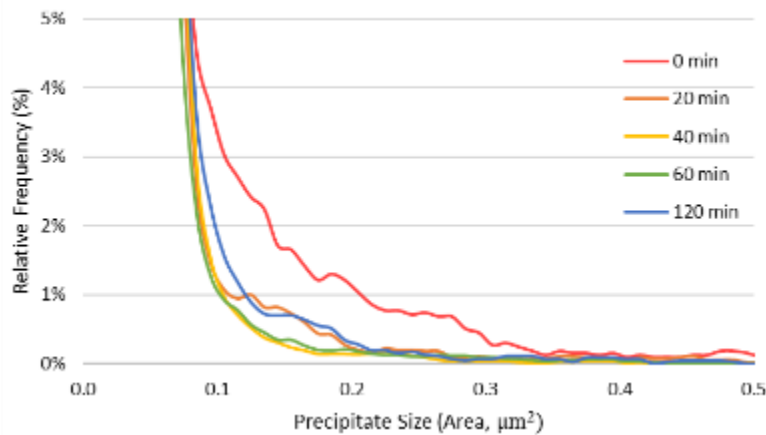


Figure 18: Relative frequency as a function of particle size, for select treatment times

Together, these trends suggest that precipitates do not completely dissolve, only partially dissolving to a minimum precipitate size. Also, that the most amount of change takes place during shorter treatment times, which coincides with the nanohardness.

The difference in peak size, shape, and location shown in the DSC scans in Figure 15 indicate a difference in the secondary phases present during each treatment time. Since the peaks indicate precipitation during the scan, it can be inferred that these phases were in solid solution after the given heat

treatment. Therefore, a larger peak indicates a better solid solution. It can be seen in Table 7 that the longer treatment times have a smaller peak in the 200°C-350°C range; there was already a larger percentage of secondary phases formed. This coincides with the trend seen in Figure 18.

#### 6.2.3.1.7 Secondary Phase Area Fraction

Nanohardness is related to strength, so both should have peaks when a maximum solid solution is achieved. This can be seen in Figure 19; there is a maximum nanohardness that coincides with a minimum secondary phase area fraction (maximum solid solution). Where the dashed orange line indicates the secondary phase area fraction of the As-Atomized (untreated) condition.

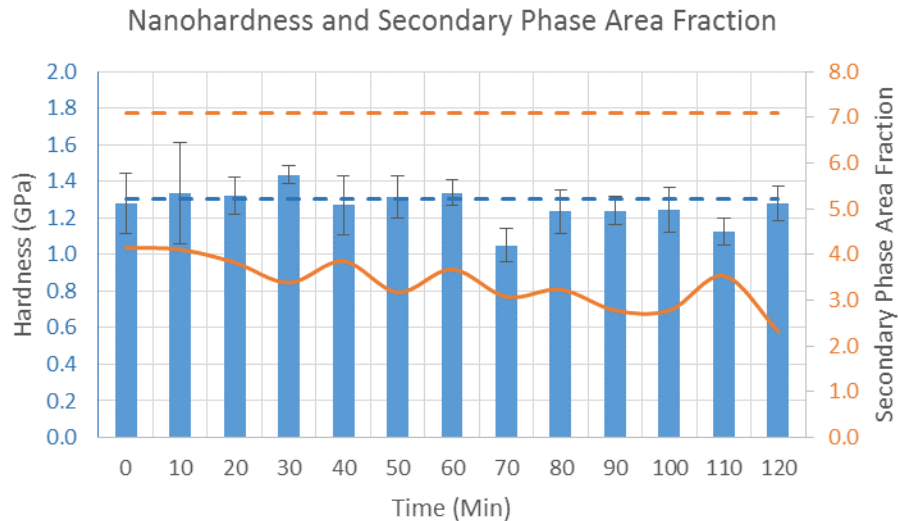


Figure 19: Nanohardness and Secondary phase area fraction as a function of treatment time

#### 6.2.3.2 6061

This work has been submitted in part for publication as:

**C. Walde**, D. Cote, V. Champagne, R. Sisson. Characterizing the Effect of Thermal Processing on Powder Al Alloys for Additive Manufacturing Applications. *Journal of Materials Engineering and Performance*. 2018. <https://doi.org/10.1007/s11665-018-3550-0>

##### 6.2.3.2.1 Light Microscopy

Both granular and sub-granular boundaries were revealed during etching. With etching, it is not possible to discern between the granular and sub-granular boundaries; as such, the size of the sub-granular structure – cells – were measured using light microscopy, and size of the grains was measured with EBSD. The cell size of the As-Atomized sample ranged from 1.4-1.9  $\mu\text{m}$ , and the grain size of the treated samples ranged from 0.8-2.5  $\mu\text{m}$ . There is no appreciable growth as a function of solution treatment time.

##### 6.2.3.2.2 SEM

SEM images were analyzed for changes in total secondary phase area fraction (SPAF) and precipitate size as a function of solution treatment time.

Figure 20 shows the relative frequency of the precipitate sizes for various solution treatment times; (a-f) are  $Mg_2Si$  (dark contrasting) while (g-l) are the Fe-containing phases (all others that contrast light with the matrix). The purpose of the solution treatment was to reduce the unwanted phase ( $Mg_2Si$ ) while minimizing growth of other phases. If the treatment was effective, the relative frequency of the larger  $Mg_2Si$  precipitates should decrease with increasing treatment time. This should occur without growing the Fe-containing phases. It can be seen that the frequency of all sizes of  $Mg_2Si$  precipitates decreases, indicating dissolution and that the frequency of all sizes of Fe-containing phases initially decreases, but increases after 240 min of treatment.

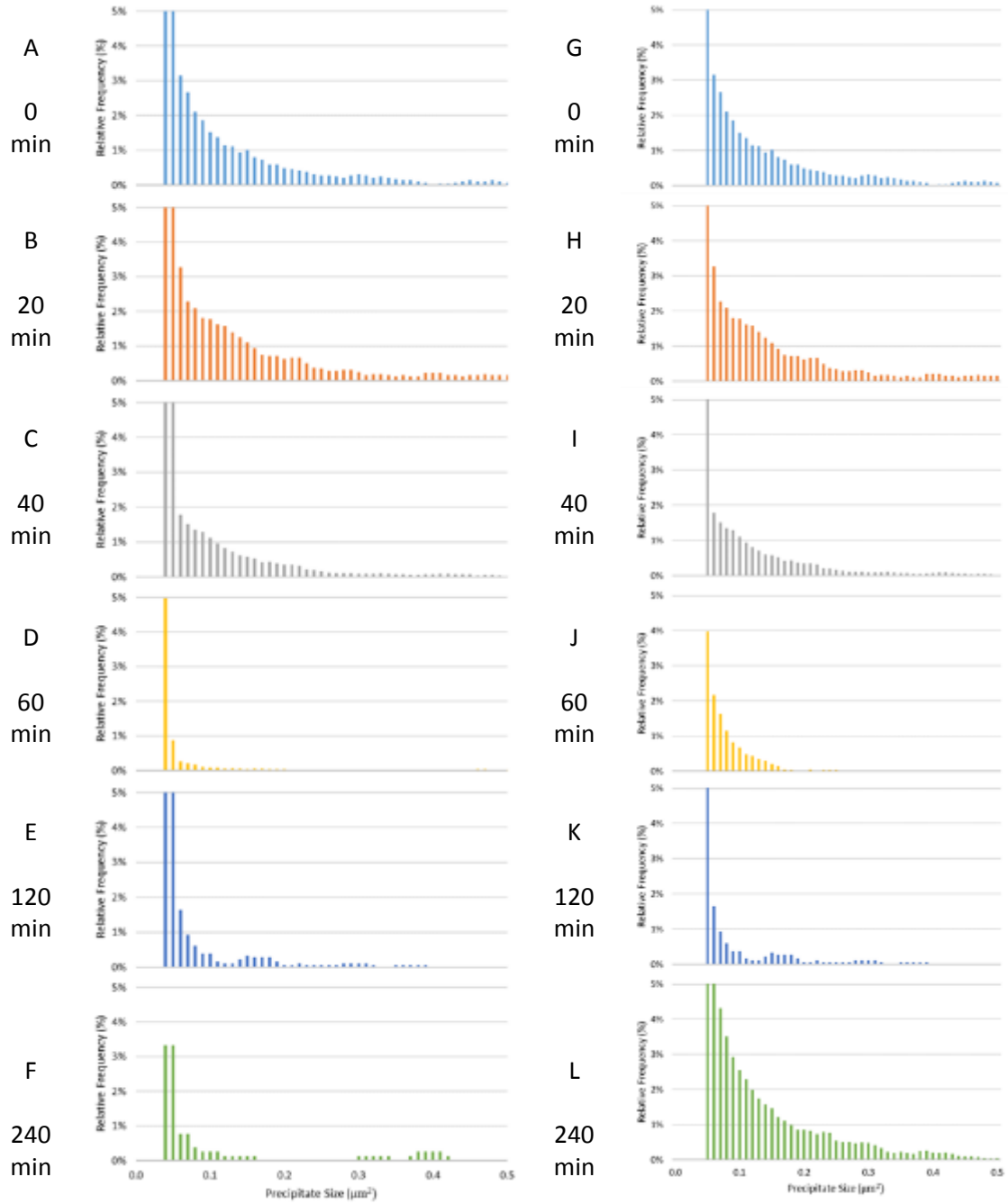


Figure 20: Relative frequency of precipitate sizes for (a) Mg<sub>2</sub>Si, 0 min, (b) Mg<sub>2</sub>Si, 20 min, (c) Mg<sub>2</sub>Si, 40 min, (d) Mg<sub>2</sub>Si, 60 min, (e) Mg<sub>2</sub>Si, 120 min, (f) Mg<sub>2</sub>Si, 240 min, (g) Fe-containing phases, 0 min, (h) Fe-containing phases, 20 min, (i) Fe-containing phases, (k) Fe-containing phases, 120 min, (l) Fe-containing phases, 240 min.

Figure 21 shows the SPAF as a function of solution treatment time. The dashed line indicates the As-Atomized condition.

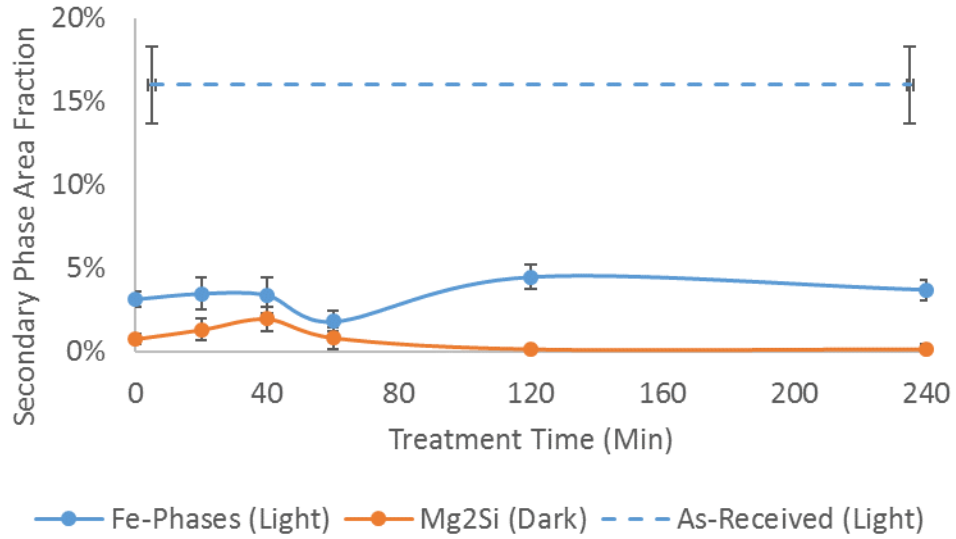
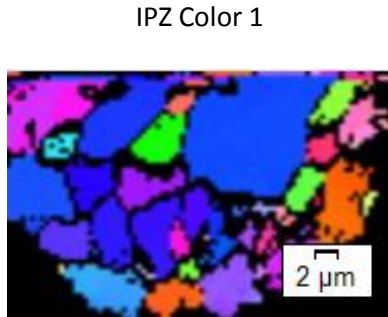


Figure 21: Secondary phase area fraction (SPAF) as a function of solution treatment time.

6.2.3.2.3 EBSD

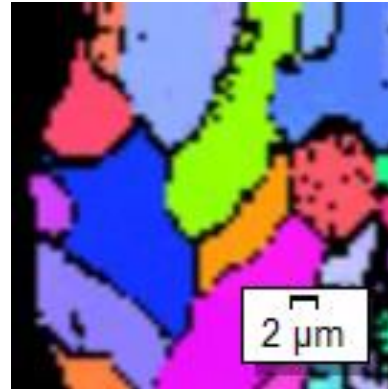
Figure 22 shows EBSD results for various solution treatment times. The measured mean grain diameter for each condition was measured as follows: 4.25  $\mu\text{m}$  (As-Atomized), 6.15  $\mu\text{m}$  (20 min), 5.99  $\mu\text{m}$  (60 min), and no measurement was possible for the 4 hour sample.

a)



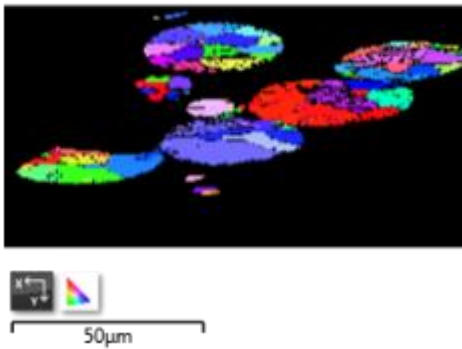
b)

IPZ Color 1



c)

IPF Z Color 1



d)

IPF Z Color 1

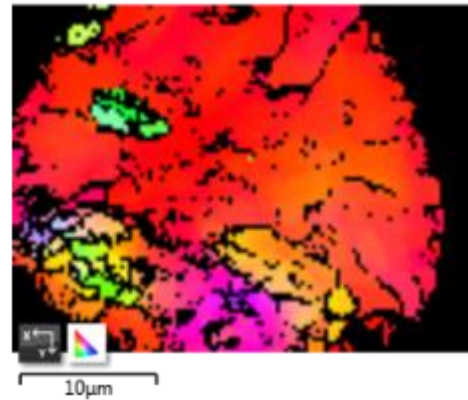


Figure 22: EBSD results for various solution treatment times. (a) As-Atomized, (b) 20 min, (c) 60 min, (d) 240 min.

#### 6.2.3.2.4 DSC

DSC was used to evaluate the relative amount of secondary phases formed upon reheating specimens that were previously solutionized for various times at 530°C (Figure 23). Note the difference between the As-Atomized (untreated) sample and the various treatments.

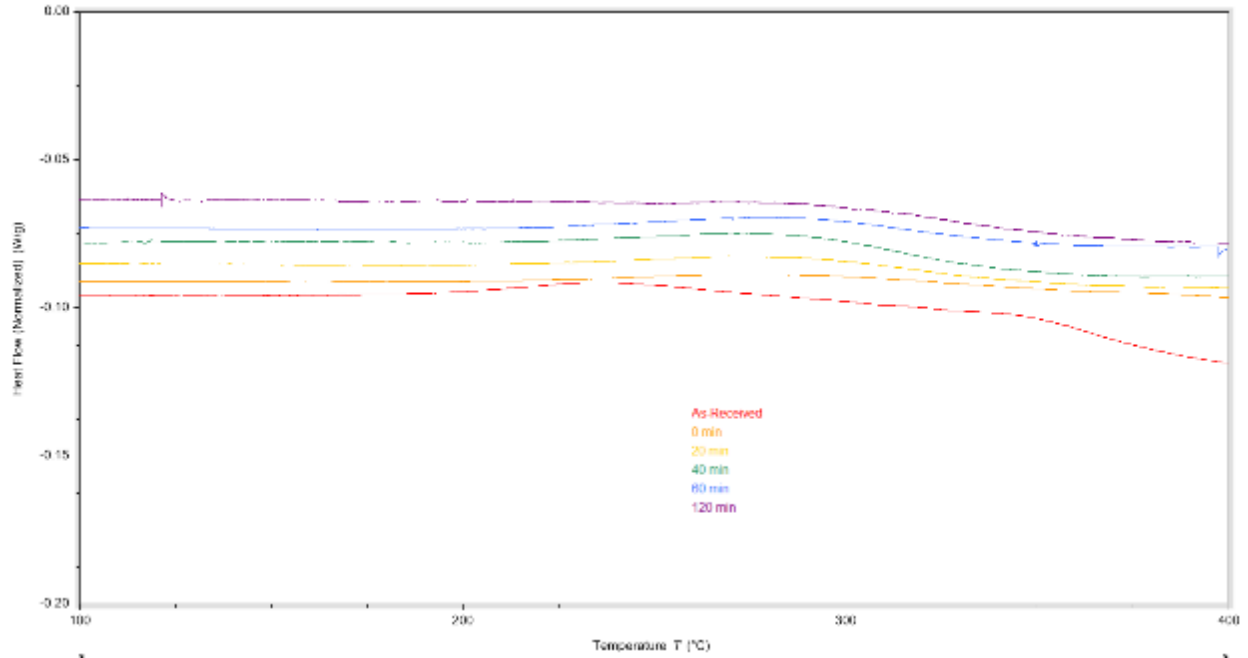


Figure 23: DSC scans of select treatment times of 6061

#### 6.2.3.2.5 Hardness

Figure 24 shows hardness as a function of solution treatment time. The results were filtered from 0.7 GPa to 3 GPa before averaging; the approximate hardness of the epoxy and a reasonable value for Al alloys, respectively.

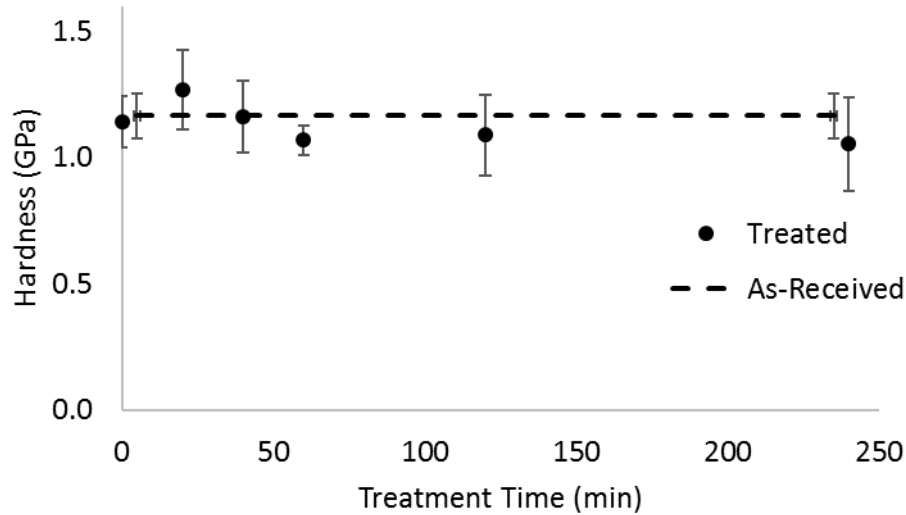


Figure 24: Hardness as a function of solution treatment time for 6061

#### 6.2.3.2.6 Precipitate Size

Figure 20 shows the relative frequency of precipitate sizes after various solution treatment times, for both  $Mg_2Si$  and Fe-containing phases. It was found that the frequency of all sizes of  $Mg_2Si$  precipitates decreases, indicating dissolution; this is consistent with what was seen in Figure 21 when analyzing the secondary phase fraction of the  $Mg_2Si$ . It was also found that the frequency of all sizes of Fe-containing phases initially decreases, but increases after 240min of treatment. Unlike the changes in the  $Mg_2Si$ , which are consistent between precipitate size and secondary phase fraction, these two quantifications for the Fe-containing phases do not agree. The SPF exhibits a phase reduction until 60 min, but at 2 hours and 4 hours, there is a phase increase. However, the precipitate size data indicates dissolution until 2 hours, and a drastic growth in all precipitate sizes after 4 hours.

This suggests that between 0-60min, there is dissolution of the Fe-containing phases that were present in the As-Atomized condition as well as nucleation and possible growth of additional phases. After 60min, the growth of those additional phases overshadows the dissolution of those initial phases.

It is proposed, based on the thermodynamic simulations presented in Figure 11, that  $Al_{45}V_7$  ( $Al_{45}Cr_7$ ),  $Al_6Mn$  ( $Al_6Fe$ ) and  $Al_{13}Fe_4$  are the phases that are dissolving and that  $Al_9Fe_2Si_2$  is growing; after 60 min, the  $Al_{45}Cr_7$ ,  $Al_6Fe$  and  $Al_{13}Fe_4$  are nearly dissolved and the  $Al_9Fe_2Si_2$  growth accelerates. This is further evaluated through the use of TEM/STEM and results are presented and analyzed in Section 0

Phase Identification. Because the goal of a solution treatment is to reduce and/or eliminate secondary phases to promote homogenous nucleation during subsequent aging, it is important to accurately know which phases are dissolving and which are growing to pick an appropriate solution treatment time.

#### 6.2.3.2.7 Secondary Phase Fraction

In comparing Figure 21 and Figure 24, it can be seen that the hardness follows the trend seen in the change in the area fraction of the Fe-containing phases. This supports what was seen in Figure 20– that there are multiple Fe-containing phases that have competing effects, which is to be expected based on the Thermo-Calc diagram.

#### 6.2.3.3 7075

This work has been submitted in part for publication as:

**C. Walde**, K. Tsaknopoulos, V. Champagne, & D. Cote. Phase Transformations in Thermally Treated Gas-Atomized Al 7075 Powder. *Metallurgical and Materials Transactions A*. Under Review.

#### 6.2.3.3.1 Light Microscopy

Both granular and sub-granular boundaries were revealed during etching. With etching, it is not possible to discern between the granular and sub-granular boundaries; as such, the size of the sub-granular structure – cells – were measured using light microscopy. The cell size of the As-Atomized sample ranged from 1.0-1.3  $\mu\text{m}$ , and the grain size of the treated samples ranged from 1.7-2.3  $\mu\text{m}$ . After an initial increase in grain size, there was no appreciable growth as a function of solution treatment time.

#### 6.2.3.3.2 SEM

SEM images were analyzed for changes in total secondary phase area fraction (SPAF) and precipitate size as a function of solution treatment time.

Figure 25: Overview SEM micrograph and EBSD micrograph of the as-atomized condition for 7075. Figure 25 displays an overview SEM micrograph and EBSD micrograph of the as-atomized condition. The continuous network structure present at both the grain and sub-grain boundaries in the as-atomized is consistent with what is seen in other gas-atomized powders (2024 and 6061). Note the large grains in Figure 25b that have smaller regions with slight misorientation ( $<15^\circ$ ) within them, which corresponds to the sub-grain boundaries.

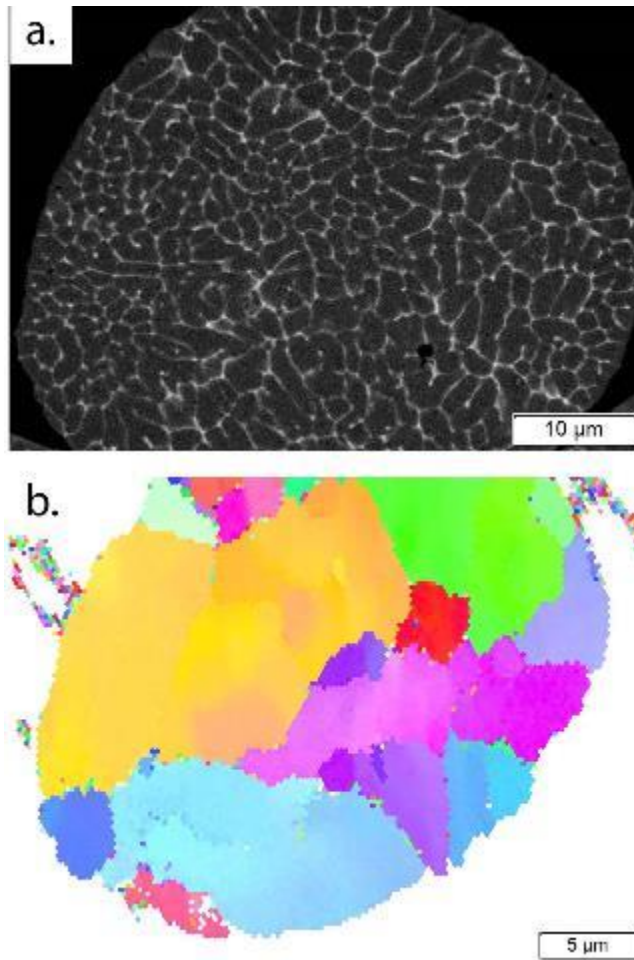


Figure 25: Overview SEM micrograph and EBSD micrograph of the as-atomized condition for 7075.

Figure 26 shows overview SEM micrographs of the thermally treated conditions. As seen in Figure 26a and Figure 26b, the network structure present in the as-atomized condition begins to dissolve simply by bringing the powder up to an elevated temperature. With increased treatment times, note the presence of both larger phases and smaller phases in two different regions; the large phases are present at the high-angle grain boundaries, such as seen in Figure 25b, while the smaller phases are present at the low-angle sub-grain boundaries.

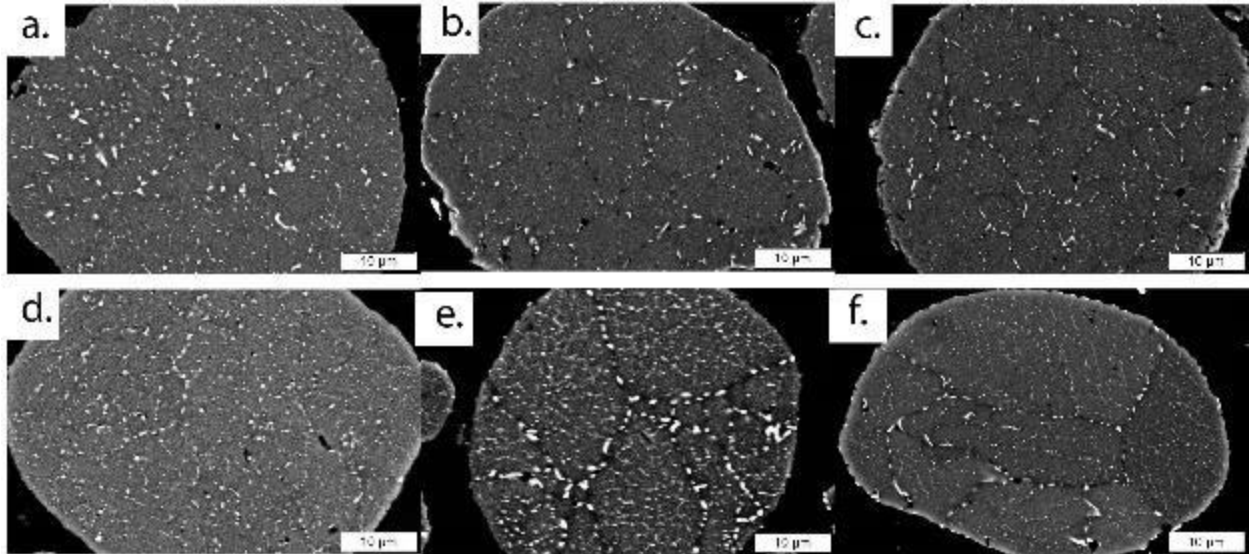


Figure 26: Overview SEM micrographs of the thermally treated conditions of 7075; a) 465 °C for 0min, b) 465 °C for 60min, c) 465 °C for 120min, d) 480 °C for 0min, e) 480 °C for 60min, f) 480 °C for 120min.

Figure 27 shows the area percent of secondary phases present as a function of treatment time for both treatment temperatures.

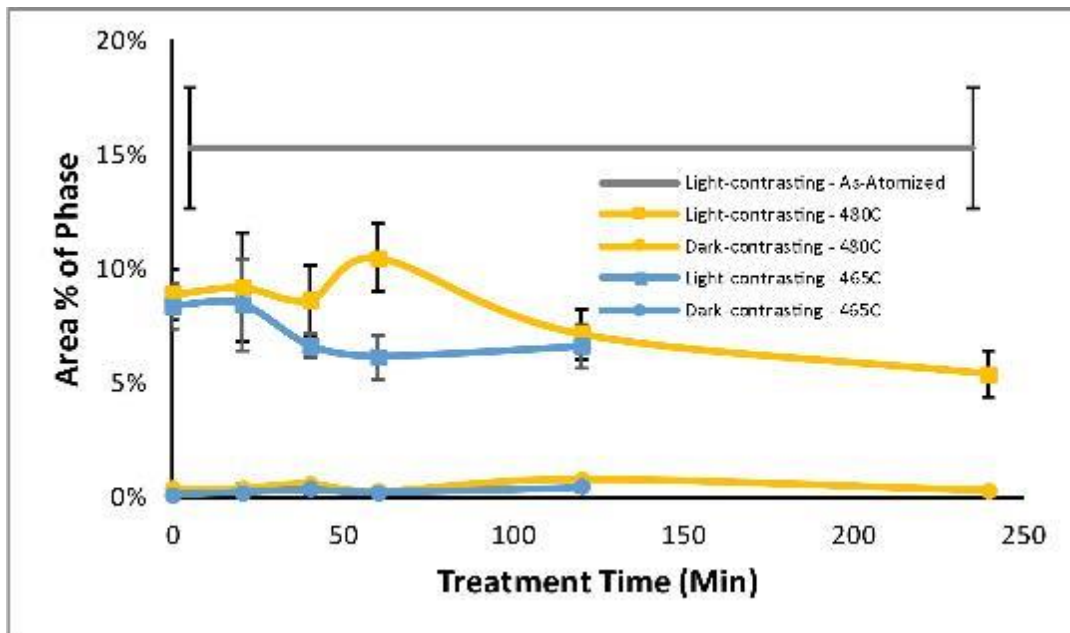


Figure 27: Area percent of secondary phases present in 7075 as a function of treatment time for both treatment temperatures.

In the treatment performed at 465 °C, there is an initial drop in secondary phase amount after the sample reaches the set temperature, consistent with Figure 26. Then, there is a slight decrease in amount of bright-contrasting secondary phases after 20 minutes of treatment, stabilizing after 60

minutes of treatment. The dark-contrasting phases, while not detected in the as-atomized condition, is stable in very low amounts across all treatment temperatures.

In the treatment performed at 480 °C, there is an initial drop in secondary phases after increasing the sample to the set temperature, consistent with Figure 26d, after which there is a slight increase in the bright-contrasting phases until 60 minutes of treatment. After 60 minutes, the bright-contrasting phases decrease. The dark-contrasting phase, while not detected in the as-atomized condition, is stable across all treatment temperatures.

When comparing the two treatment temperatures, it is of note that the dark-contrasting phase area percent is the same, whereas the bright-contrasting phase trends vary. There is a similar reduction in the bright-contrasting phase in both treatments when at the set temperature. However, after approximately 20 minutes of treatment, the trends diverge; at 480 °C, the bright-contrasting phase increases while at 465 °C the bright-contrasting phase decreases. After approximately 120 minutes of treatment, the trends converge again, appearing to reach an equilibrium.

Due to the large interaction volume in the SEM, EDS was not successful in further differentiating the light- and dark-contrasting phases into the constituents predicted in Thermo-Calc. Hence, EDS was performed in a TEM for phase ID. This is presented in Section 6.3

## Phase Identification.

### 6.2.3.3.3 DSC

DSC was used to evaluate the relative amount of secondary phases formed upon reheating specimens that were previously solutionized for various times at 465°C (Figure 28). Note the difference between the As-Atomized (untreated) sample and the various treatments.

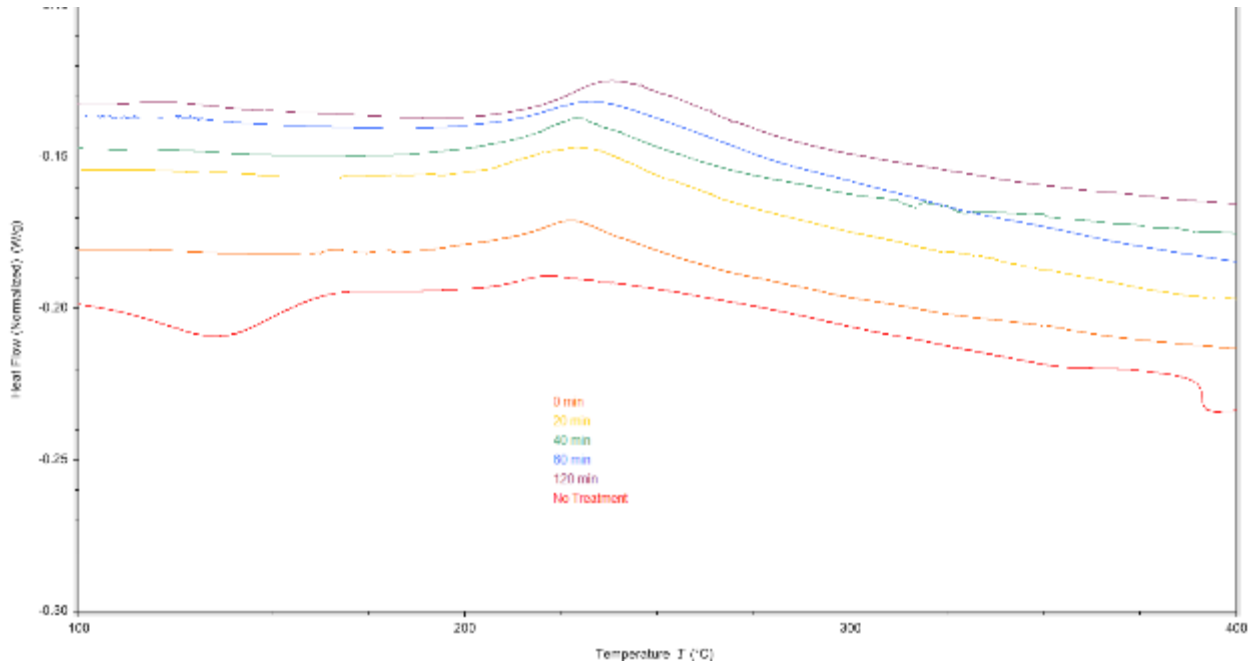


Figure 28: DSC scans of select treatment times of 7075

### 6.2.3.3.4 Hardness

Figure 29 shows hardness as a function of solution treatment time for the treatments performed at 465 °C. The results were filtered from 0.7 GPa to 3 GPa before averaging; the approximate hardness of the epoxy and a reasonable value for Al alloys, respectively.

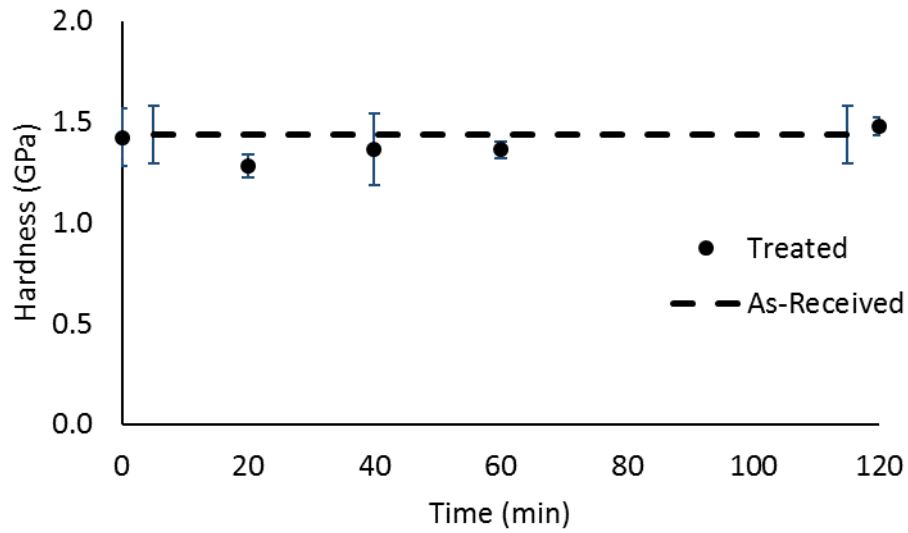


Figure 29: Hardness as a function of solution treatment time for 7075

#### 6.2.3.3.5 Secondary Phase Fraction

In comparing Figure 27 and Figure 29, it can be seen that the hardness follows the trend seen in the change in the area fraction of the Fe-containing phases. This supports what was seen in Figure 27 – that there are multiple Fe-containing phases that have competing effects, which is to be expected based on the Thermo-Calc diagram. The Fe-containing phases will be more specifically identified in Section 0

Phase Identification.

## 6.2.4 Conclusions

### 6.2.4.1 2024

From the SEM micrographs, it is clear that chemical segregation that is present in the as-atomized (untreated) powder is homogenized in as little as 10 minutes of treatment at temperature, which agrees with the previous work on diffusion of chemical segregation. Additionally, EBSD revealed the existence of sub-grains within the powder particle grains. With thermal treatments of 1 hour, the 2024 grain orientations did not change.

One limitation of this work is that the secondary phases are all categorized together. This was done because it was not possible to accurately identify the phases through the use of EDS in an SEM; these phases are too small compared to the interaction volume of the beam. Another limitation of this work is that the contributions of secondary phases smaller than  $0.1 \mu\text{m}^2$  were ignored, as they could not be resolved in the SEM. Both of these limitations will be addressed through the use of TEM and STEM in Section 0

Phase Identification, since there is a higher resolution and smaller interaction volume.

#### *6.2.4.2 6061*

From the SEM micrographs, it is clear that the solution treatments were effective in reducing the amount of secondary phases. Additionally, the SEM combined with EBSD revealed the existence of sub-grains within powder particle grains.

This understanding of the microstructure, transformations, and properties of gas atomized powder can serve as a reference when considering process parameters for treatment of feedstock powder for solid state consolidation processes.

Again, a limitation of this work is that the Fe-containing phases were all grouped together; further work will be done in TEM to identify which Fe phases are present.

#### *6.2.4.3 7075*

From the SEM micrographs, it can be seen that the chemical segregation present in the as-atomized powder is homogenized in as little as 20 minutes of treatment at either treatment temperature. It was also seen that there are likely competing effects from different Fe-containing precipitates; this will be addressed in future work with TEM/STEM to perform phase identification.

Additionally, EBSD revealed the presence of grains and sub-grains in the powders, confirming what was seen in other alloys.

## 6.3 Phase Identification

### 6.3.1 Materials

The powder used for this study was the Al 2024, 6061, and 7075 that was used in Section 6.1 Cast versus Powder; see Section 6.1 Cast versus Powder for material details.

### 6.3.2 Method

#### 6.3.2.1 *Treatment Parameters*

The same treatment temperatures as determined for each alloy for analysis in the SEM were also evaluated in the TEM (Section 0

Phase Identification). Based on the secondary phase area fraction curves presented in Figure 19, Figure 21, and Figure 27, treatment times of 1 hour, as well as the as-atomized condition, were chosen for TEM evaluation.

#### 6.3.2.2 FIB

For TEM imaging, samples were created using a gallium focused ion beam (FIB) (FEI Helios 660 Nanolab and FEI Scios Dual Beam FIBs). Powder was distributed on carbon tape on an SEM stub for FIB sectioning. This was done by applying a protective Pt layer on the top surface of the chosen powder particle (approximately  $40\ \mu\text{m} \times 1\ \mu\text{m} \times 1\ \mu\text{m}$ ). Material on either side of the Pt layer was then removed by milling perpendicular to the top surface of the Pt layer. This produced a parallel-sided slice of the powder particle. This slice was then lifted out and attached to a Mo omni-grid. Then it was thinned to a thickness of approximately 100 nm with a final finish of 5 kV to remove surface stresses. For elemental quantification analysis using EDS, thinner samples were needed to remove the interaction signal from other phases and the matrix behind the desired phase; smaller sections of the large sample were taken for further thinning for this analysis.

#### 6.3.2.3 TEM

TEM and STEM images were taken using a Probe-corrected FEI Titan Themis 300 S/TEM with ChemiSTEM technology at an accelerating voltage of 300 kV. EDS was completed using a Super-X EDS system at 300 kV.

##### 6.3.2.3.1 Image Analysis

Image analysis was performed on the TEM micrographs the same way it was performed on the SEM micrographs in Section 0

Solution Treatment.

### 6.3.3 Results and Discussion

#### 6.3.3.1 2024

This work has been submitted in part for publication as:

**C. Walde**, K. Tsaknopoulos, V. Champagne, & D. Cote. The Microstructural Evolution of Rapidly Solidified Powder Aluminum 2024 during Thermal Processing. *Metallography, Microstructure, and Analysis*. Under Review.

TEM was used to evaluate the internal microstructure of the powder. Figure 30 shows low magnification micrographs of the lamella from a powder particle for a) as-received and b) thermally treated for 1 hour at 490 °C. It shows similar features as those seen in the SEM micrographs (Figure 14), however, finer precipitates in the thermally treated sample are now resolvable. Image thresholding was also performed on these micrographs, and the results are tabulated in Table 8. Note the agreement between the values calculated by the different electron microscopy techniques when Table 8 is compared to Figure 19.

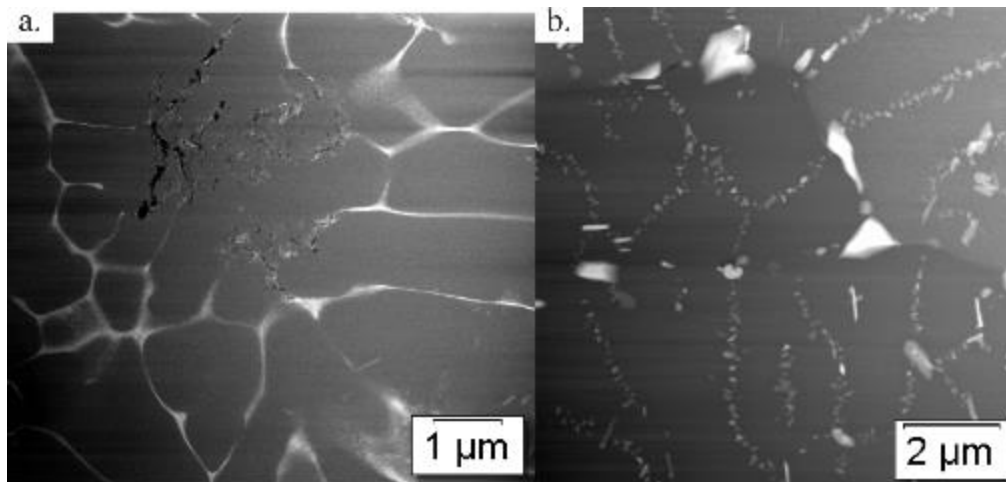


Figure 30: Low magnification HAADF micrographs of powder Al 2024 a) in the as-atomized condition and b) after a 60 minute thermal treatment.

Table 8: Secondary phase area (%) for 2024, as measured via TEM.

	As-Atomized	Thermally Treated
Al <sub>2</sub> Cu	4.2 %	4.1 %
S-Phase	9.2 %	0.0 %
Al <sub>6</sub> Mn	0.0 %	3.4 %

Figure 31 shows high magnification representative microstructures of the as-received condition with elemental EDS maps. In the SEM micrographs, the secondary phases at the boundaries appear to be a single continuous phase, however, in the HAADF images in Figure 6, it can be seen that two phases exist at the boundary. The elemental maps in Figure 6 show that one phase consists of Cu, Mg, and Si, and the

second, a discrete phase, consists of Cu, Fe, and Mn. Further investigation using EDS point quantification analysis revealed these phases to be S-phase with trace amounts of Si and Al<sub>2</sub>Cu with trace amounts of Fe and Mn, respectively. During rapid solidification there is solute microsegregation of the alloying elements at the boundaries. This segregation is highly unstable with a high propensity for the formation of secondary phases. Thus, the S-phase and Al<sub>2</sub>Cu form rapidly while the Fe and Mn have no time to diffuse. Based on literature data compiled in the Thermo-Calc databases, it is known that Fe and Mn are soluble in Al<sub>2</sub>Cu.

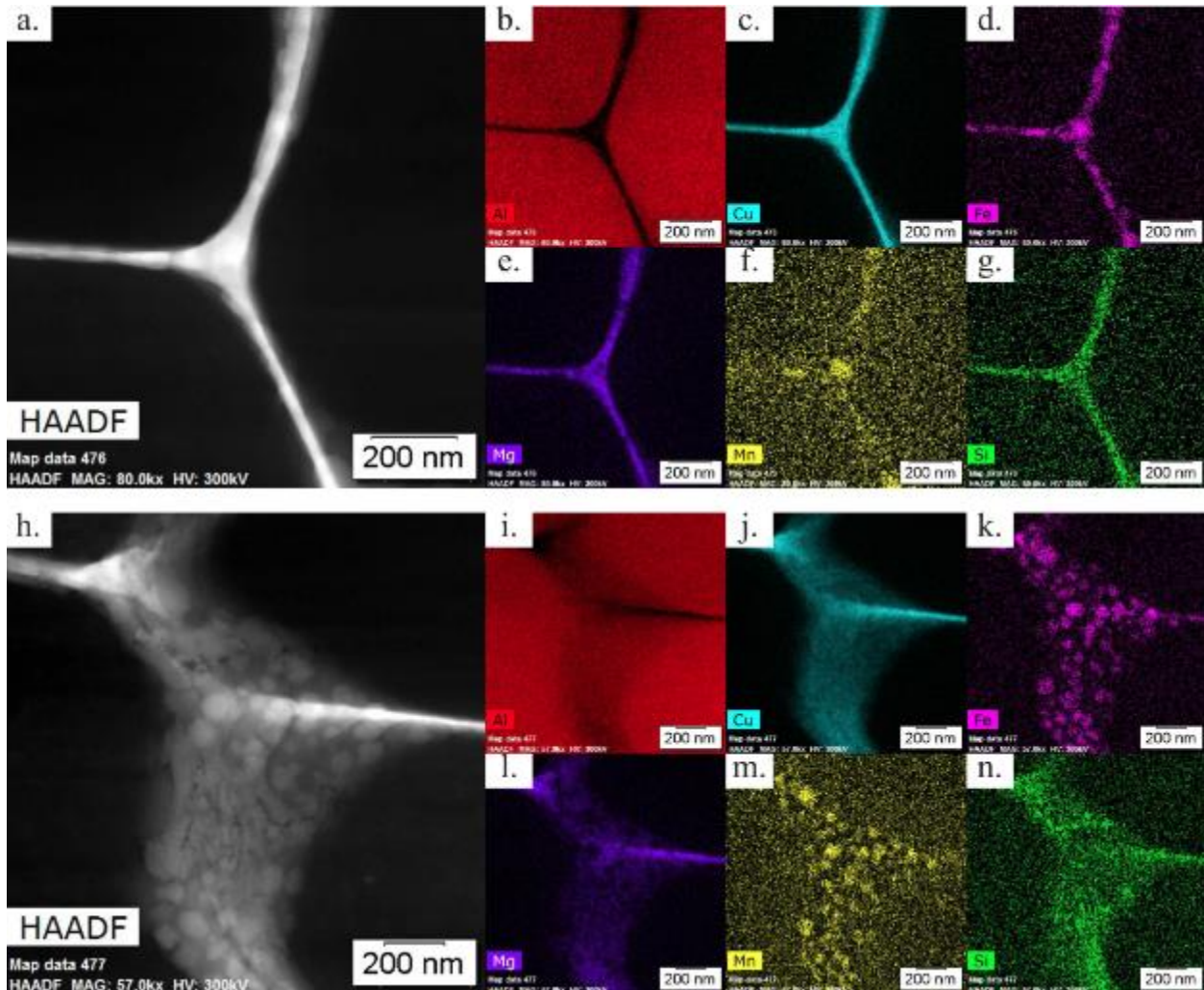


Figure 31: High magnification HAADF's and elemental EDS maps for the as-atomized condition of 2024 at a triple point a) HAADF, b) Al, c) Cu, d) Fe, e) Mg, f) Mn, and g) Si, and at a boundary h) HAADF, i) Al, j) Cu, k) Fe, l) Mg, m) Mn, and n) Si.

The two phases have an intertwined morphology. S-phase forms a network-structure at the sub-grain boundaries, while Al<sub>2</sub>Cu forms as discs in or on the network. Little to no precipitation is seen in the bulk of the sub-grains, though considering the small size of the sub-grains and subsequent short diffusion distance to a boundary, this is an expected observation.

Given the rapidly solidified nature of the powders and the non-equilibrium conditions, it is expected that the as-received microstructure would follow Scheil solidification. Based on the Scheil solidification model in Thermo-Calc (Figure 10b), the two most abundant phases predicted are S-phase and  $\text{Al}_2\text{Cu}$ . As this is consistent with the results from the experimental, it validates the applicability of the Scheil solidification model this rapidly solidified powder.

Figure 32 shows high magnification of representative microstructures of the 60 minute thermally treated condition with elemental EDS maps. In SEM micrographs in Figure 14, both large and small discrete secondary phases can be seen at the boundaries. This is similar to what is seen in the TEM in the HAADF images in Figure 32, however in the TEM it is possible to resolve even smaller phases. Based on the size distributions of these phases, it is hypothesized that there are two different phases. The elemental maps in Figure 32 show that two phases do exist, one consisting of Al and Cu, and the other consisting of Al, Cu, Fe, and Mn. Further investigation using EDS point quantification analysis revealed these phases to be  $\text{Al}_2\text{Cu}$  and  $\text{Al}_6\text{Mn}$  with trace amounts of Cu and Fe; additionally, small amounts of  $\text{Al}_{28}\text{Cu}_4\text{Mn}_7$  were identified. The  $\text{Al}_2\text{Cu}$  has a plate-like morphology, the  $\text{Al}_6\text{Mn}$  a short rod morphology, and the  $\text{Al}_{28}\text{Cu}_4\text{Mn}_7$  a small plate morphology. While  $\text{Al}_2\text{Cu}$  is present in both the as-received and thermally treated conditions, there are differences in both the composition and morphology.

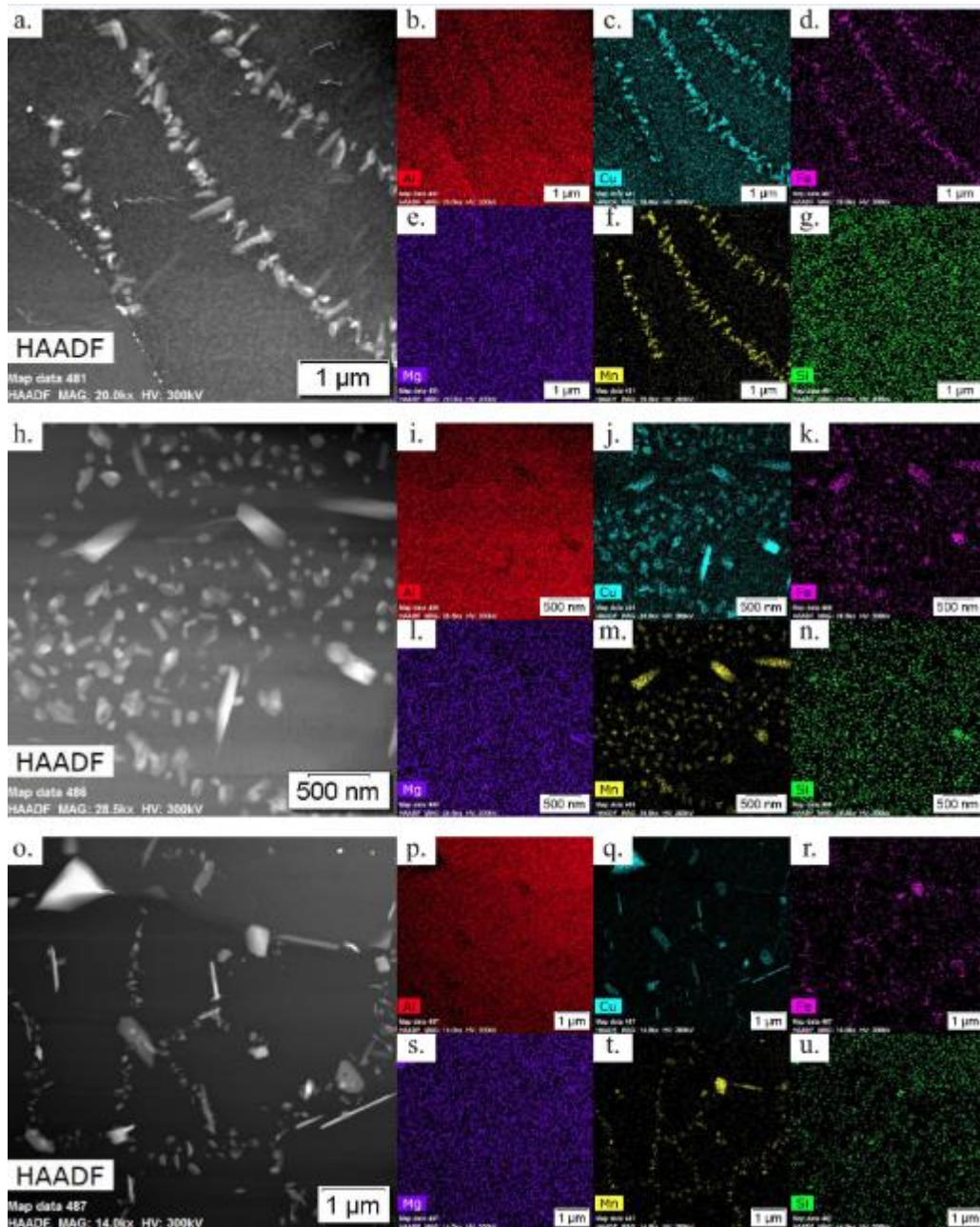


Figure 32: High magnification HAADF's and elemental EDS maps for the 60 minute thermally treated condition of 2024 at a multiple boundaries region 1 a) HAADF, b) Al, c) Cu, d) Fe, e) Mg, f) Mn, and g) Si, at region 2 h) HAADF, i) Al, j) Cu, k) Fe, l) Mg, m) Mn, a

As seen in Figure 10a, S-phase has a dissolution temperature above the treatment temperature, as does  $Al_2Cu$ ; this does not agree with what was seen experimentally. Additionally, Figure 10a predicts the presence of the  $Al_{15}Si_2Mn_4$  phase, which again is in disagreement with the experimental results. To further understand the phase transformation in this system, the model was calibrated to the experimental results by suppressing the  $Al_{15}Si_2Mn_4$  phase in the simulation. The resultant equilibrium diagram is shown in Figure 33a. Figure 33b shows an increased magnification of Figure 33a and Figure

33c shows an increased magnification of the original diagram (Figure 10a) for comparison. Figure 33b shows that when  $Al_{15}Si_2Mn_4$  is not present, a change in the stability of the other phases occurs; S-phase will completely dissolve at 490 °C,  $Al_2Cu$  remains stable until 502 °C, and  $Al_{28}Cu_4Mn_7$  will now begin to form at 480 °C. Given these changes, the model now predicts the phases present in the powder. During thermal treatment, the boundary network S-phase dissolves, leaving a concentration of Al, Cu, Mg, and Si at the boundaries. Additionally, the Fe and Mn that was dissolved in the  $Al_2Cu$  in the as-received condition diffuses out of the  $Al_2Cu$  into the matrix, adds additional Fe and Mn concentrations at the boundary. This high concentration of Al, Cu, Fe, and Mn leads to the formation of  $Al_6Mn$ , as this is the next thermodynamically stable phase. The added thermal energy enables the growth of  $Al_2Cu$  from 50-100 nm-sized discs to 400-800 nm-sized plates.

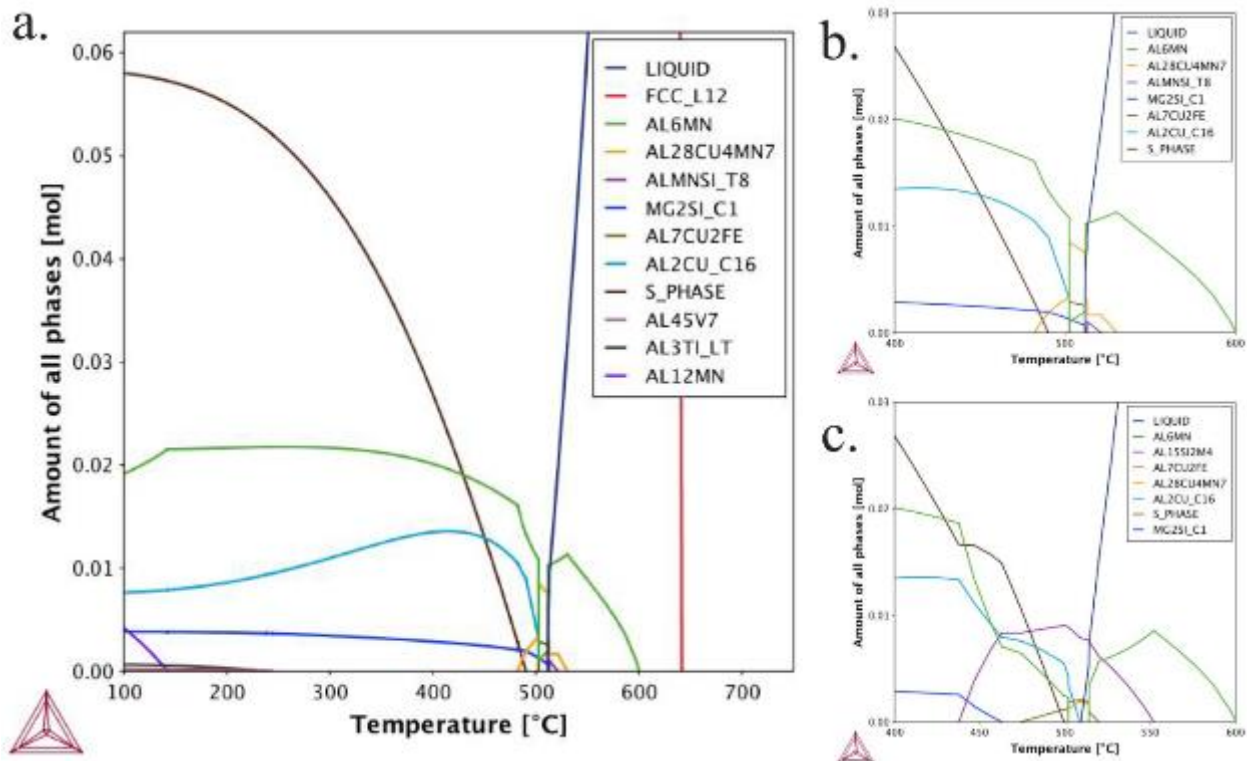


Figure 33: Phase diagrams predicted using Thermo-Calc a) with  $Al_{15}Si_2Mn_4$  suppressed, b) increased magnification of (a), and c) increased magnification of Figure 1a.

### 6.3.3.2 6061

This work has been submitted in part for publication as:

**C. Walde**, K. Tsaknopoulos, V. Champagne, & D. Cote. Evolution of Fe-rich Phases in thermally processed aluminum 6061 powders for AM applications. *Journal of Thermal Spray Technology*. Under Review.

K. Tsaknopoulos, **C. Walde**, V. Champagne, & D. Cote. Gas-Atomized Al 6061 Powder: Phase Identification and Evolution During Thermal Treatment. *JOM*. 2018. <https://doi.org/10.1007/s11837-018-3175-7>

Typical images of this analysis can be seen in Figure 34, which shows typical TEM images for both the as-manufactured and thermally treated samples. The Mg-rich phases contrast darker than the matrix in the TEM high-angle annular dark-field (HAADF) images while the Fe-rich phases are contrast lighter.

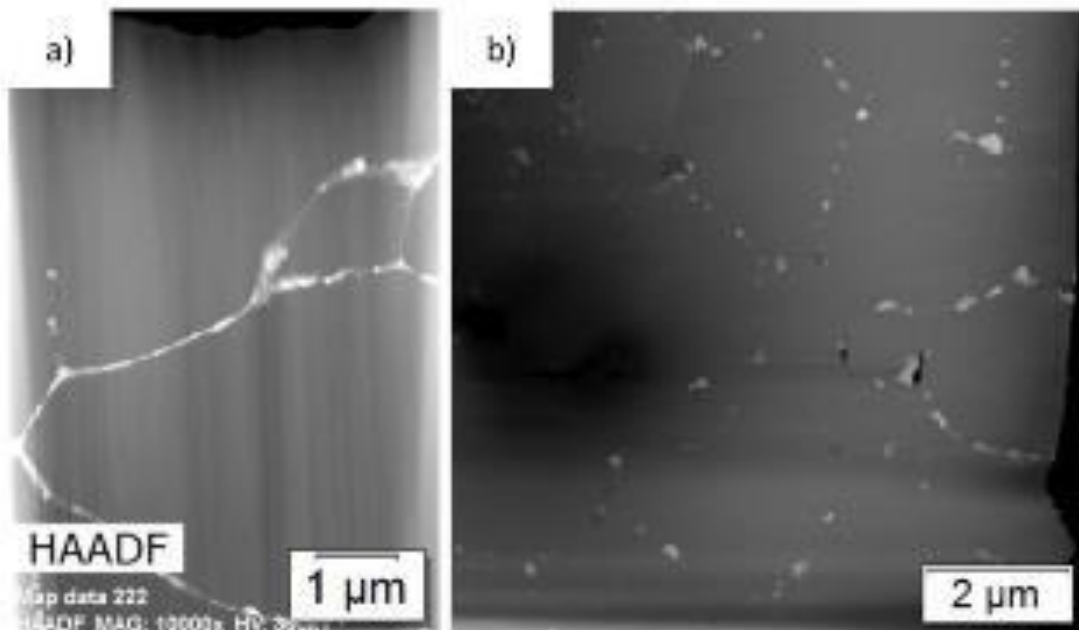


Figure 34: Typical images used for secondary phase fraction analysis: (a) TEM-HAADF of as-manufactured Al 6061 particle lamella, (b) TEM HAADF of thermally treated Al 6061 particle lamella.

#### 6.3.3.2.1 Modeling

The diagrams created in Thermo-Calc provide insight into which phases are expected given the alloy composition and serve as a starting point for phase identification in the powder microstructure. Figure 35a shows the equilibrium phases present in the Al 6061 composition as a function of temperature. This shows the stability of the different secondary phases, which is especially useful to know during thermal treatment. Since these powders are gas atomized, they are rapidly solidified and are thus not considered to be in an equilibrium state. Given that, it is expected that the phases present in the as-manufactured powder microstructure would more closely match that predicted by the Scheil solidification diagram, Figure 35b.

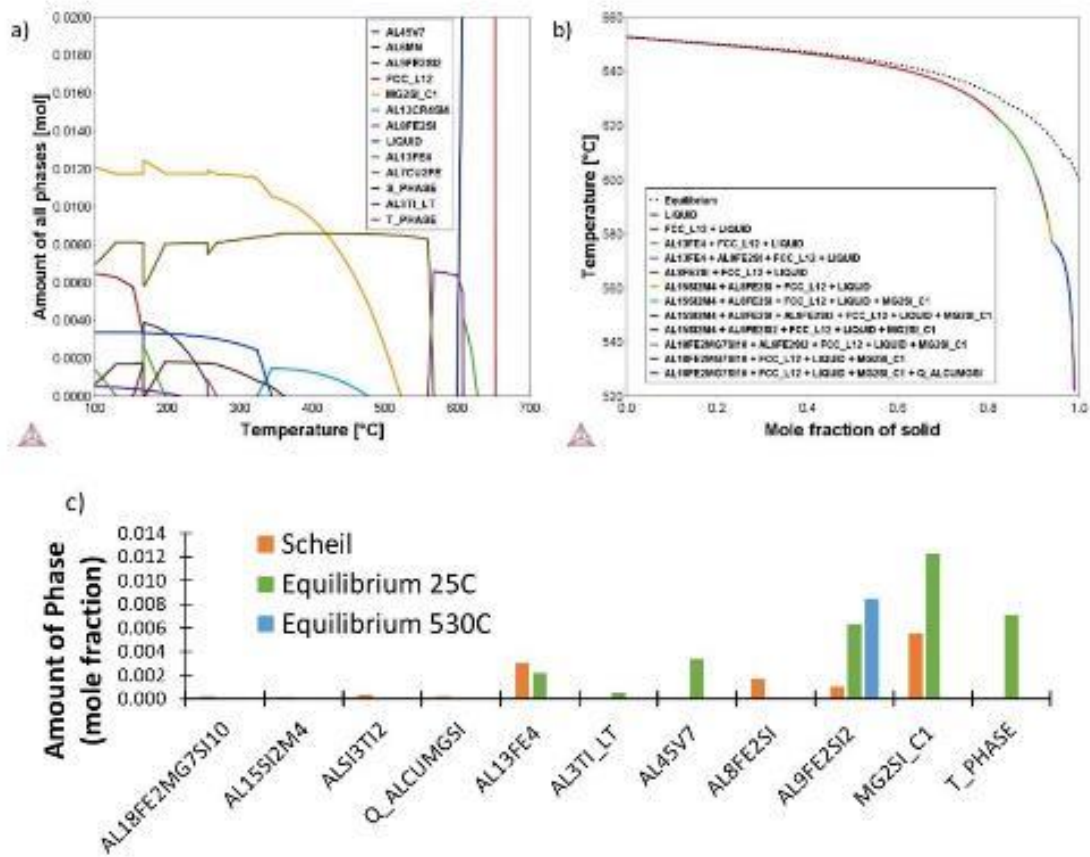


Figure 35: (a) Equilibrium diagram from Thermo-Calc software, (b) Scheil diagram from Thermo-Calc software, (c) amount of each possible phase as predicted by Thermo-Calc software at varying conditions.

The equilibrium and non-equilibrium phases predicted by the Thermo-Calc models for as-manufactured and thermally treated conditions are compiled in Figure 35c. This demonstrates the predicted phases in the as-manufactured powder for rapid solidification (Scheil results), the phases expected if the initial powder were at equilibrium (Equilibrium results at 25°C), and the phases expected after thermal treatment of the powder (Equilibrium results at 530°C). The Scheil results predict the presence of  $\text{Al}_{15}\text{Si}_2(\text{Fe,Mn})_4$ ,  $\text{Q}(\text{AlCuMgSi})$ ,  $\text{Al}_{18}\text{Fe}_2\text{Mg}_7\text{Si}_{10}$ ,  $\text{AlSi}_3\text{Ti}_2$ ,  $\text{Al}_9\text{Fe}_2\text{Si}_2$ ,  $\text{Al}_8\text{Fe}_2\text{Si}$ ,  $\text{Al}_{13}\text{Fe}_4$  and  $\text{Mg}_2\text{Si}$ , in order of increasing abundance in the as-manufactured powder microstructure, with the most prominent phases being  $\text{Mg}_2\text{Si}$  and  $\text{Al}_{13}\text{Fe}_4$ . The Equilibrium results at 25°C predict the presence of  $\text{Al}_3\text{Ti}$ ,  $\text{Al}_{13}\text{Fe}_4$ ,  $\text{Al}_{45}\text{Cr}_7$ ,  $\text{Al}_9\text{Fe}_2\text{Si}_2$ , T-Phase, and  $\text{Mg}_2\text{Si}$  in order of increasing abundance. Here the most prominent phases were  $\text{Al}_9\text{Fe}_2\text{Si}_2$ , T-Phase, and  $\text{Mg}_2\text{Si}$ . The Equilibrium results at 530°C show only the presence of  $\text{Al}_9\text{Fe}_2\text{Si}_2$ , as the previously mentioned phases are no longer stable at that temperature and will have dissolved back into the matrix.

These results can be used to determine the phases present in powder microstructure, but it is important to note that the data used to create the Thermo-Calc databases was taken from cast or wrought samples, rather than powder samples. Given this, it is possible that there are discrepancies between the powder microstructure and the predicted models as the kinetics for powders are significantly faster than their wrought counterparts due to their smaller size.

#### 6.3.3.2.2 As-Manufactured Powder

Once sectioned and thinned, the samples were analyzed by TEM HAADF, EDS maps and EDS point quantifications. While thinner samples were specifically extracted to remove interaction effects from the matrix or overlapping phases, there were still many instances where the secondary phases were thinner than the lamella. This was taken into consideration during analysis of the point quantifications; if there is matrix behind the analyzed phase, the quantification will show a higher Mg content, as the matrix is richer in Mg than in Si. Alternatively, if there is an Fe-rich phase behind the analyzed phase, the quantification will show a lower Mg content, as the Fe-rich phases contain more Si than Mg. With this in mind, all of the Mg-rich phases were found to be  $Mg_2Si$  with varying morphologies.

Figure 36 displays images of as-manufactured powder. Figure 36a shows an SEM image of an as-manufactured powder particle. The channeling contrast reveals clusters of similarly oriented sub-grains with phases at the sub-grain boundaries, consistent with what is reported in the literature for powders.<sup>10,21,22,24,74,77-79</sup> Figure 36b shows a low-magnification TEM-HAADF image of a similar sample. Figure 36c shows a higher magnification TEM-HAADF image of an as-manufactured sample. Note the continuous nature of the phases at the sub-grain boundaries. These, and similar microstructures, were analyzed in the image analysis software to determine the phase fraction of the secondary phases. It was found that there was 1.62% (area)  $Mg_2Si$  and 3.42% (area) Fe-rich phases present in the as-manufactured samples.

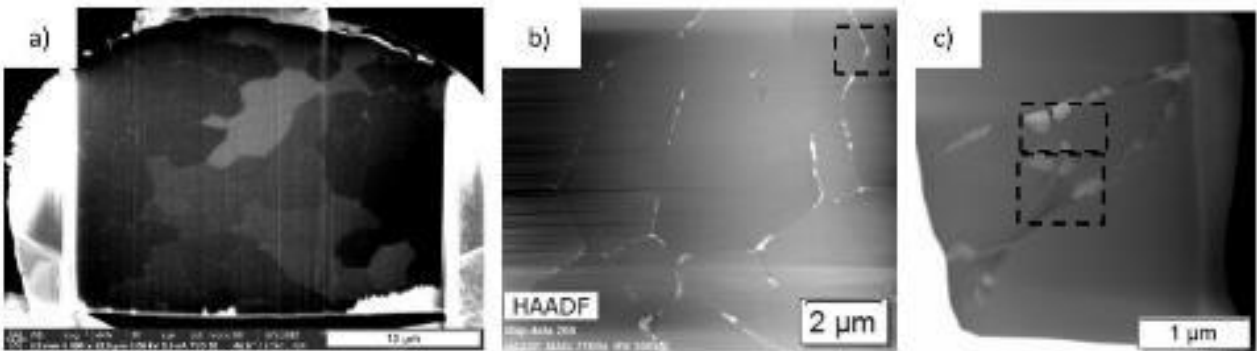


Figure 36: Overview images of as-manufactured Al 6061: (a) SEM, (b) TEM-HAADF, (c) increased magnification HAADF from (b). Outlined regions show where further analysis will be highlighted.

Additionally, EDS point analysis quantification was performed at multiple points at the subgrain interiors to determine the matrix composition. The average matrix composition was found to have 97.56 wt% Al, 1.16 wt% Mg, 0.04 wt% Fe, and 0.02 wt% Si with trace amounts of the remaining elements. The solubility limit of Mg in Al is less than 0.5 wt% at room temperature (as predicted by Thermo-Calc simulations). This demonstrates that the Mg composition in the Al matrix in these powders is higher than the solubility limit. This confirms the super saturated nature of the powders due to rapid solidification.

Figure 37 shows a HAADF micrograph of a triple point boundary with elemental EDS maps for Al, Cu, Fe, Mg, and Si. Figure 37g shows the highlighted region of Figure 4a magnified, where the atomic lattice of the precipitate can be seen as incoherent with that of the matrix. From the elemental maps, it can be concluded that this is a rod-like  $Mg_2Si$  particle with an Fe-rich phase surrounding it. This morphology

appears to be unique to powders. The composition from point analysis combined with the incoherent nature of the phase boundary indicates the phase is  $Mg_2Si$  and not a metastable precursor.

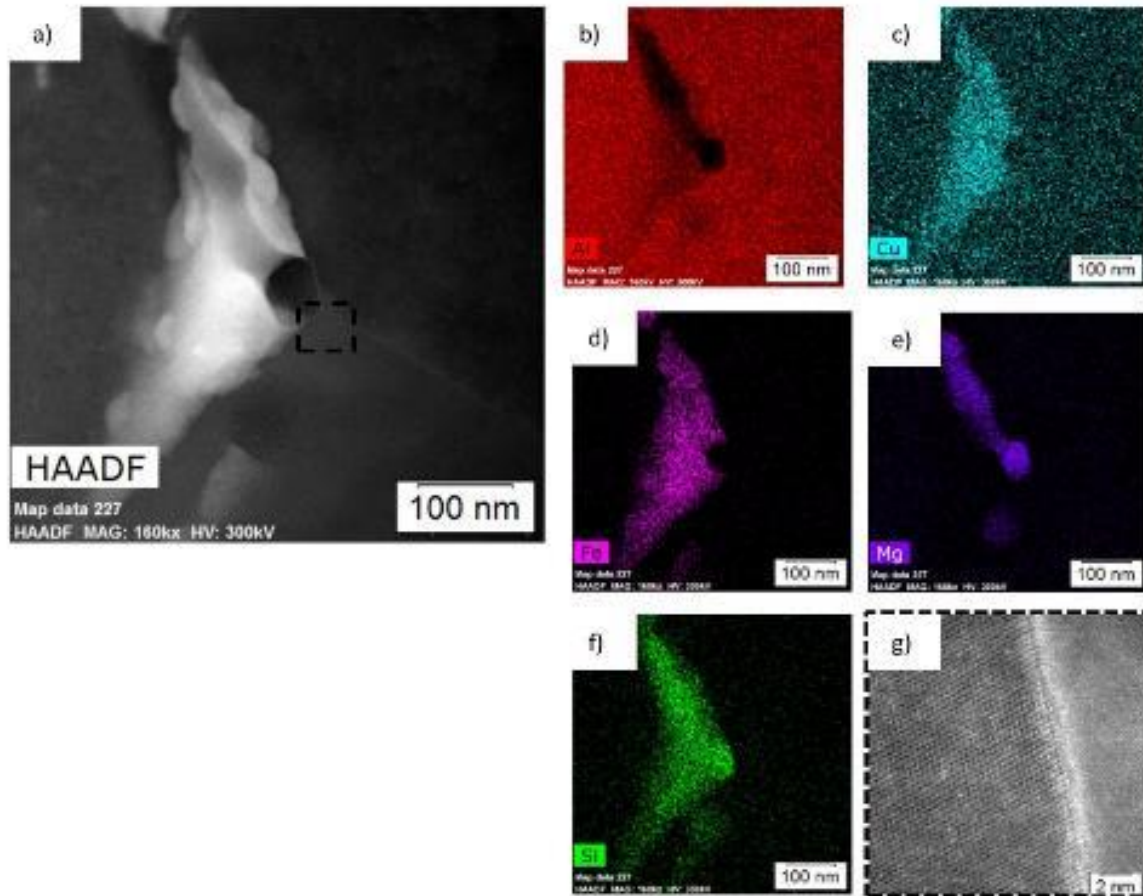


Figure 37: (a) HAADF image of a triple point in as-manufactured Al 6061. Elemental EDS maps for: (b) Al, (c) Cu, (d) Fe, (e) Mg, (f) Si. (g) High-magnification HAADF of highlighted region in (a).

Figure 38a shows a HAADF image of  $Mg_2Si$  and Fe-rich particles along a grain boundary, along with elemental EDS maps for Al, Cu, Fe, Mg, and Si. It can be seen that Si is present in both the Mg- and Fe-rich phases. These have different morphologies than the  $Mg_2Si$  and Fe-rich phase in Figure 37.

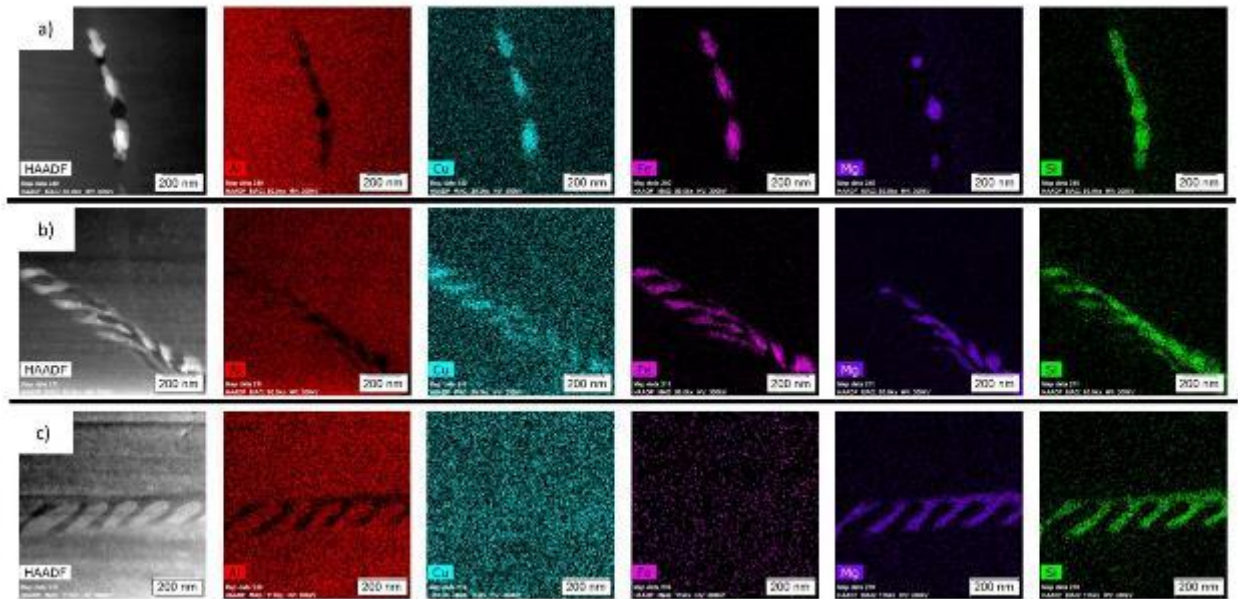


Figure 38: Elemental EDS maps and HAADF images of Mg-rich phases at a boundary in as-manufactured Al 6061: (a) alternating Mg<sub>2</sub>Si and Fe-rich phases (left to right: HAADF image, Al, Cu, Fe, Mg, Si), (b) alternating Mg<sub>2</sub>Si and Fe-rich phases in a different orientation (left to right: HAADF image, Al, Cu, Mg, Si), (c) unique Mg<sub>2</sub>Si morphology at a boundary (left to right: HAADF image, Al, Cu, Fe, Mg, Si)

Figure 38b shows a HAADF image of Mg<sub>2</sub>Si and Fe-rich phases in a lamellar structure along a boundary. This microstructure is consistent with that of cellular precipitation, which is more likely to be the mechanism of precipitation in non-equilibrium systems. This morphology of Mg<sub>2</sub>Si is particularly different than seen in castings. A perpendicular view of the cellular precipitates can be seen in Figure 38a.

Figure 38c shows a HAADF image of Mg<sub>2</sub>Si in another cellular structure with the Al-matrix, along with elemental EDS maps for Al, Cu, Fe, Mg, and Si. Here, there is no Fe-rich phase interacting with the Mg<sub>2</sub>Si, so this is yet another unique morphology.

Figure 39 shows additional morphologies of the Mg<sub>2</sub>Si (dark-contrasting phase) present in the as-manufactured powders at various magnifications. All of the unique morphologies seen in the as-manufactured powders can be attributed to the rapidly-solidified, non-equilibrium structure.

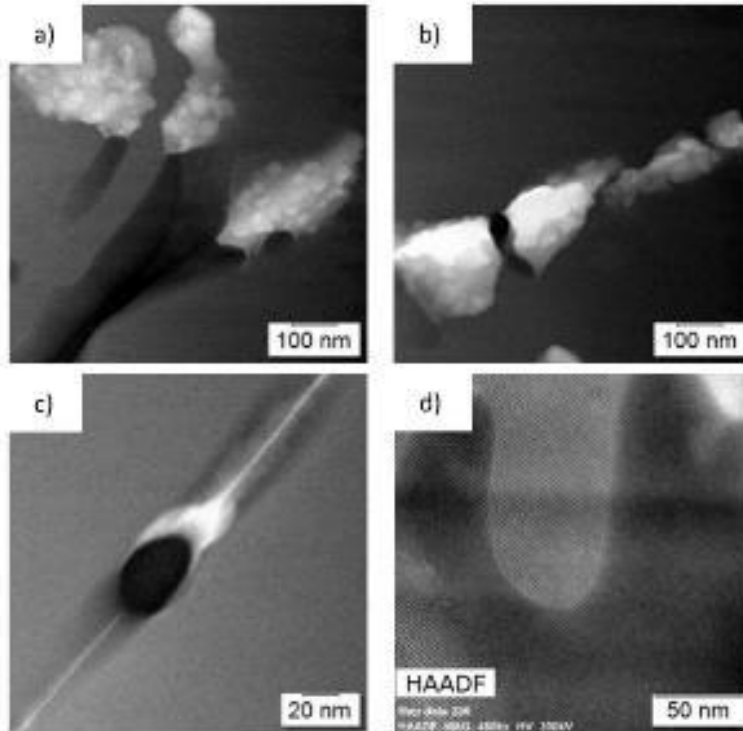


Figure 39: Additional morphologies of  $Mg_2Si$  in as-manufactured Al 6061: (a) Fe-rich phase on  $Mg_2Si$ , (b) alternating Fe-rich and  $Mg_2Si$  on a boundary, (c)  $Mg_2Si$  on a boundary, (d) atypical  $Mg_2Si$  morphology.

The thermodynamic and kinetic models in Figure 35 predict that other Mg-containing phases should be present in the as-manufactured condition, however,  $Mg_2Si$  is the only Mg-rich phase seen in these gas atomized Al 6061 powders. The discrepancy stems from the models being created using data for wrought conditions. This further emphasizes the need to understand powders in both models and experiments.

Figure 40 shows a higher magnification HAADF image of a triple point in the as-atomized condition. Again, it can be seen that the Fe-rich phases and  $Mg_2Si$  are intertwined with one another. Point EDS quantification of the Fe-rich phases reveals it to be  $Al_{13}Fe_4$  of various morphologies. As reported in literature and predicted by the thermodynamic and kinetic simulations (Thermo-Calc),  $Al_{13}Fe_4$  can contain Cu, Mn, Si, and Zn in addition to the Al and Fe. Using image thresholding to quantify the amounts of these phases, it was determined that there was 0.4% (area)  $Mg_2Si$  and 2.5% (area)  $Al_{13}Fe_4$ .

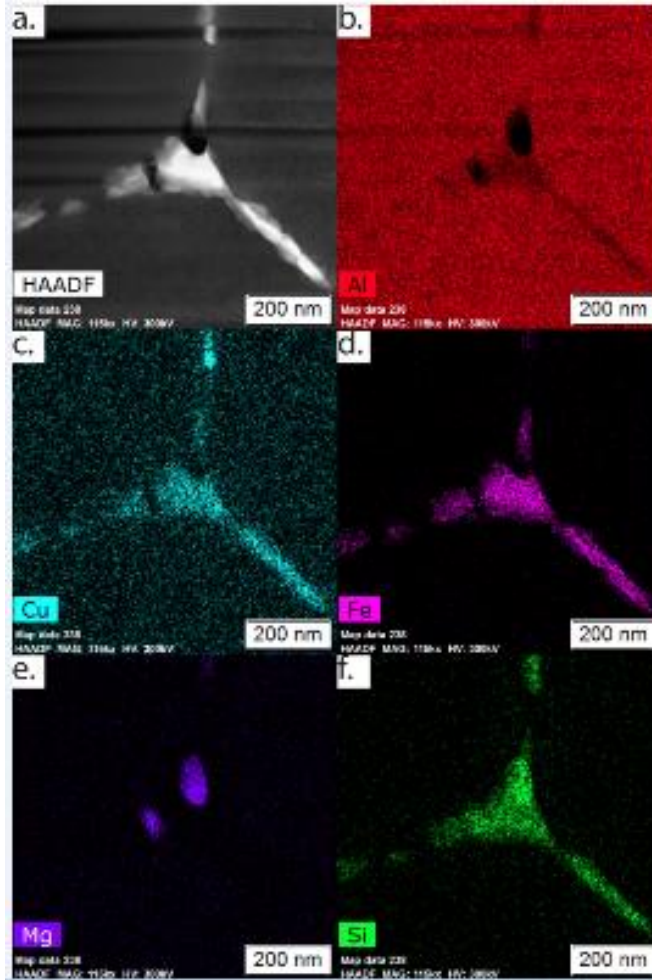


Figure 40: Higher magnification a) HAADF, and EDS maps of b) Al, c) Cu, d) Fe, e) Mg, and f) Si showing  $Mg_2Si$  and  $Al_{13}Fe_4$  at a triple point in the as-atomized powder.

### 6.3.3.2.3 Thermally Treated Powder

Figure 41a shows an SEM image of a thermally treated powder particle. Figure 41b shows a low-magnification TEM image of a similar sample. Figure 41c shows a higher magnification TEM image of a thermally treated sample. Note the discrete phases, in contrast to the continuous nature of the phases present in the as-manufactured sample. This structure is consistent with what is reported in the literature for powders.<sup>10,21,22,24,74,77-79</sup>

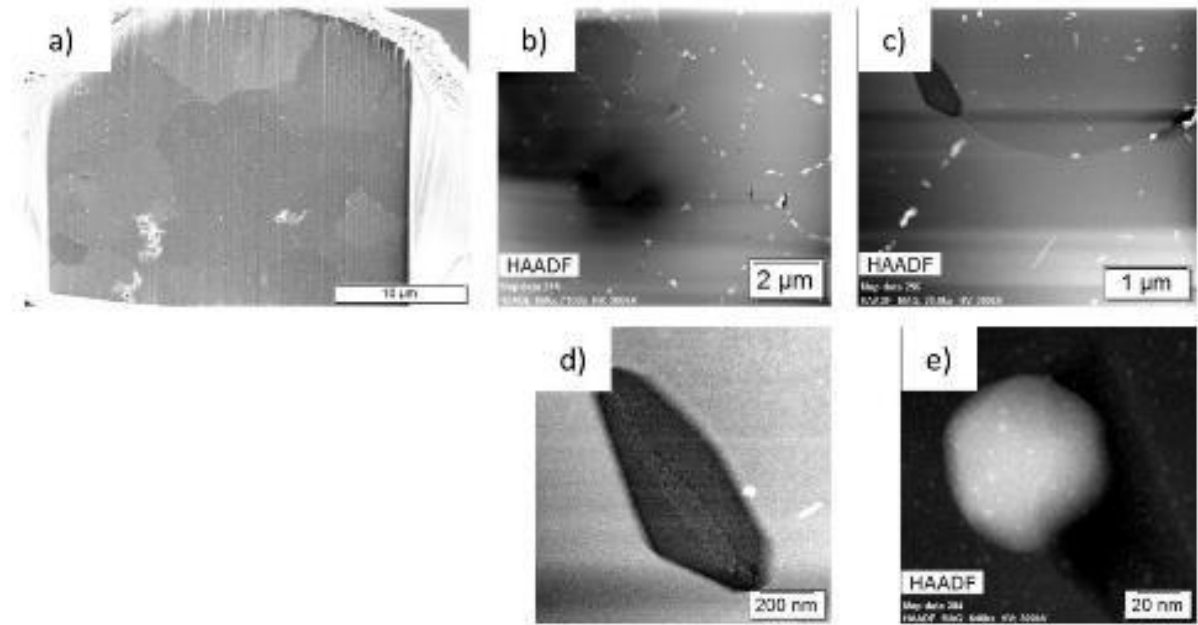


Figure 41: Overview images of thermally treated Al 6061: (a) SEM, (b) TEM HAADF, (c) increased magnification HAADF of similar sample, (d) Mg<sub>2</sub>Si of plate-like morphology, (e) Mg<sub>2</sub>Si dissolving.

Additionally, note the qualitative decrease in the dark-contrasting Mg<sub>2</sub>Si. These, and similar micrographs, were used in the image analysis software to determine the phase fraction of the Mg<sub>2</sub>Si. It was found that there was 0.81% (area) Mg<sub>2</sub>Si, a decrease from the as-manufactured samples, and 4.4% (area) Fe-rich phases, an increase from the as-manufactured sample.

Figure 41d-e shows examples of two Mg<sub>2</sub>Si morphologies in the thermally treated condition. Figure 41d shows an Mg<sub>2</sub>Si particle at a prior triple point, while Figure 41e shows a much smaller Mg<sub>2</sub>Si particle with an Fe-rich phase. Based on Figure 35, all Mg<sub>2</sub>Si should dissolve at the treatment temperature. It is hypothesized that the Mg<sub>2</sub>Si at the triple points spheroidizes to a more equilibrium plate-like shape prior to dissolving, while Mg<sub>2</sub>Si on the grain boundaries dissolves. The point quantification analysis, along with the semi-coherent atomic lattice structure seen in Figure 41d, indicates these phases are Mg<sub>2</sub>Si rather than a metastable precursor.

A longer treatment time is necessary to fully dissolve all the Mg<sub>2</sub>Si and reach the equilibrium structure predicted by Figure 35a. However, it has been shown in SEM studies that the Fe-rich phases continue to grow, and thus results in a more heterogeneous microstructure.<sup>22</sup> Treatment times must be optimized for each application, depending upon whether the goal is a homogenous microstructure or the complete dissolution of Mg<sub>2</sub>Si. Fe-rich phases tend to act as nucleation sites for cracks and have been known to cause poor wear properties, however at least partially-solutionizing the powder has been shown to increase ductility during the solid state metal additive manufacturing process cold spray.<sup>10,24,77</sup> It has been hypothesized that the Fe-rich phases control the mechanical properties of this powder, but given the amount of different types of Fe-rich phases predicted by Figure 35, and the fact that model predictions were inaccurate for Mg<sub>2</sub>Si, identification of the Fe-rich phases is an extensive study that will be reported separately.<sup>22</sup>

The thermodynamic and kinetic models in Figure 35 predict the  $\text{Mg}_2\text{Si}$  should be fully dissolved at  $530^\circ\text{C}$ , however, some  $\text{Mg}_2\text{Si}$  is still present in these thermally treated gas atomized Al 6061 powders at this temperature. The discrepancy stems from the models being created using data for wrought conditions, and also the treatment time not being long enough to reach equilibrium. This further emphasizes the need to understand powders in both models and experiments.

Figure 41 shows a HAADF image and overview EDS maps of the powder microstructure in the thermally treated condition. Note the Fe-rich phases and  $\text{Mg}_2\text{Si}$  are no longer intertwined. Figure 6 shows high magnification HAADF and EDS maps of an Fe-rich phase. Note the incoherent boundaries, the accumulation of Cr at the outside of the phase, and the clusters of Mg on the boundary. Point EDS quantification of the Fe-rich phase reveals it to be  $\text{Al}_9\text{Fe}_2\text{Si}_2$ . What has been reported in literature, and what is predicted by thermodynamic and kinetic simulations (Thermo-Calc), indicate that  $\text{Al}_9\text{Fe}_2\text{Si}_2$  has a more stoichiometric ratio of  $\text{Al}_{0.6}\text{Fe}_{0.15}\text{Si}_{0.1}(\text{Al},\text{Si})_{0.15}$ . Using image thresholding to quantify the amounts of these phases, it was determined that there was 0.9% (area)  $\text{Mg}_2\text{Si}$  and 4.0% (area)  $\text{Al}_9\text{Fe}_2\text{Si}_2$ .

Based on Figure 35, it is hypothesized that, upon heating, the  $\text{Al}_{13}\text{Fe}_4$  dissolves, resulting in an area of matrix supersaturated in Fe, Si, and Cu. Upon prolonged exposure to elevated temperature, the Cu easily diffuses throughout the matrix. Since the  $\text{Al}_{13}\text{Fe}_4$  was intertwined with the  $\text{Mg}_2\text{Si}$ , those regions with Fe and Si supersaturated in the matrix are still intertwined with the  $\text{Mg}_2\text{Si}$ . After the dissolution of the  $\text{Al}_{13}\text{Fe}_4$ , the  $\text{Al}_9\text{Fe}_2\text{Si}_2$  readily forms, often nucleating on an undissolved  $\text{Mg}_2\text{Si}$ . It is not uncommon for there to be residual  $\text{Mg}_2\text{Si}$  after treatment at  $530^\circ\text{C}$ .<sup>4</sup>

$\text{Al}_{13}\text{Fe}_4$  can contain Cu, Mn, Zn, and Si in addition to the Al and Fe; however, EDS maps indicate that Cu and Si are present but not Mn or Zn. It is important to consider the overall composition of the alloy (Table 3) and note that there is less than 0.05 wt% of both of these elements, making their presence difficult to detect unless highly concentrated.

Additionally,  $\text{Al}_9\text{Fe}_2\text{Si}_2$  should not contain Cu, Mn, or Cr, contrary to what is seen in the maps in Figure 42 and Figure 43. Given that the  $\text{Al}_9\text{Fe}_2\text{Si}_2$  formed in a region formerly supersaturated with Cu, it is not unreasonable to assume that some excess Cu was remaining in that area during cooling after the heat treatment that was incorporated into the  $\text{Al}_9\text{Fe}_2\text{Si}_2$ . Prior to heating, the Cr and Mn were homogeneously supersaturated in the matrix. During heating, this likely remained. A major difference between the two conditions is cooling rate; the as-atomized sample was rapidly solidified and experienced cooling rates on the order of  $10^5$ - $10^6$   $^\circ\text{C}/\text{min}$  whereas the thermally treated sample was quenched and experienced cooling rates on the order of  $10^2$   $^\circ\text{C}/\text{min}$ . With the slower cooling rate, the matrix was likely unable to maintain the supersaturation with Cr and Mn, leading to the accumulation of those elements at the  $\text{Al}_9\text{Fe}_2\text{Si}_2$  at the boundaries. Point EDS quantification of the  $\text{Al}_9\text{Fe}_2\text{Si}_2$  revealed the exact composition to include 0.01 wt% Mn and 0.01 wt% Cr, which is considered trace amounts. To fully understand the transformations occurring in this system, hot stage TEM will be performed in future work.

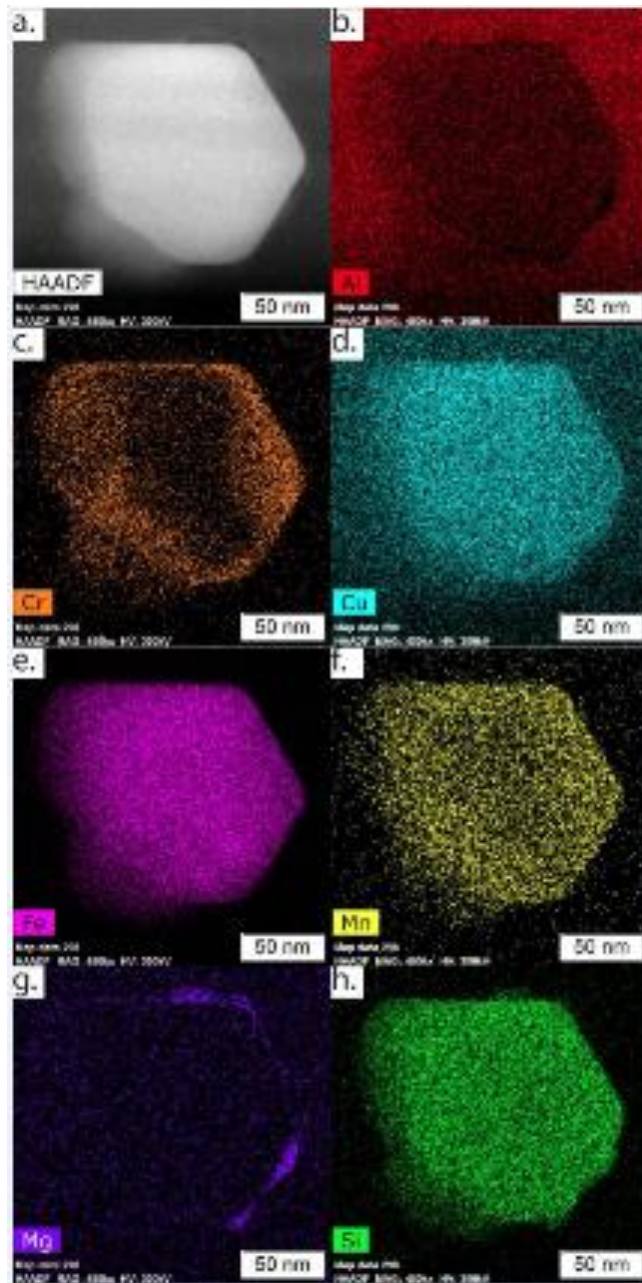


Figure 42: a) HAADF, and EDS maps b) Al, c) Cr, d) Cu, e) Fe, f) Mn, g) Mg, and h) Si showing  $\text{Al}_9\text{Fe}_2\text{Si}-2$  and residual  $\text{Mg}_2\text{Si}$  in the thermally treated powder.

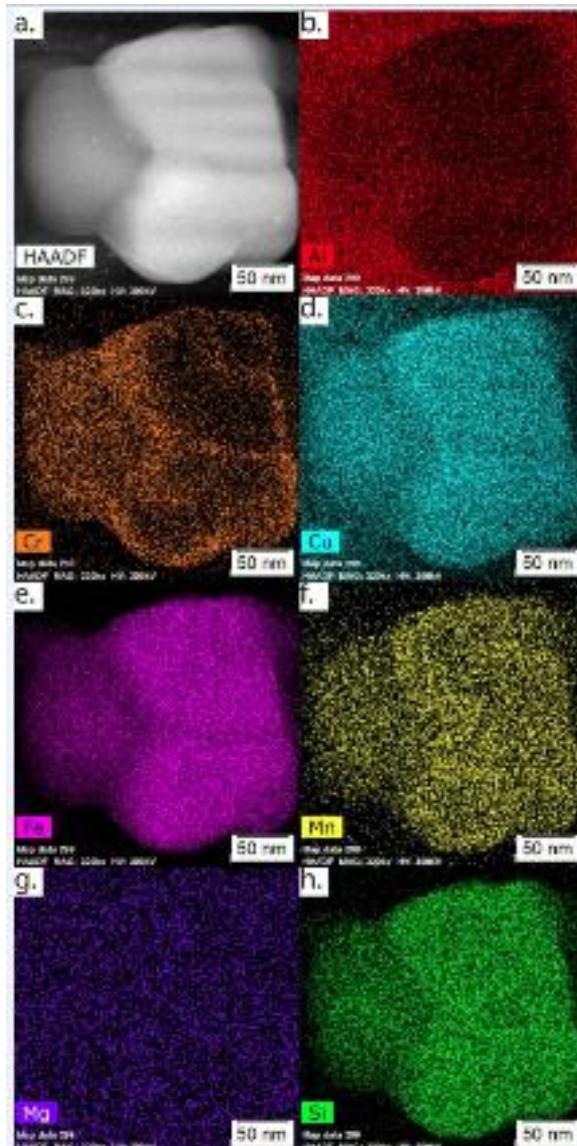


Figure 43: a) HAADF, and EDS maps of b) Al, c) Cr, d) Cu, e) Fe, f) Mn, g) Mg, and h) Si showing another morphology of  $Al_9Fe_2Si_{-2}$  in the thermally treated powder.

Previous work done by Walde et al. reports phase fractions for the Mg- and Fe-rich phases in powders in the same conditions as studied here, however work is performed here in TEM rather than SEM [presented in Section 0

Solution Treatment]<sup>22</sup>. Due to the smaller interaction volume, TEM can provide better insights into the amount of phases present than SEM, as some of the phases present are smaller than the interaction volume of the SEM beam, a limitation acknowledged by the authors. They report no measurable Mg-rich phases and 16% (area) Fe-rich phases in the as-manufactured powder, with less than 1% (area) Mg-rich phases and 4.5% (area) Fe-rich phases in the thermally treated powder. Both the numbers and trends vary greatly from the results reported here. This discrepancy is likely due to the limitations of the SEM beam as previously discussed; TEM analysis revealed many precipitates that are too small for an SEM to detect.

It is important to remember the type of sample considered here is rapidly solidified powders. Given the finer microstructural features in powders, as compared to their wrought counterparts, the shorter diffusion distances and metastable conditions have a great effect on the phase type, morphology, and chemistry seen in the powders. In general, the  $Mg_2Si$ ,  $Al_{13}Fe_4$  and  $Al_9Fe_2Si_2$  have morphologies different than their wrought counterparts.

#### 6.3.3.3 7075

This work has been submitted in part for publication as:

**C. Walde**, K. Tsaknopoulos, V. Champagne, & D. Cote. Phase Transformations in Thermally Treated Gas-Atomized Al 7075 Powder. *Metallurgical and Materials Transactions A*. Under Review.

Due to the large interaction volume in the SEM, EDS was not successful in further differentiating the light- and dark-contrasting phases into the constituents predicted in Thermo-Calc. Hence, EDS was performed in a TEM.

Figure 44 shows overview TEM micrographs of the as-atomized and thermally treated conditions for 60 minutes at each temperature. Figure 44a shows a similar structure as seen in the SEM in Figure 25a; on the other hand, Figure 44b and Figure 44c provide much more detail than their SEM counterparts in Figure 26. Figure 45, Figure 46, and Figure 47 show higher magnification TEM micrographs and corresponding EDS maps to give further insight into the specific constituents present in each condition.

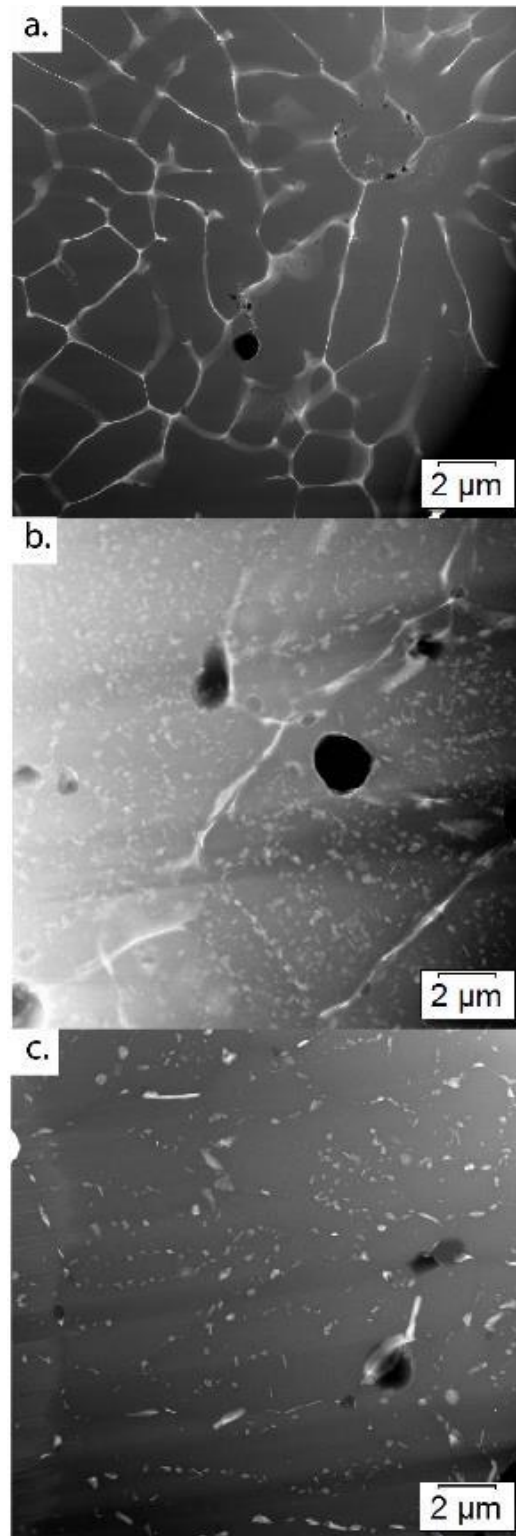


Figure 44: Overview TEM micrographs for 7075 of a) the as-atomized condition, b) 60min at 465 °C and c) 60min at 480 °C.

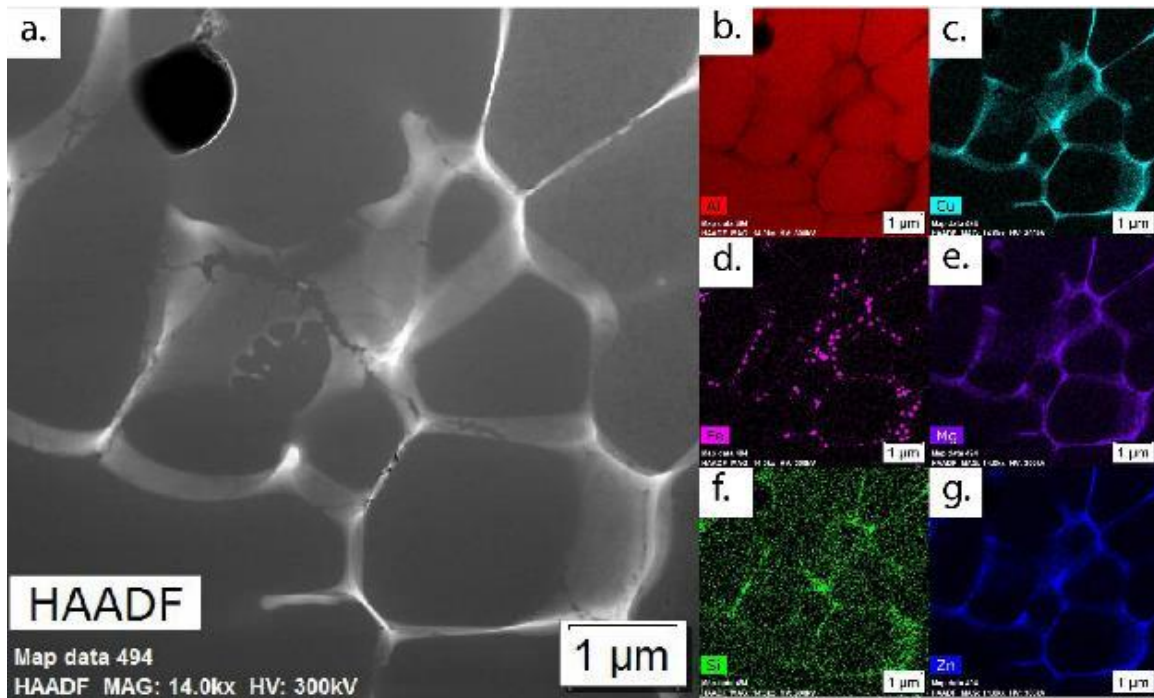


Figure 45: TEM micrograph and EDS maps for 7075 for the as-atomized condition; a) HAADF, b) Al, c) Cu, d) Fe, e) Mg, f) Si, and g) Zn

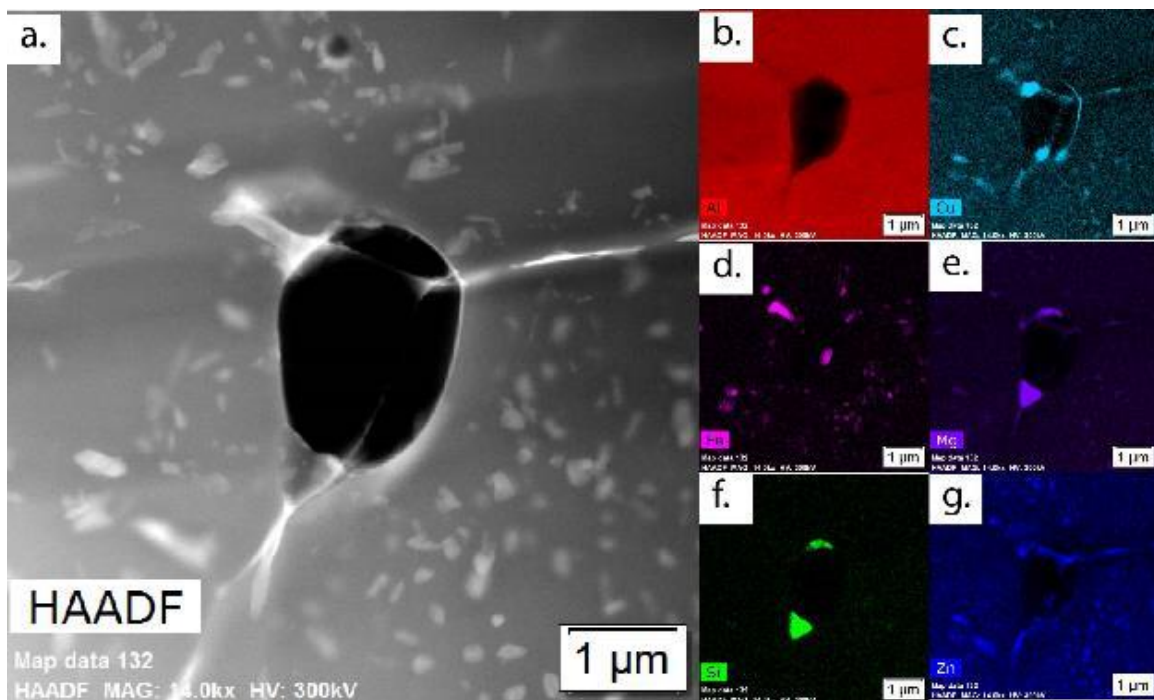


Figure 46: TEM micrograph and EDS maps for 7075 for the 60min at 465 °C condition; a) HAADF, b) Al, c) Cu, d) Fe, e) Mg, f) Si, and g) Zn.

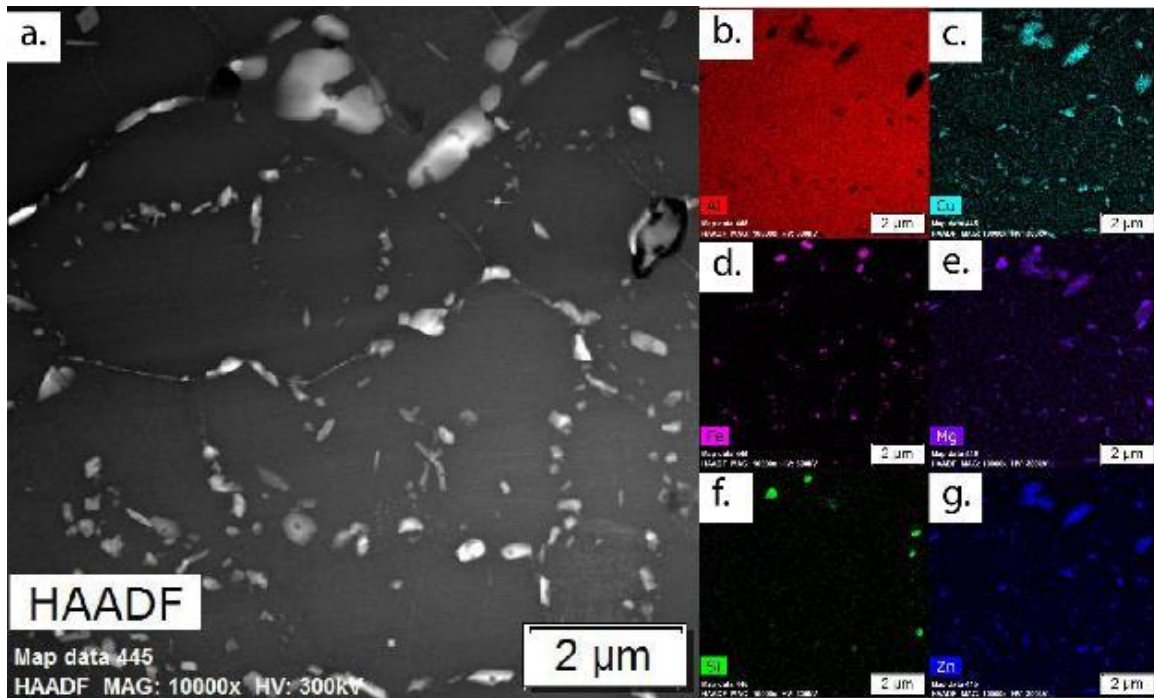


Figure 47: TEM micrograph and EDS maps for 7075 for the 60min at 480 °C condition; a) HAADF, b) Al, c) Cu, d) Fe, e) Mg, f) Si, and g) Zn.

Figure 45 shows TEM micrograph and EDS maps for the as-atomized condition. Note the presence of two phases – an Al-Cu-Mg-Zn network phase and discrete Fe-rich phases. EDS point quantification revealed the Al-Cu-Mg-Zn network to be T-phase and the discrete Fe-rich phases to be  $Al_7Cu_2Fe$ , which is consistent with what is seen in literature. Additionally, the dark-contrasting phase seen in the thermally treated SEM micrographs (Figure 26 and Figure 27) is also found in the as-atomized structure using TEM, and has been identified as  $Mg_2Si$ .

Figure 46 shows TEM micrograph and EDS maps for the sample thermally treated at 465 °C for 60 minutes. Note the presence of four phases – an Al-Cu-Mg-Zn phase, an Al-Cu-Mg phase, an Fe-rich phase, and a Si-rich phase. EDS point quantifications revealed the Al-Cu-Mg-Zn phase to be residual T-phase that had not fully dissolved, the Al-Cu-Mg phase to be S-phase, the Fe-rich phase to be the  $Al_7Cu_2Fe$ , and the Si-rich phase to be  $Mg_2Si$ . Based on the equilibrium diagram in Figure 12, S-phase is not expected to be present at this temperature; this indicates a difference in the local equilibrium for the powder in comparison to the global powder composition as measured by direct current plasma emission spectroscopy.

Figure 47 shows TEM micrograph and EDS maps for the sample thermally treated at 480 °C for 60 minutes. Note the presence of three phases – an Al-Cu-Mg-Zn phase, an Fe-rich phase, and a Si-rich phase. EDS point quantifications revealed the Al-Cu-Mg-Zn phase to be residual T-phase that had not fully dissolved, the Fe-rich phase to be the  $Al_7Cu_2Fe$ , and the Si-rich phase to be  $Mg_2Si$ . Note the lack of the S-phase that was present in the 465 °C thermally treated condition.

An unexpected similarity between the treatment temperatures is the presence of T-phase seen in Figure 46 and Figure 47. The equilibrium predictions indicate that T-phase should not be present at either temperature; this indicates that 60 minutes of treatment at either temperature is not sufficient time to

dissolve the T-phase. As Scheil simulations predict T-phase to be the most abundant phase, it is expected that it may take additional time to dissolve. Unfortunately, it is not possible to distinguish between the T-phase and  $\text{Al}_7\text{Cu}_2\text{Fe}$  in the SEM (Figure 26), so further TEM work would be needed to determine if 120 minutes or 240 minutes of treatment is sufficient to fully dissolve T-phase.

Additionally, large and small phases can be seen in both the SEM and TEM micrographs; they have been identified as both T-phase and  $\text{Al}_7\text{Cu}_2\text{Fe}$ , with sizes corresponding to different boundary types. The high-angle boundaries have more open space, hence the phases can be larger there, whereas the phases at the low-angle boundaries have less open space for growth.

Of significant note is the difference in precipitate locations between the 465 °C and 480 °C treatment temperatures; the 465 °C treatment has precipitates both at the boundaries and in the bulk of the grains, whereas the 480 °C only has precipitates at the boundaries. Because the grains are so small in these gas-atomized powders and there is such a small diffusion distance to the grain boundaries from the center of the grains, the driving force for precipitation on the boundaries is easily achievable, thus precipitation will occur first and most frequently on the grain boundaries. However, it is possible for the boundaries to become saturated. This is the case in the 465 °C treatment. The boundaries are saturated with T-phase and  $\text{Al}_7\text{Cu}_2\text{Fe}$  so the S-phase can only precipitate in the bulk matrix. This can be seen in both the SEM and TEM micrographs.

Given the increase in understanding of the phases present in each condition from study in TEM, it is beneficial to revisit Figure 27 to further understand the trends found in the SEM analysis. Recall the increasing trend in the bright-contrasting phases in the 480 °C treatments at 60 minutes; in TEM, two different bright-contrasting phases were identified at the boundaries:  $\text{Al}_7\text{Cu}_2\text{Fe}$  and T-phase. As previously stated, the T-phase is in the process of dissolving, so this increase is likely due to the coarsening of the  $\text{Al}_7\text{Cu}_2\text{Fe}$  at a faster rate than the T-phase dissolution. It is expected that after 120 minutes of treatment, the T-phase would be fully dissolved and the  $\text{Al}_7\text{Cu}_2\text{Fe}$  reached a stable size and fraction, reflected in the plateau in Figure 27. In comparison, at 60 minutes of treatment at 465 °C, there is a decreasing trend in the bright-contrasting phases in the SEM. This trend is surprising because based on the TEM results, there are three different bright-contrasting phases present –  $\text{Al}_7\text{Cu}_2\text{Fe}$  and T-phase at the boundaries and S-phase in the bulk of the grains. Because S-phase is forming,  $\text{Al}_7\text{Cu}_2\text{Fe}$  cannot coarsen. In SEM, S-phase was not detected in the bulk, but this is likely due to the limiting resolution of the SEM; this causes the area fraction to appear lower than expected based on TEM results. With this in mind, it is important to understand the limitations of individual characterization techniques and utilize multiple techniques.

### 6.3.4 Conclusions

#### 6.3.4.1 2024

Electron microscopy revealed that the phases present in the as-received condition were found to be S-phase and  $\text{Al}_2\text{Cu}$ , which is consistent with non-equilibrium Scheil solidification predictions. Additionally, it was shown that at 490°C the S-phase dissolves and the remaining high elemental concentration forms  $\text{Al}_6\text{Mn}$  while the  $\text{Al}_2\text{Cu}$  grows from discs to plates.

The primary goal of a high temperature solutionization or homogenization treatment is to dissolve the secondary phases. Due to unique powder precipitation kinetics, this was not achieved in this study. SEM

micrographs showed the thermal treatment to not have homogenized the microstructure. Rather, the thermal treatment transformed some phases, and TEM was necessary to identify the precipitation sequences with the aid of thermodynamic modeling. Future work evaluating other treatment temperatures is needed. It was shown here that, due to the higher percentage of grain boundary area acting as diffusion highways and the small grain sized leading to small diffusion distances to those highways, much shorter solutionization times will be needed for powders compared to their wrought counterparts.

#### 6.3.4.2 6061

Through extensive TEM and EDS analysis, this work demonstrates how the internal microstructure of commercial alloy compositions in the powder form differ from those present in the wrought condition. It was shown that Al 6061 powder contains  $Mg_2Si$  of highly atypical morphologies in the as-manufactured condition. Once thermally treated, the smaller  $Mg_2Si$  precipitates dissolve and the larger ones spheroidize to the more equilibrium plate- or cube-like structures. This greatly differs from the microstructures seen in the wrought versions of the same commercial alloy composition and from the amounts of  $Mg_2Si$  predicted by thermodynamic and kinetic models. It was shown that  $Al_{13}Fe_4$  was present in the as-atomized condition and transforms to  $Al_9Fe_2Si_2$  after a treatment of 1 hour at 530 °C. Since parts made via MAM techniques can retain microstructural features of the feedstock powder in the consolidated part, it is beneficial to understand the microstructure of the feedstock powder prior to consolidation.

There is opportunity for further optimization of the thermal treatment for individual applications; it is not possible to achieve a fully homogenous microstructure as the Fe-rich phases grow as the  $Mg_2Si$  dissolves. Understanding the transformations of the phases during thermal treatment can be studied through hot stage TEM; these transformation kinetics are important inputs into dissolution and growth models.

#### 6.3.4.3 7075

Extensive electron microscopy revealed the presence of T-Phase,  $Al_7Cu_2Fe$ , and  $Mg_2Si$  in the as-atomized condition of this gas-atomized Al 7075 powder. Thermal treatments were performed with the goal of homogenizing the microstructure – dissolving T-phase while avoiding S-phase growth, avoiding  $Al_7Cu_2Fe$  coarsening, and avoiding melting. 465 °C was chosen because the  $Al_7Cu_2Fe$  should coarsen slower at a lower temperature, and this is as low as possible without containing S-phase. 480 °C was chosen because it is the conventional solutionization temperature used for Al 7075. In the samples treated at 465 °C, S-phase was present, indicating a shift in local equilibrium of the powders as compared to the global composition of the powder batch. In both treatments, 60 minutes was insufficient to fully dissolve the T-phase. Due to the large interaction volume of the SEM as compared to the size of the precipitates present in these powders, it is not possible to accurately differentiate these phases in the SEM; additional TEM would be necessary to evaluate the time required to fully dissolve the T-phase.

It is important to understand the benefits, as well as the limitations, of different microscopy techniques and utilize multiple for different purposes. The SEM is useful for high-throughput measurements and total secondary phase area quantification. However, its lower resolution does not allow for tracking individual secondary phases. The TEM is useful for its high-resolution, allowing for identification of individual phases. However, the time required for sample preparation limits its feasibility for high-

throughput evaluations. Leveraging the strengths of each technique, and coupling both of these microscopy techniques with modeling, allows for enhanced understanding of the microstructural evolution with decreased time spent on data collection.

## 6.4 3D Characterization

Gas-atomized metallic powders are commonly used in solid-state additive manufacturing processes. While their post-process consolidated properties are widely studied, there is little research on the properties of the powders before consolidation. Understanding the powder characteristics before use in additive manufacturing could lead to fine-tuning properties of additively manufactured materials. As powder properties and characteristics differ greatly from their wrought counterparts, it is important to fully understand the unique structure of these powders. It has been shown that two-dimensional micrographs may miss certain features such as shape and spatial distribution of particulates. As such, this research characterizes three-dimensionally the grain structure and secondary phases of aluminum alloy powders after various thermal processes. This is accomplished through the use of a serial sectioning technique that combines SEM images and EBSD results of numerous planes throughout the powder particles. Secondary phases are further analyzed using TEM/STEM and DSC. Results from this work can also be input to models and simulations.

### 6.4.1 Materials

The powder used for this study was the Al 6061 that was used in Section 6.1 Cast versus Powder and in Section 0

Solution Treatment; see Section 6.1 Cast versus Powder for material details.

#### 6.4.2 Method

Automated serial sectioning was performed in an FEI Helios Plasma-Focused Ion Beam (P-FIB) equipped with an electron backscatter diffraction (EBSD) detector (EDAX). Samples were mounted on the 54° side of a pre-tilted holder, near the top edge. For the single-particle sectioning, powder was dispersed on the holder then later secured with a Pt-deposition in the FIB to prevent movement.<sup>80</sup>

Milling and imaging parameters were set-up using FEI Auto-Slice-and-View. The slice thickness was 300 nm and depth of sectioning was set to the diameter of the powder particle. The EBSD step size was 0.4 μm.

3D reconstruction and image analysis was performed using Avizo software (version 9.4.0, Thermo-Fischer Scientific). Images were aligned utilizing least squares method, then a histogram equalization and despeckling filters were applied. Finally, each slice was segmented using label fields.

#### 6.4.3 Results

Similar to the 2D SEM images, the 3D reconstructions were analyzed for changes in secondary phase volume fraction (SPVF) and grain size; here, the As-Atomized and 60 min conditions of 6061 were analyzed in 3D.

Figure 48 (a) shows a small sub-volume of the full rendering of the As-Atomized condition while (b) shows the full rendering of the same particle. Figure 48 (c) shows the full rendering of the heat treated condition. Table 9 shows the SPVF for each volume compared to the SPAF for the corresponding treatments in 2D.

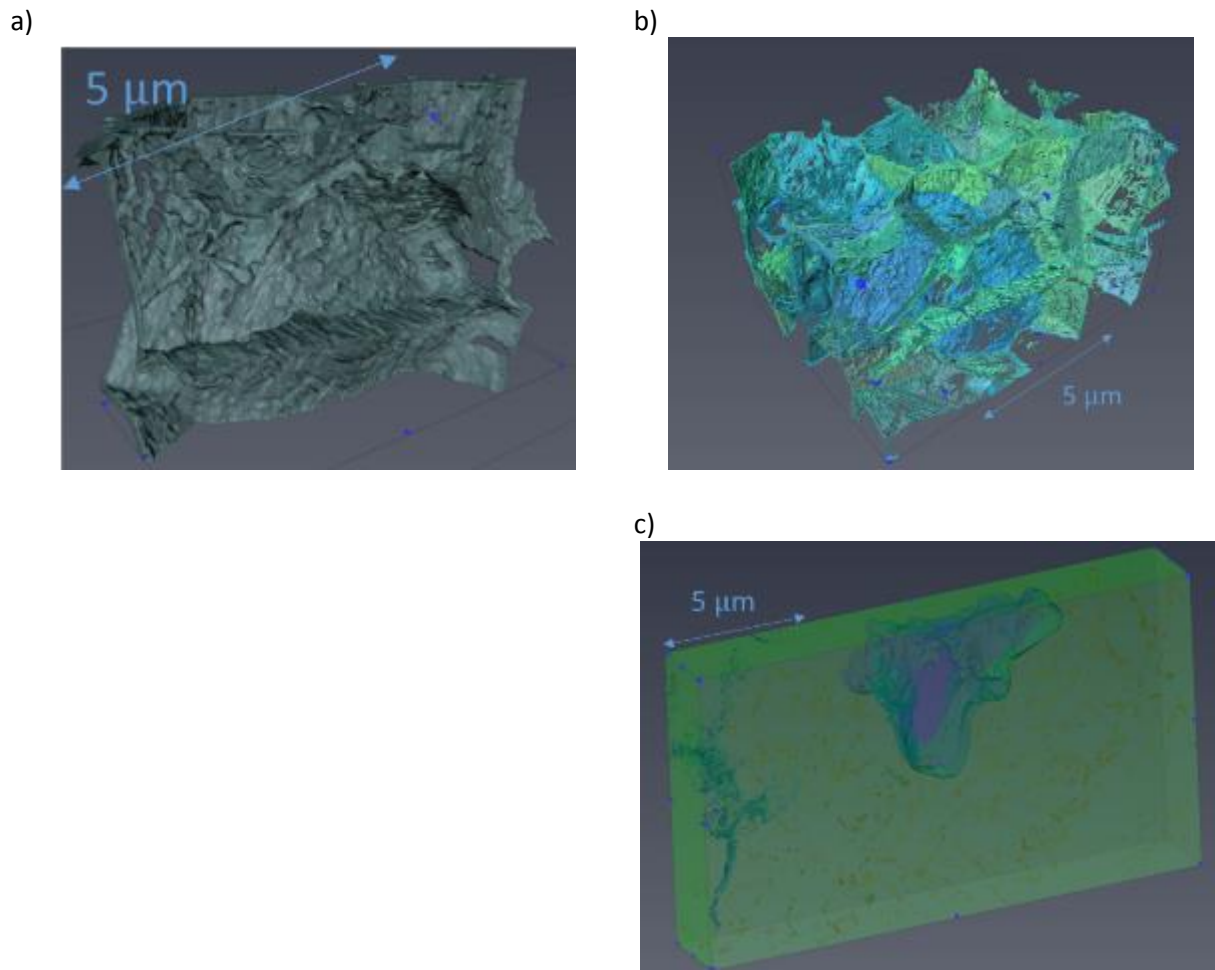


Figure 48: Volume renderings of (a) secondary phases in a sub-volume of the sectioned As-Atomized particle, (b) secondary phases in the full volume of the sectioned As-Atomized particle, (c) matrix, secondary phases, and pores in the full volume of the sectioned treated particle.

Table 9: SPVF for rendered volumes

	2D	3D	
		Sub-volume	Full volume
As-Atomized	16.0 %	11.6 %	4.9 %
Heat Treated (60 min)	1.8 %	N/A	0.2 %

Figure 49 shows select slices from each sectioning, comparing SEM and EBSD slices for both As-Atomized and treated powders.

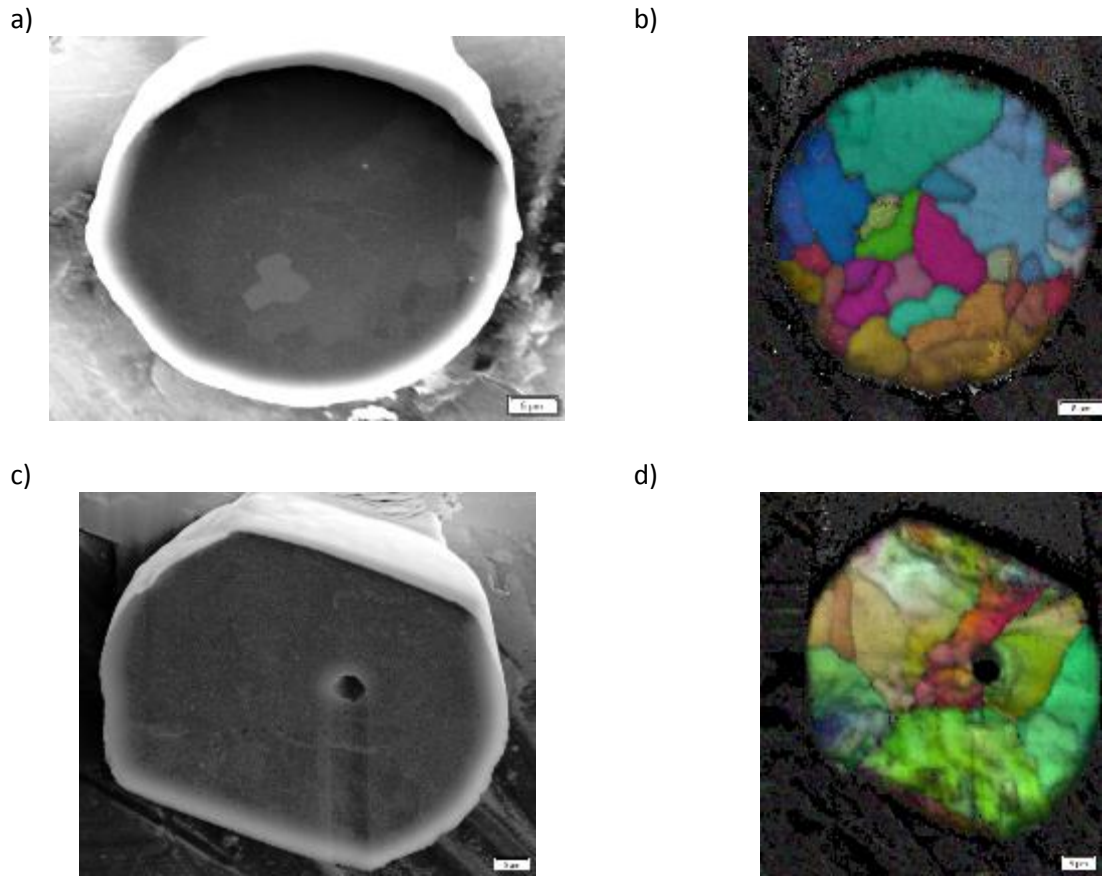


Figure 49: Slices from sectioning of (a) As-Atomized particle, SEM, (b) As-Atomized particle, EBSD, (c) treated particle, SEM, (d) treated particle, EBSD.

The measured mean grain diameter for each condition was measured as follows: 2.88  $\mu\text{m}$  (As-Atomized, SEM), 5.44  $\mu\text{m}$  (As-Atomized, EBSD), 3.79  $\mu\text{m}$  (treated, SEM), and no measurement was possible for the EBSD data for the treated sample.

#### 6.4.3.1 Grain and Cell Size

As was seen in the grain size measurements of the etched samples via light microscopy, there was no appreciable grain growth during solution treatments. This is validated by what was seen in the 2D EBSD (Figure 22). However, when the 3D EBSD (Figure 49) is viewed, the 60 min sample has a grain structure more similar to that of the 4 hour sample, rather than the other particles treated for 60 min.

When the grain diameters measured via etching are compared to those measured via EBSD, it can be seen that there is a discrepancy. This can be attributed to the presence of grains *and* cells. In the As-Atomized condition, the cells may have low-angle boundaries with each other that were not resolved with the EBSD step-size but that were revealed through etching. These cells have the same orientation as most adjacent cells, which form the grains that were measured via EBSD. When this is combined with SEM, it can be seen that the cells are outlined by the web-like structure of secondary phases.

Upon heating, these cells re-orient themselves to more closely align with all adjoining cells, resulting in the very continuous orientations seen in the 4 hours sample (2D) and 60 min sample (3D). The 3D EBSD step-size was smaller than that used in the 2D measurements, so perhaps in 2D the 60 min sample is more similar to the 4 hour sample than initially seen. The cell boundaries still exist and thus are visible via etching, but are reoriented. Additionally, the reorientation of the cells may be a confounding contributor to the changes seen in the hardness measurements.

#### 6.4.4 3D vs. 2D

Table 9 shows a comparison of the 2D and 3D secondary phase fractions (area and volume percentage, respectively). It can be seen here that the general trend is consistent between area and volume – the secondary phase fraction decreases with solution treatment; this can be attributed primarily to the dissolution of phases at the boundaries. However, the difference in percent between the respective volumes and between the volumes and the area percentages is consistent with that of the growing trend in literature showing that 2D data may really not capture the entire picture. However, the 3D data may have missed some secondary phases due to variation in the contrast during the automated process.

Additionally, the 3D reconstructions, when coupled with the appropriate material properties, can be input to a 3D model. For example, the Cold Spray Through-Process Model<sup>31</sup> utilizes Abaqus to simulate powder particle deformation during impact. Currently, the state of the art uses homogenous spheres, however these 3D microstructures can be imported and used as the internal structure of the particles to see how deformation behaves in inhomogeneous particles.

## 7 Future Work

### 7.1 Cast versus Powder

Although this study was conclusive in demonstrating the difference between the powder and cast morphologies and the differences in their response to a homogenization/solutionization thermal treatment, differences in the aging step of a heat treatment still need to be addressed.

### 7.2 Thermal Treatment

#### 7.2.1 Solution Treatment

While the equilibrium diagrams generated using Thermo-Calc were useful in determining homogenization/solutionization treatment temperatures, the research showed that powder does vary from these diagrams. As such, studies of other homogenization/solutionization treatment temperatures should be evaluated.

#### 7.2.2 Aging Treatment

The next step in the heat treatment process is aging. Since research has shown that powders differ from their cast counterparts, powder-specific aging curves should be developed.

### 7.3 3D Characterization

While the third dimension typically referenced is another distance dimension, it would be useful to understand the evolution of the same two-dimensional cross-section of powders with respect to time.

In order to most accurately understand the evolution of the granular structure of rapidly solidified powder particles during solution treatment, the same powder particle should be studied. This could be done by performing EBSD on a single powder particle cross section prior to and after several thermal treatments. This would be able to show how individual grains behave, rather than making extrapolations between the As-Atomized and Treated conditions.

Additionally, a fourth dimension could be added, if non-destructive methods were used. For example, x-ray tomography can be used to image the porosity and secondary phases of powders in three dimensions, non-destructively. Then, heat treatments could be applied to the powder particle and it can be reimaged after to watch the evolution in three dimensions. This would provide important insight into the spatial evolution of the secondary phases and pores.

### 7.4 Phase Identification

For use in the Through-Process Model, and to most accurately evaluate effectiveness of heat treatments, it is important to know exactly what phases are present in the As-Atomized condition, as well as after heat treatment. This work evaluated the as-atomized condition as well as one thermally treated condition; however, understanding the precipitation sequence during aging must still be understood. Materials

## 8 Potential Impact

This work has relevance to a number of fields:

### 8.1 Powder Metallurgy

The microstructures of rapidly solidified metallic powders has been of little interest until recently. This work has already provided insights into the unique microstructural features of these powders. It has revealed an interesting granular/sub-granular structure and shown that kinetics in these powders differ from their wrought counterparts, showing that it is necessary to evaluate thermal treatments for powder separately from those developed for their wrought counterparts. This work has the potential to show that the equilibrium phases and precipitation orders are different in powders than in their wrought counterparts.

### 8.2 Additive Manufacturing

Because there is no melting of the feedstock material in solid-state additive manufacturing techniques such as cold spray and Additive Friction Stir, the properties of the feedstock powder can be altered to have an effect on the final consolidated part. If these additive manufacturing techniques are to be used in more and more applications that require specific properties, it is important to have as much control as possible over the properties of the final part.

My solution treatment work has shown the ability to manipulate the properties of the As-Atomized powders; all that is left is to determine the properties that are optimal for each given process in a given application.

### 8.3 Thermodynamic and Kinetic Modeling

Models always need to be validated, commercially available thermodynamic and kinetic software included! These models were created for use in wrought or cast systems, not specifically for rapidly solidified powders. While the software does allow for some considerations (you *can* input the cooling rate etc.), these outputs must be validated.

My work in three-dimensional analysis has provided some parameters for comparison with model outputs – volume fraction, size, and spatial distribution of certain secondary phases. Additionally, my work on Phase Identification will show if the phases predicted by the models were correct, enabling the modeling community to make adjustments if necessary.

## 9 Relevant Presentations & Publications

### 9.1 Publications

**C. Walde**, B. Sousa, V. Champagne, & D. Cote. An Evaluation of Gas Atomized Aluminum Alloy Powders as Compared to Cast Counterparts. *Metallurgical and Materials Transactions A*. Under Review.

**C. Walde**, K. Tsaknopoulos, V. Champagne, & D. Cote. Phase Transformations in Thermally Treated Gas-Atomized Al 7075 Powder. *Metallurgical and Materials Transactions A*. Under Review.

**C. Walde**, K. Tsaknopoulos, V. Champagne, & D. Cote. The Microstructural Evolution of Rapidly Solidified Powder Aluminum 2024 during Thermal Processing. *Metallography, Microstructure, and Analysis*. Under Review.

**C. Walde**, K. Tsaknopoulos, V. Champagne, & D. Cote. Evolution of Fe-rich Phases in thermally processed aluminum 6061 powders for AM applications. *Journal of Thermal Spray Technology*. Under Review.

B. Sousa, **C. Walde**, D. Tsaknopoulos, K. Fitzpatrick-Schmidt, C. Massar, V. Champagne, & D. Cote. Initial Observation of Grain Orientation Dependent Nanoindentation Hardness of Al 6061 Gas-atomized Powder. *International Journal of Metallurgy and Metal Physics*. Under Review.

K. Tsaknopoulos, **C. Walde**, V. Champagne, & D. Cote. Gas-Atomized Al 6061 Powder: Phase Identification and Evolution During Thermal Treatment. *JOM*. 2018. <https://doi.org/10.1007/s11837-018-3175-7>

**C. Walde**, D. Cote, V. Champagne, R. Sisson. Characterizing the Effect of Thermal Processing on Powder Al Alloys for Additive Manufacturing Applications. *Journal of Materials Engineering and Performance*. 2018. <https://doi.org/10.1007/s11665-018-3550-0>

**C. Walde**, R. Ristau, & D. Cote. Automated 3D EBSD for metallic powders. *MethodsX*. 2018. <https://doi.org/10.1016/j.mex.2018.06.001>

### 9.2 Technical Conference Presentations

**C. Walde**, D. Cote, V. Champagne, Jr., R.D. Sisson, Jr., “Optimizing Thermal Parameters for Powder Pre-Processing Treatments”, MS&T 2018, Columbus, OH, October 14-18, 2018.

**C. Walde**, D. Cote, V. Champagne, Jr., R.D. Sisson, Jr., “Analysis of Aluminum Alloy Feedstock Powder used in Solid State Processes”, MS&T 2018, Columbus, OH, October 14-18, 2018.

**C. Walde**, D. Cote, V. Champagne, Jr., R.D. Sisson, Jr., “Thermal Analysis of the Effect of Thermal Processing on Powder Al Alloys used in Additive Manufacturing”, NATAS 2018, Philadelphia, PA, August 6-10, 2018.

**C. Walde**, D. Cote, V. Champagne, Jr., R.D. Sisson, Jr., “Three Dimensional Characterization of Powder Al Alloys and the Effects of Thermal processing”, TMS 2018, Phoenix, AZ, March 11-14, 2018

**C. Walde**, D. Cote, V. Champagne, Jr., R.D. Sisson, Jr., “Characterizing the Effect of Thermal Processing on Powder Al Alloys for Additive Manufacturing Applications”, MS&T 2017, Pittsburgh, PA, October 8-11, 2017

**C. Walde**, D. Cote, V. Champagne, Jr., R.D. Sisson, Jr., “Optimization of Solution Treatment Parameters for Aluminum Alloy Powders through the use of Thermal Analysis”, NATAS 2017, Newark, DE, August 7-10, 2017

**C. Walde**, D. Cote, V. Champagne, Jr., R.D. Sisson, Jr., “Feedstock Powder Analysis for Additive Manufacturing Applications”, AeroMat 2017, Charleston, SC, April 9-12, 2017

### 9.3 Technical Conference Posters

**C. Walde**, D. Cote, V. Champagne, Jr., R.D. Sisson, Jr., “Characterization of Powder Al Alloys and the Effects of Thermal Processing, in Three Dimension”, 4th International Congress on 3D Materials Science (3DMS) 2018, Elsinore, Denmark, June 10-14, 2018

**C. Walde**, D. Cote, V. Champagne, Jr., R.D. Sisson, Jr., “Characterizing the Effect of Thermal Processing on Powder Al Alloys for Additive Manufacturing Applications”, ASEE-GEM, Washington, DC, January 2018

**C. Walde**, D. Cote, V. Champagne, Jr., R.D. Sisson, Jr., “Feedstock Powder Analysis for Additive Manufacturing Applications”, Cold Spray Action Team Conference, Boston, MA, June 2017

**C. Walde**, D. Cote, V. Champagne, Jr., R.D. Sisson, Jr., “Feedstock Powder Analysis for Additive Manufacturing Applications”, TMS Conference, San Diego, CA, February 2017

**C. Walde**, D. Cote, V. Champagne, Jr., R.D. Sisson, Jr., “The Microstructural Evolution of Powder Aluminum Alloys after Thermal Processing”, Cold Spray Action Team Conference, Worcester, MA, June 2016

**C. Walde**, D. Cote, V. Champagne, Jr., R.D. Sisson, Jr., “The Microstructural Evolution of Powder Aluminum Alloys after Thermal Processing”, MS&T Conference, Salt Lake City, UT, October 2016

**C. Walde**, D. Cote, V. Champagne, Jr., R.D. Sisson, Jr., “The Microstructural Evolution of Powder Aluminum Alloys after Thermal Processing”, TMS Conference, Nashville, TN, February 2016

## 10 References

1. Champagne, V. Advancements in Cold Spray and Army Vision. in *Cold Spray Action Team Meeting* (2017).
2. Champagne, V. K. *The cold spray materials deposition process : fundamentals and applications*. (Woodhead, 2007).
3. Shackelford, J. F. *Introduction to Materials Science for Engineers*. (Prentice Hall, 2005).
4. *Handbook of Aluminum: Vol. 1: Physical Metallurgy and Processes*. (CRC Press, 2003).
5. Murr, L. E. *et al.* Metal Fabrication by Additive Manufacturing Using Laser and Electron Beam Melting Technologies. *J. Mater. Sci. Technol.* **28**, 1–14 (2012).
6. Kruth, J., Mercelis, P., Van Vaerenbergh, J., Froyen, L. & Rombouts, M. Binding mechanisms in selective laser sintering and selective laser melting. *Rapid Prototyp. J.* **11**, 26–36 (2005).
7. Azhari, A., Marzbanrad, E., Yilman, D., Toyserkani, E. & Pope, M. A. Binder-jet powder-bed additive manufacturing (3D printing) of thick graphene-based electrodes. *Carbon N. Y.* **119**, 257–266 (2017).
8. Ouyang, J., Yarrapareddy, E. & Kovacevic, R. Microstructural evolution in the friction stir welded 6061 aluminum alloy (T6-temper condition) to copper. *J. Mater. Process. Technol.* **172**, 110–122 (2006).
9. Champagne, V. K., Helfritsch, D., Leyman, P., Grendahl, S. & Klotz, B. Interface Material Mixing Formed by the Deposition of Copper on Aluminum by Means of the Cold Spray Process. *J. Therm. Spray Technol.* (2005). doi:10.1361/105996305X59332
10. Sabard, A., de Villiers Lovelock, H. L. & Hussain, T. Microstructural Evolution in Solution Heat Treatment of Gas-Atomized Al Alloy (7075) Powder for Cold Spray. *J. Therm. Spray Technol.* **27**, 145–158 (2018).
11. Balani, K., Agarwal, A., Seal, S. & Karthikeyan, J. Transmission electron microscopy of cold sprayed 1100 aluminum coating. *Scr. Mater.* **53**, 845–850 (2005).
12. Rokni, M. R., Widener, C. A. & Champagne, V. R. Microstructural Evolution of 6061 Aluminum Gas-Atomized Powder and High-Pressure Cold-Sprayed Deposition. *J. Therm. Spray Technol.* **23**, 514–524 (2014).
13. Rokni, M. R., Widener, C. A., Champagne, V. K. & Crawford, G. A. Microstructure and mechanical properties of cold sprayed 7075 deposition during non-isothermal annealing. *Surf. Coatings Technol.* **276**, 305–315 (2015).
14. Rokni, M. R., Widener, C. A., Crawford, G. A. & West, M. K. An investigation into microstructure and mechanical properties of cold sprayed 7075 Al deposition. *Mater. Sci. Eng. A* **625**, 19–27 (2015).
15. Rokni, M. R., Widener, C. A., Champagne, V. K., Crawford, G. A. & Nutt, S. R. The effects of heat treatment on 7075 Al cold spray deposits. *Surf. Coatings Technol.* **310**, 278–285 (2017).
16. Jodoin, B. *et al.* Effect of particle size, morphology, and hardness on cold gas dynamic sprayed aluminum alloy coatings. *Surf. Coatings Technol.* **201**, 3422–3429 (2006).

17. Lee, P. *et al.* *ASM Handbook, Volume 7: Powder Metallurgy - ASM International.* (1998).
18. metallurgy -- Britannica Library. *Britannica* (2017).
19. Levi, C. G. & Mehrabian, R. Microstructures of rapidly solidified aluminum alloy submicron powders. *Metall. Trans. A* **13**, 13–23 (1982).
20. Zheng, B. L., Lin, Y. J., Zhou, Y. Z. & Lavernia, E. J. Gas Atomization of Amorphous Aluminum Powder: Part II. Experimental Investigation. *Metall. Mater. Trans. B-PROCESS Metall. Mater. Process. Sci.* **40**, 995–1004 (2009).
21. Adkins, N. J. E. & Tsakiroopoulos, P. Design of powder metallurgy aluminium alloys for applications at elevated temperatures Part 1 Microstructure of high pressure gas atomized powders. *Mater. Sci. Technol.* **7**, 334–340 (1991).
22. Rokni, M. R., Widener, C. A., Ozdemir, O. C. & Crawford, G. A. Microstructure and mechanical properties of cold sprayed 6061 Al in As-sprayed and heat treated condition. *Surf. Coatings Technol.* **309**, 641–650 (2017).
23. Rokni, M. R., Widener, C. A., Crawford, G. A. & West, M. K. An investigation into microstructure and mechanical properties of cold sprayed 7075 Al deposition. *Mater. Sci. Eng. A* **625**, 19–27 (2015).
24. Sabard, A., de Villiers Lovelock, H. L. & Hussain, T. Microstructural Evolution in Solution Heat Treatment of Gas-Atomized Al Alloy (7075) Powder for Cold Spray. *J. Therm. Spray Technol.* 1–14 (2017). doi:10.1007/s11666-017-0662-2
25. Champagne, V. & Helfrich, D. Critical assessment 11: structural repairs by cold spray. *Mater. Sci. Technol.* **31**, 627–634 (2015).
26. Champagne, V., Nardi, A. & Cote, D. Materials Characterization of Advanced Cold-Spray Aluminum Alloys. *Int. J. Powder Metall.* **51**, (2015).
27. Borchers, C., Gärtner, F., Stoltenhoff, T., Assadi, H. & Kreye, H. Microstructural and macroscopic properties of cold sprayed copper coatings. *J. Appl. Phys.* **93**, 10064–10070 (2003).
28. King, P. C., Bae, G., Zahiri, S. H., Jahedi, M. & Lee, C. An Experimental and Finite Element Study of Cold Spray Copper Impact onto Two Aluminum Substrates. *J. Therm. Spray Technol.* **19**, 620–634 (2010).
29. Rokni, M. R., Widener, C. A. & Crawford, G. A. Microstructural evolution of 7075 Al gas atomized powder and high-pressure cold sprayed deposition. *Surf. Coatings Technol.* **251**, 254–263 (2014).
30. Stoltenhoff, T., Borchers, C., Gärtner, F. & Kreye, H. Microstructures and key properties of cold-sprayed and thermally sprayed copper coatings. *Surf. Coat. Technol.* **200**, 4947–4960 (2006).
31. Belsito, D., McNally, B., Bassett, L., Sisson, R. & Champagne, V. A Through-Process Model for Cold Sprayed ALuminum Alloys. 308 (2014).
32. Vander Voort, G. F. *et al.* *ASM Handbook, Volume 9: Vol. 9 Metallography and Microstructures.* (A S M International, Incorporated, 2004).
33. Lee, S. ., Saito, Y., Sakai, T. & Utsunomiya, H. Microstructures and mechanical properties of 6061 aluminum alloy processed by accumulative roll-bonding. *Mater. Sci. Eng. A* **325**, 228–235 (2002).

34. Tsui, T. Y., Oliver, W. C. & Pharr, G. M. Influences of stress on the measurement of mechanical properties using nanoindentation: Part I. Experimental studies in an aluminum alloy. *J. Mater. Res.* **11**, 752–759 (1996).
35. Richardson, M. J. & Charsley, E. L. Chapter 13 Calibration and Standardisation in DSC. *Handb. Therm. Anal. Calorim.* **1**, 547–575 (1998).
36. Klar, E. & Samal, P. K. *Powder metallurgy stainless steels : processing, microstructures, and properties*. (ASM International, 2007). doi:10.1361/pmss2007p001
37. Van Steenkiste, T. H., Smith, J. R. & Teets, R. E. Aluminum coatings via kinetic spray with relatively large powder particles. *Surf. Coat. Technol.* **154**, 237–252 (2002).
38. Lyle, J. P. & Cebulak, W. S. Powder metallurgy approach for control of microstructure and properties in high strength aluminum alloys. *Metall. Trans. A* **6**, 685–699 (1975).
39. Robson, J. D. Microstructural evolution in aluminium alloy 7050 during processing. *Mater. Sci. Eng. A* **382**, 112–121 (2004).
40. Chakrabarti, D. . & Laughlin, D. E. Phase relations and precipitation in Al–Mg–Si alloys with Cu additions. *Prog. Mater. Sci.* **49**, 389–410 (2004).
41. Nakayasu, H., Kobayashi, E., Sato, T., Holmestad, R. & Marthinsen, K. Orientation relationships of phase transformation in  $\alpha$ -Al<sub>12</sub>Mn<sub>3</sub>Si pseudomorphs after plate-like Al<sub>6</sub>Mn precipitate in an AA3004 Al–Mn based alloy. *Mater. Charact.* **136**, 367–374 (2018).
42. Barbosa, C., Dille, J., Delplancke, J.-L., Rebello, J. M. A. & Acselrad, O. A microstructural study of flash welded and aged 6061 and 6013 aluminum alloys. *Mater. Charact.* **57**, 187–192 (2006).
43. Warmuzek, M., Mrówka, G. & Sieniawski, J. Influence of the heat treatment on the precipitation of the intermetallic phases in commercial AlMn<sub>1</sub>FeSi alloy. *J. Mater. Process. Technol.* **157–158**, 624–632 (2004).
44. Sjölander, E. & Seifeddine, S. The heat treatment of Al–Si–Cu–Mg casting alloys. *J. Mater. Process. Technol.* **210**, 1249–1259 (2010).
45. Wang, S. C. & Starink, M. J. Two types of S phase precipitates in Al–Cu–Mg alloys. *Acta Mater.* **55**, 933–941 (2007).
46. Chakrabarti, D. . & Laughlin, D. E. Phase relations and precipitation in Al–Mg–Si alloys with Cu additions. *Prog. Mater. Sci.* **49**, 389–410 (2004).
47. Matsuda, K. *et al.* Crystal structure of the  $\beta''$  phase in an Al–1.0mass%Mg<sub>2</sub>Si–0.4mass%Si alloy. *Mater. Sci. Eng. A* **262**, 232–237 (1999).
48. Wolverton, C. Crystal structure and stability of complex precipitate phases in Al–Cu–Mg–(Si) and Al–Zn–Mg alloys. *Acta Mater.* **49**, 3129–3142 (2001).
49. Gupta, A. K., Gaunt, P. & Chaturvedi, M. C. The crystallography and morphology of the S'-phase precipitate in an Al(CuMg) alloy. *Philos. Mag. A* **55**, 375–387 (1987).
50. Zhao, Y. H., Liao, X. Z., Jin, Z., Valiev, R. Z. & Zhu, Y. T. Microstructures and mechanical properties of ultrafine grained 7075 Al alloy processed by ECAP and their evolutions during annealing. *Acta Mater.* **52**, 4589–4599 (2004).

51. Li, X. Z., Hansen, V., Gjønnnes, J. & Wallenberg, L. R. HREM study and structure modeling of the  $\eta'$  phase, the hardening precipitates in commercial Al–Zn–Mg alloys. *Acta Mater.* **47**, 2651–2659 (1999).
52. Liang, P. *et al.* Experimental investigation and thermodynamic calculation of the Al–Mg–Zn system. *Thermochim. Acta* **314**, 87–110 (1998).
53. Jeniski, R. A., Thanaboonsombut, B. & Sanders, T. H. The effect of iron and manganese on the recrystallization behavior of hotrolled and solution-heat-treated aluminum alloy 6013. *Metall. Mater. Trans. A* **27**, 19–27 (1996).
54. Li, Y. J., Muggerud, A. M. F., Olsen, A. & Furu, T. Precipitation of partially coherent  $\alpha$ -Al(Mn,Fe)Si dispersoids and their strengthening effect in AA 3003 alloy. *Acta Mater.* **60**, 1004–1014 (2012).
55. DeHoff, R. T. Quantitative serial sectioning analysis: preview. *J. Microsc.* **131**, 259–263 (1983).
56. Yanuka, M., Dullien, F. A. L. & Elrick, D. E. Serial sectioning and digitization of porous media for two- and three-dimensional analysis and reconstruction. *J. Microsc.* **135**, 159–168 (1984).
57. Spowart, J. E. Automated serial sectioning for 3-D analysis of microstructures. *Scr. Mater.* **55**, 5–10 (2006).
58. Burnett, T. L. *et al.* Large volume serial section tomography by Xe Plasma FIB dual beam microscopy. *Ultramicroscopy* **161**, 119–129 (2016).
59. Zankel, A., Wagner, J. & Poelt, P. Serial sectioning methods for 3D investigations in materials science. *Micron* **62**, 66–78 (2014).
60. Singh, S. S., Loza, J. J., Merkle, A. P. & Chawla, N. Three dimensional microstructural characterization of nanoscale precipitates in AA7075-T651 by focused ion beam (FIB) tomography. *Mater. Charact.* **118**, 102–111 (2016).
61. Spowart, J. E. Automated serial sectioning for 3-D analysis of microstructures. *Scr. Mater.* **55**, 5–10 (2006).
62. Spowart, J. E., Mullens, H. E. & Puchala, B. T. Collecting and analyzing microstructures in three dimensions: A fully automated approach. *JOM* **55**, 35–37 (2003).
63. Groeber, M. A., Haley, B. K., Uchic, M. D., Dimiduk, D. M. & Ghosh, S. 3D reconstruction and characterization of polycrystalline microstructures using a FIB–SEM system. *Mater. Charact.* **57**, 259–273 (2006).
64. Abbasi, R., Dzieciol, K. & Borbély, A. Three-dimensional analysis of creep voids in copper by serial sectioning combined with large field EBSD. *Mater. Sci. Technol.* **31**, 540–546 (2015).
65. Lin, F. X., Godfrey, A., Jensen, D. J. & Winther, G. 3D EBSD characterization of deformation structures in commercial purity aluminum. *Mater. Charact.* **61**, 1203–1210 (2010).
66. Soppela, I. *et al.* Rapid Particle Size Measurement Using 3D Surface Imaging. *AAPS PharmSciTech* **12**, 476–484 (2011).
67. Zaafarani, N., Raabe, D., Singh, R. N., Roters, F. & Zaefferer, S. Three-dimensional investigation of the texture and microstructure below a nanoindent in a Cu single crystal using 3D EBSD and crystal plasticity finite element simulations. *Acta Mater.* **54**, 1863–1876 (2006).

68. Konrad, J., Zaefferer, S. & Raabe, D. Investigation of orientation gradients around a hard Laves particle in a warm-rolled Fe<sub>3</sub>Al-based alloy using a 3D EBSD-FIB technique. *Acta Mater.* **54**, 1369–1380 (2006).
69. Belsito, D. Application of Computational Thermodynamic and Solidification Kinetics to Cold Sprayable Powder Alloy Design. (2014).
70. He, S., Liu, Y. & Guo, S. Cooling rate calculation of non-equilibrium aluminum alloy powders prepared by gas atomization. *Xiyou Jinshu Cailiao yu Gongcheng (Rare Met. Mater. Eng.* **38**, 353–356 (2009).
71. Ghoncheh, M. H. & Shabestari, S. G. Effect of Cooling Rate on the Dendrite Coherency Point During Solidification of Al<sub>2024</sub> Alloy. *Metall. Mater. Trans. A* **46**, 1287–1299 (2015).
72. Herbert, E. G. *et al.* On the measurement of stress-strain curves by spherical indentation. *Thin Solid Films* **398**, 331–335 (2001).
73. Mullis, A. M., Farrell, L., Cochrane, R. F. & Adkins, N. J. Estimation of Cooling Rates During Close-Coupled Gas Atomization Using Secondary Dendrite Arm Spacing Measurement. *Metall. Mater. Trans. B* **44**, 992–999 (2013).
74. Walde, C., Cote, D., Champagne, V. & Sisson, R. Characterizing the Effect of Thermal Processing on Feedstock Al Alloy Powder for Additive Manufacturing Applications. *J. Mater. Eng. Perform.* **0–9** (2018). doi:10.1007/s11665-018-3550-0
75. Tsaknopoulos, K., Walde, C., Jr, V. C. & Cote, D. Gas-Atomized Al 6061 Powder : Phase Identification and Evolution During Thermal Treatment. *JOM* (2018). doi:10.1007/s11837-018-3175-7
76. Badini, C., Marino, F. & Verné, E. Calorimetric study on precipitation path in 2024 alloy and its SiC composite. *Mater. Sci. Eng. A* **191**, 185–191 (1995).
77. Rokni, M. R., Widener, C. A., Ahrenkiel, S. P., Jasthi, B. K. & Champagne, V. R. Annealing behaviour of 6061 aluminium deposited by high pressure cold spray. *Surf. Eng.* **30**, 361–368 (2014).
78. Rokni, M. R., Widener, C. A. & Champagne, V. R. Microstructural stability of ultrafine grained cold sprayed 6061 aluminum alloy. *Appl. Surf. Sci.* **290**, 482–489 (2014).
79. Rokni, M. R., Widener, C. A. & Champagne, V. R. Microstructural stability of ultrafine grained cold sprayed 6061 aluminum alloy. *Appl. Surf. Sci.* **290**, 482–489 (2014).
80. Walde, C., Ristau, R. & Cote, D. Automated 3D EBSD for metallic powders. *MethodsX* **5**, 652–655 (2018).